Order by structural disorder and field effects in frustrated systems

Vladimir Maryasin

To cite this version:

Vladimir Maryasin. Order by structural disorder and field effects in frustrated systems. Strongly Correlated Electrons [cond-mat.str-el]. Université Grenoble Alpes, 2015. English. NNT : 2015GREAY051 . tel-01288985

HAL Id: tel-01288985
https://theses.hal.science/tel-01288985

Submitted on 15 Mar 2016

UNIVERSITÉ GRENOBLE ALPES

THÈSE

Pour obtenir le grade de

DOCTEUR DE L'UNIVERSITÉ GRENOBLE ALPES

Spécialité : **Physique theorique**

Arrêté ministériel : 7 août 2006

Présentée par

Vladimir MARYASIN

Thèse dirigée par **M. Mike ZHITOMIRSKY**

préparée au sein de **Service de Physique Statistique, Magnétisme et Supraconductivité, CEA Grenoble**
et de **l'Ecole Doctorale de Physique**

Ordre par le désordre structural et les effets du champ magnétique dans les systèmes frustrés.

Thèse soutenue publiquement le **10 Novembre, 2015**,
devant le jury composé de :

Mme. Claudine Lacroix
Institut Neel, CNRS & Université Grenoble Alpes, Présidente
M. Andreas Honecker
Université de Cergy-Pontoise, Rapporteur
M. Frédéric Mila
Ecole Polytechnique Fédérale de Lausanne, Rapporteur
M. Peter Holdsworth
Ecole Normale Supérieure de Lyon, Examinateur
M. Xavier Waintal
SPSMS/CEA Grenoble, Examinateur
M. Mike Zhitomirsky
SPSMS/CEA Grenoble, Directeur de thèse

Acknowledgements

First of all I would like to express my gratitude to my advisor Mike Zhitomirsky for the three years of common work. I feel very fortunate to have a supervisor, who gave me the freedom to explore on my own and at the same time patiently provided guidance, when I needed it. I appreciate all our discussions about various problems of physics, thank you for sharing your knowledge and wisdom. Work with you greatly expanded my scientific, geographic and personal horizons.

I want to thank Claudine Lacroix, Andreas Honecker, Frédéric Mila, Peter Holdsworth and Xavier Waintal for being in my defence committee. I am grateful for their attention to my work and for interesting questions and discussions about it.

I am very grateful to Xavier Waintal for providing me with the absolute access to the computational cluster *Meso*. The whole numerical part of my work was done on it.

During these three years I was working alongside so many interesting and talented people. All the days, spent in the Theory Group were very enriching and motivating. Looking back, I would say that meeting the people of our Lab and Service was the best thing that happened to me during my PhD. I would like to thank my office mates, Benoit Gaury and Joseph Weston for all the time, we spent together full of mutual encouragement and help in all sorts of *challenges*. Moreover, Benoit, your patient corrections and explanations played the main role in my progress in French; I will also miss our interesting talks about everything in life. Joseph, owning to your never-ending energy and emotions, our office was always a very lively and pleasant place; and I will never forget our hike to the Neron, thanks for taking us there. I also spent a lot of wonderful time with Lars Elster. Whatever I did, I could call him to join, and it was great. A very special thanks goes to my fellow PhD students from C1 Jean-Eudes Duvauchelle, Mounir Boukahil and Alexandra Palacio-Morales, who helped me a lot to settle down in Grenoble during my first months here.

I wish to express my gratitude from my deep heart to my whole family and my dearest parents above all. I am indefinitely grateful for your permanent support, encouragement and invaluable advice. All this became possible because of you. Finally, I owe a debt of gratitude to my best friend and beloved wife, Valeria. She was the one to bear all my bad moods and to live through all my difficulties. My darling, thank you for agreeing to take this adventure, for your love, devotion and patience. I dedicate this work to you.

Abstract

Competing interactions are an essential feature of frustrated magnetic systems, they stand behind a large degeneracy of classical or mean-field ground states. In many cases such degeneracy can be lifted by thermal and quantum fluctuations, this mechanism is commonly called *order from disorder*.

Experimentally studied magnetic systems inevitably contain a certain amount of structural disorder. In this Ph.D. project I study the influence of defects: vacancies and bond disorder on a degenerate ground state manifold for various frustrated systems. The quenched disorder is found to be capable of consistently lifting the degeneracy, moreover, it has an opposite tendency, compared to the order by disorder mechanism, produced by fluctuations. For every considered model, analytic energy corrections are derived in the form of effective anisotropic terms, which act on the manifold of degenerate ground states. Analytical arguments are confirmed by numerical calculations, which include energy minimisation and classical Monte Carlo simulations. The detected sequences of ordered states is attributed to competition of fluctuations and structural disorder. The observed effect can open additional possibilities in tuning and manipulating magnetic structure of frustrated spin systems.

Finally, the effect of an external magnetic field is investigated for the pure XY pyrochlore antiferromagnet. Depending on the field orientation I observe phase transitions, which do not exist within the mean-field description of the system. They are generalisations of the spin-flop transition for the case of broken discrete $\mathbb{Z}_k$ symmetry with $k > 2$.

Résumé

La compétition des interactions est une caractéristique essentielle des systèmes frustrés, elle est à l'origine d'une large dégénérescence des états fondamentaux classiques ou, obtenus par une théorie de champ moyen. Fréquemment la dégénérescence peut être levée par des fluctuations thermiques ou quantiques, ce qui constitue la base du mécanisme appelé *ordre par le désordre*.

Les systèmes magnétiques étudiés expérimentalement contiennent une quantité inévitable de désordre structural. Dans cette thèse de doctorat, l'influence des défauts, créé par des sites inoccupés ou par un désordre des liens sur l'espace dégénéré des états fondamentaux est étudiée pour des systèmes frustrés divers. Nous avons trouvé qu'un désordre structural est, lui aussi, capable de lever systématiquement la dégénérescence; par ailleurs, la tendance est inverse par rapport au le mécanisme d'ordre par le désordre produit par les fluctuations. Pour chacun des modèles considérés, les corrections à l'énergie ont été calculées sous la forme de termes anisotropes effectifs qui agissent sur l'espace dégénéré des états fondamentaux. Ces arguments analytiques ont été confirmés par des calculs numériques que nous avons effectués par minimisation de l'énergie, ainsi que par simulation de type Monte-Carlo classique. La séquence des états ordonnés que nous avons détectée est attribuée à la compétition entre l'effet d'ordre induit par les fluctuations et celui induit par les défauts structuraux. L'effet observé peut ouvrir des possibilités supplémentaires de contrôler la structure magnétique des systèmes.

Enfin, les effets d'un champ magnétique externe ont été étudiés pour le système antiferromagnétique pyrochlore pur avec anisotropie de plan facile. Nous avons observé des transitions de phases qui dépendent de l'orientation du champ et qui n'existent pas dans la description de type champ moyen du système. Elles constituent une généralisation des transitions de type spin-flop pour le cas de la symétrie discrète $\mathbb{Z}_k$ brisée avec $k > 2$.

Contents

Chapter 1

Introduction

The term frustration generally refers to a competition without definitive win. Cancellation of dominant microscopic couplings enhances the role of various subdominant interactions, producing a plethora of unconventional phases and effects. Due to its incredibly rich and complex behaviour, frustrated systems attract a lot of research attention. High degeneracy of ground states represents another fundamental consequence of competing interactions. Moreover, it is often the case that the classical ground state is invariant under some symmetry operation, while the Hamiltonian that describes the system is not. Such a symmetry is said to emerge in the low-energy sector of the model. Mathematically, it can be expressed via the noncommutation of the symmetry operator $\hat{O}$ with the Hamiltonian of the system

$$[\hat{\mathcal{H}}, \hat{O}] \neq 0, \qquad [\hat{\mathcal{H}}, P\hat{O}P] = 0, \tag{1.1}$$

where P is a projector to a ground state sector of $\hat{\mathcal{H}}$.

These *emergent* symmetries should not be confused with a more common situation of spontaneous symmetry breaking. In the latter the invariance of the Hamiltonian is spontaneously lost in a specific low-energy state, while the states themselves are related by some symmetry operation. Emergent symmetry describes, in a sense, an opposite situation: the system becomes more symmetric in the ground state sector in comparison with the higher energies.

The operator $\hat{O}$ does not describe a true symmetry of the system, it is rather an artefact of the application of the mean-field approximation to the model. So the corresponding degeneracy can in principle be lifted by various mechanisms that are left beyond the mean-field theory. For example, these accidentally degenerate states may have different entropy S or a different spectrum of zero-point quantum fluctuations:

$$F = E_{\text{cl}} - TS, \qquad E_{\text{g.s.}} = E_{\text{cl}} + \frac{\hbar}{2}\sum_k \omega_k. \tag{1.2}$$

These degeneracy lifting mechanisms, which are associated with fluctuations, thermal or quantum, are called *order by disorder* after a work of Jacques Villain *et al.* [1]. In its modern form it was first used by Shender [2] for explaining magnetic order of the $Mn_3Cr_2Ge_3O_{12}$ garnet. Being investigated for numerous spin models, the order by disorder mechanism finds so far only a few realisations in magnetic materials. Perhaps, the clearest examples of the order by disorder selection are provided by the 1/3 magnetisation plateau in triangular-lattice antiferromagnets [3–

5] and by zero-field noncoplanar spin structure of the XY pyrochlore antiferromagnet $Er_2Ti_2O_7$ [6, 7].

Various other mechanisms, which lift the accidental ground state degeneracy should be taken into account when studying real systems. As was already mentioned, additional interactions, may cause state selection already on the mean-field level. Internal subleading effects, such as weak anisotropies and further neighbour interaction, usually bring a complication due to the difficulty of distinguishing fluctuation effects from those of interactions. On the contrary, external tunable parameters, such as an application of a magnetic field or hydrostatic pressure, presents a tool for probing the order by disorder phenomenon. It is also possible to propose other scenarios of modification of the energy of the system. For example, a defect in a lattice causes an energy gain due to local relief of frustration, therefore, it has the potential of causing the lifting of degeneracy.

Most of the existing theoretical studies of defects in magnetic solids focus on a single impurity problem. A number of works were devoted to studying magnetic susceptibility of different types of impurities: vacancies and additional spins. Sachdev *et. al* showed that the impurity susceptibility has a Curie-like divergence with the universal effective spin [8]. Logarithmic corrections to $\chi(T)$ were later derived [9, 10]. Another important line of studies is dedicated to studying long range magnetisation patterns around impurities in the external field. The universal form of tilting of spins, surrounding a single vacancy was obtained by Lüscher and Sushkov using harmonic spin-wave calculations [11]. The result was later generalised to the case of impurities in the form of additional spins [12], and confirmed by quantum Monte Carlo simulations [13, 14].

In addition to this, frustrated magnets exhibit a variety of new effects, caused by impurities. Structural disorder modifies locally exchange interactions and destroys perfect magnetic frustration at the microscopic level [15]. As a result, magnetic moments tilt from the equilibrium bulk structure causing spin textures, even at zero magnetic field [16, 17]. Another subsequent effect is that a single impurity produces a net uncompensated magnetic moment [16–18], which is, in contrast with collinear antiferromagnets, fractional and highly dependent on the system details.

Scaling from a single vacancy to a more realistic situation of finite concentration of impurities is straightforward for simple collinear antiferromagnets. In the case of frustrated magnets more complex behaviour can be detected. First of all, a common notion is that a combination of the large degeneracy of states together with disorder leads to the spin-glass phase. This behaviour was first observed in the random ferro-antiferromagnetic interaction model, which represents, however, an example of a rather strong randomness.

A surprising effect appears when the opposite limit of not very intense disorder is considered. Henley first suggested an idea that dilution can, on the contrary, be the source of order. He argued that a noncollinear state is selected by nonmagnetic impurities from the degenerate ground state manifold of FCC antiferromagnet [19]. The action of dilution on the ground state manifold was described by a phenomenological positive biquadratic exchange. Henley's prediction was supported by Monte Carlo simulations by Giebultowicz [20]. Later the same positive biquadratic exchange was derived for the BCT antiferromagnet [21] and for the $J_1 - J_2$ square antiferromagnet [22] by minimising the energy of the tilted distorted state and averaging over vacancy replica. Monte Carlo studies of the latter model with XY and Heisenberg spins [23, 24] confirmed the argumentation by reporting orthogonal orientation of sublattices in the presence of impurities.

However, such an “antiparallel” phase was found to have only short range correlations as it involved no symmetry breaking.

All aforementioned systems can be decoupled into independent subsystems in such a way that the effective fields produced by spins of one subsystem (a) at any spin of the other subsystem (b) cancel: $\mathbf{h}_{a\to b} = 0$. For those systems a very simple and elegant argument was presented, which explains collinear order by fluctuations and anticollinear order, favoured by impurities. Both fluctuations of spins and vacancies on subsystem a produce a distortion to the local field, felt by the second subsystem $\delta\mathbf{h}_{a\to b} \neq 0$. Similar to the situation of a square antiferromagnet in external field, interaction of such a distortion with the spins on subsystem b is maximised when $\mathbf{S}_b \perp \delta\mathbf{h}_{a\to b}$. When the distortion is caused by fluctuations, it is perpendicular to the direction of spin on subsystem a: $\delta\mathbf{h}_{a\to b} \parallel \delta\mathbf{S}_a \perp \mathbf{S}_a$. Therefore, two subsystems tend to align parallel to each other. In the second case of a vacancy on a site a: $\delta\mathbf{h}_{a\to b} \parallel \mathbf{S}_a$, and the antiparallel alignment is realised.

Interestingly, in a somewhat different context of magnetic multilayers positive biquadratic exchange interaction was reported by Slonczewski [25]. It appeared as a subleading interaction due to interface roughness. Accordingly, the order by disorder and the effect of structural disorder are associated with negative and positive effective biquadratic interactions. Such additional terms are even proposed to be included in numerical simulations of classical frustrated systems at low T to emulate the effect of quantum fluctuations or disorder [26].

These two concepts: (i) structural disorder can consistently and independently from the particular impurity realisation select the states from the accidentally degenerate ground state manifold, and (ii) effect of fluctuations and structural disorder on the degenerate lowest energy states can be represented by the action of an effective interaction terms with different signs, constitute the core ideas of this work.

Though simple and quite appealing, Henley’s argumentation for obvious reasons cannot be applied to a general problem of lifting the continuous ground state degeneracy in noncollinear frustrated magnets,

In this Ph.D. project we aim to present a unified approach to frustrated systems with continuous emergent ground state degeneracy. We consider models with varying properties of ground states: the Heisenberg antiferromagnet on a triangular lattice, the easy-plane pyrochlore antiferromagnet, 120° and 90° compass models. While the standard state selection effect of fluctuations in these systems is well established, we concentrate on studying the *order by structural disorder* mechanism. Consequently, we investigate the interplay of this weak and substantially energetic effect with the ordering by fluctuations.

In addition to this, we demonstrate how spin fluctuations, and in general the beyond-mean-field approximation effects can be probed by application of additional tunable external parameters, such as the magnetic field.

Outline of the work

In this work we analyse the interplay between energetic and fluctuational effects in lifting the emergent ground state degeneracy of frustrated systems. The first two chapters show various methods that were used throughout our studies. They are all described in various studies and reviews, so in these methodological chapters we present only the necessary introduction to the methods and demonstrate modifications that were made for adapting them to specific models. The rest of the work (chapters 4-7, apart from the description of the corresponding models) contains original results that were obtained during this Ph.D. project. More details about the contents of the work are presented below.

In **chapter 2** various analytical methods that were used to study lifting of ground state degeneracy are demonstrated. First, we present technical details of the real space perturbation expansion, which is an efficient alternative to a commonly-used harmonic spin-wave approach. The method treats fluctuation of spins around an equilibrium configuration in terms of a series of effective Hamiltonians that act on the whole degenerate ground state manifold. After that we describe our analytic model for disorder and introduce an integration procedure for spin deviations, which gives the energies of the new ground states.

Chapter 3 contains the description of numerical methods and techniques that were used in this work. First of all, we present the core of our classical Monte Carlo algorithm, which uses a combination of the single spin Metropolis steps with microcanonical overrelaxation updates. Then a finite size scaling procedure is described, which is an essential tool for extracting the precise information about the studied phase transitions. We give a brief introduction to scaling procedures in case of second and first order phase transitions, as well as for Berezinsky-Kosterlitz-Thouless phase transition. Finally, the details of our mean-field energy minimisation algorithm, which is used for studying ground state of the systems at $T = 0$, are demonstrated.

In **chapter 4** the collective impurity effects on the paradigmatic frustrated system: the Heisenberg triangular antiferromagnet are studied. First, building on the previous works [21, 22], we show that, averaged over different realisations, bond and site disorder generate positive biquadratic exchange, and therefore, lift the continuous degeneracy of spin plane orientation in the magnetic field. Such an effective interaction is obtained by integrating out static fluctuations in a spin texture and due to its sign favours the *least* collinear spin configurations. This state selection competes with the action of the conventional order by disorder mechanism, which can be described by a negative biquadratic exchange. The rich phase diagram of the system with impurities, which emerges from this competition, is obtained by Monte Carlo simulations.

In addition to this, we present another effect of a finite impurity concentration on the Heisenberg triangular system. It is the nontrivial dependence of the effective vacancy moment on the defect concentration $m_{\text{imp}}(n_{\text{imp}})$. A substantial growth of m_{imp} in comparison with the single vacancy value is explained by the clustering of impurities. This quadratic in concentration effect turns out to be nonnegligible due to the small initial value of $m^{\circ}_{\text{imp}} = 0.04S$ [16].

In **chapter 5** we study the effect of structural disorder on the anisotropic XY pyrochlore model, which describes the low-temperature magnetic properties of the rare earth magnetic insulator $\text{Er}_2\text{Ti}_2\text{O}_7$. This model is interesting because in pyrochlores lifting of the ground state degeneracy by biquadratic spin interaction is prohibited by symmetry. In this chapter we show that structural disorder favours the coplanar $m_{x^2-y^2}$ (ψ_3) magnetic state, the opposite of the $m_{3z^2-r^2}$ (ψ_3) configuration, which is stabilised by fluctuations in the pure system. The competition of two effects results in a reconfigurational first order phase transition, occurring at low temperature inside the antiferromagnetic phase. The study of this system is additionally motivated by the fact that $Er_2Ti_2O_7$ represents the least contested experimentally observed example of the order by disorder mechanism. As in pyrochlores weaker interactions that break the degeneracy of states on the mean-field level are suppressed by symmetry.

The same anisotropic XY pyrochlore model is employed in **chapter 6** to investigate the competition of fluctuations with the external magnetic field in the pure system. Finite H lifts the ground state degeneracy at the mean field level and leads to the rather simple $H-T$ phase diagrams. We show that the weak $\mathbb{Z}_6$ anisotropy which is generated by impurities modifies the observed phase diagrams. It leads to an extra second order phase transition at low magnetic field when $\mathbf{H} \parallel [001]$ and an unusual pair of reentrant phase transitions when $\mathbf{H} \parallel [111]$. The findings of the symmetry analysis are confirmed by numerical and analytical energy minimisation in the low-H limit. Finally, classical Monte Carlo $H-T$ phase diagrams for different directions of the magnetic field are presented.

Chapter 7 is devoted to the study of the order by structural disorder phenomenon in 120° and 90° compass models. These models provide an interesting example of frustrated models on nonfrustrated lattices with very unusual sets of symmetries: both true and emergent. Discrete emergent symmetries of the 120° model are found to be preserved by vacancies, while continuous symmetry is lifted in favour of states, least supported by fluctuations. Monte Carlo simulations confirm such a scenario and show an appearance of a new long range order phase at low T. This new phase is unusual as it can only appear as a result of both structural disorder and fluctuations. Contrary to this no new ordered phase is stabilised by defects in the 90° model in two and three dimensions. Instead the paramagnetic phase bounds the fluctuation-stabilised nematic phase from below. Compass models are known to describe orbital order in Mott insulators and superconductivity in Josephson junction arrays and therefore, this chapter extends the concept of state selection by quenched disorder to a wider range of physical models.

Lastly, the results of this work are summarised in **chapter 8**, in addition, a brief overview of possible future work on the subject is presented.

Chapter 2

Analytical methods

The aim of this chapter is to present technical details of the analytical methods that are used in our studies. Our operational example throughout this chapter will be the Heisenberg antiferromagnetic model on the triangular lattice. It shares the main features of all models, considered in the work, but on the other hand is simple enough to serve as a demonstrative tool. As all the methods presented in this chapter will be used for various systems, we keep a certain level of generality in the expressions to avoid further repetitions and emphasise the points that will be crucial for us in further use regardless of the model. We point out that in this section we will be focused on the technical aspects of the calculations, rather than actual physical results, which will be the purpose of the next chapter.

The standard analytic approach to the problem of degeneracy lifting in frustrated magnets is to use the spin-wave theory. The spectrum of zero point quantum fluctuations [27] (or thermal fluctuations in the classical case [28]) is calculated in the harmonic approximation for a few (or many) degenerate states. Then the configuration with the lowest total energy is the one selected by fluctuations. In section 2.1 of this chapter we present an alternative approach to the problem of continuous degeneracy lifting in pure frustrated magnets. The method treats fluctuations around a classical ground state in terms of the real-space perturbation expansion and comprises our main analytical tool in the studies of all subsequent models.

Section 2.2 is devoted to the analytical treatment of quenched disorder in the spin system. We aim to describe spin vacancies, which model substitutions of magnetic ions by the nonmagnetic ones. So we concentrate on the continuous limit of disorder: weak vacancies, where the impurity spin is present, but has a reduced length. This allows to handle nonmagnetic impurities by the methods of perturbation expansion, developed earlier. We also briefly consider weak bond disorder as the other type of structural disorder.

2.1 Real space perturbation expansion

This method, which we call Real Space Perturbation Theory (RSPT) was employed in a number of studies of the degeneracy lifting in various frustrated systems, such as FCC [29, 30], XY checkerboard AFM [31] XXZ model on the Kagome lattice [32]. Moreover, this formalism suits well to tackle the systems that lack translational symmetry, for example, for frustrated magnets with structural disorder [33]. Eventually such a study will be the principal aim of the work, but first, in this section we develop the real space perturbation expansion for pure noncollinear magnets, following the course of Ref. [34].

Real space perturbation expansion is essentially the method of treating the terms in the Hamiltonian that are left beyond the mean-field approximation. All these terms that describe fluctuations of spins around the equilibrium configuration can be split into two parts. One of them depends only on the coordinates of only one spin, while in the other we collect the correlations of spins on neighbouring sites. Then an auxiliary problem that contains only the former site-diagonal part can be directly solved and used for determining the average of the latter terms that are treated as perturbations.

The main advantage of this approach is the description in terms of effective Hamiltonians, operating in the manifold of classical ground states. It allows to study the state selection by thermal and quantum fluctuations for the whole manifold of degenerate states without ad-hoc assumptions about plausible candidates. Moreover, the method is relatively simple, at least for a few lowest order corrections and does not require numerical computations, like in most of the spin-wave calculations.

To be specific in our derivations of this section, we use a model of frustrated triangular system of Heisenberg spins with antiferromagnetic interaction (HTAFM) under an external magnetic field. The particular choice of the system is motivated by the fact that it is simple and exemplary at the same time. Moreover, it will be the main system under consideration in chapter 4, so we will directly use the obtained results hereafter. We emphasise the fact that all the derivations can and will be repeated with minor alterations for other systems, so here we maintain a certain level of generality. The physical aspects of the obtained results will be discussed later, in this section we concentrate on describing the technical details of the analytical approach.

The section is organised as follows. Subsection 2.1.1 contains a brief presentation of HTAFM, while the main part of it is devoted to a general decomposition of the Hamiltonian in the site-diagonal part, which in many cases can be easily solved, and a series of interaction terms. The obtained results are applied in the following subsections 2.1.2 and 2.1.3 to the cases of thermal and quantum fluctuations respectively. We use perturbation theory up to the third order to generate a series of fluctuation-induced corrections, which may lift the initial ground state degeneracy. We also present a simple diagrammatic representation for both perturbation expansions.

2.1.1 General form of real space expansion

In this subsection we perform a decomposition of the Hamiltonian in a series small perturbations. We describe the method on the particular example of the Heisenberg atiferromagnetic model on the triangular lattice in an external magnetic field

$$\hat{\mathcal{H}} = J\sum_{\langle ij\rangle}\mathbf{S}_i\cdot\mathbf{S}_i - \mathbf{H}\cdot\sum_i \mathbf{S}_i. \tag{2.1}$$

When the field is finite $0 < H < H_s = 9JS$ the mean-field ground state of this model has continuous 'accidental' degeneracy, consisting in arbitrary orientation of the spin plane with respect to the field direction [27, 35]. In any of these lowest energy configurations, each spin is pointing along its local field, which is made up of interaction with the neighbours and external field

$$\mathbf{S}_i \parallel \mathbf{h}_i; \qquad \mathbf{h}_i = \mathbf{H} - J\sum_{j=1}^{z}{}'\mathbf{S}_j. \tag{2.2}$$

Here and everywhere throughout this work by prime we denote the summation over all nearest neighbours of site i. One very important property of the model that will be used in further derivations is that the magnitude of the local field is independent of $\mathbf{H}$ and of the site index: $|h_i| = h = 3JS$. A simple proof of this statement as well as a more detailed introduction into HTAFM can be found in chapter 4.

Then we can start with an arbitrary ground state and perform a coordinate transform to the local coordinates. The new frame is defined by the condition that the $\hat{\mathbf{z}}_i$ axis is directed along the local field $\mathbf{h}_i$ on the site i. The directions of the other two local coordinate axes can be chosen in a way which is the most appropriate for the considered spin system. For the systems, which have a distinct plane in spin space, for example, when the whole configuration is planar or in case of planar anisotropy, it is convenient to choose $\hat{\mathbf{x}}_i$ coordinate to lie in this plane, and $\hat{\mathbf{y}}_i$ to be orthogonal to it.

For the HTAFM we choose a specific bond-dependent local coordinates: we select the $\hat{\mathbf{x}}_i$ and $\hat{\mathbf{x}}_j$ axes such that they lie within the common $\hat{\mathbf{z}}_i - \hat{\mathbf{z}}_j$ plane, and $\hat{\mathbf{y}}_i$ and $\hat{\mathbf{y}}_j$ to be orthogonal to it. For planar spin configurations is is the natural choice of coordinate frame because it results in $\hat{\mathbf{x}} - \hat{\mathbf{z}}$ plane to be independent of all spins (and bonds) and to confine all the spins. For a more general case of noncoplanar ordered states it involves some additional complications, as the coordinate frame then depends on a bond, rather than on one lattice site. In this case $\hat{\mathbf{x}}_i(ij)$ and $\hat{\mathbf{y}}_i(ik)$ are not necessarily orthogonal. However, in our calculations this will only be important for the third and higher order corrections, which are subdominant for this system. In this section we still present an expression for these terms, without successive calculations as corresponding corrections are relevant for other models of this study.

Written in the new coordinate frame the mean-field ground state implies that all spins point along their local $\hat{\mathbf{z}}_i$ axis with $S^z = S$. The parameterisation of a state is transferred onto a set of angles between local axis $\cos\theta_{ij} = (\hat{\mathbf{z}}_i \cdot \hat{\mathbf{z}}_j)$. Spins may deviate from their equilibrium state due to fluctuations, disorder, etc., which results in small but nonzero S^x and S^y components. Then the Hamiltonian of this system takes the form

$$\begin{aligned}\hat{\mathcal{H}} &= J\sum_{\langle ij\rangle}\Big[S_i^y S_j^y + \big(S_i^z S_j^z + S_i^x S_j^x\big)\cos\theta_{ij} + \big(S_i^x S_j^z - S_i^z S_j^x\big)\sin\theta_{ij}\Big] \\ &- H\sum_i S_i^z\cos\theta_i + S_i^x\sin\theta_i.\end{aligned} \tag{2.3}$$

Note that θ_i - is the angle between the local $\hat{\mathbf{z}}_i$ axis and the direction of an external magnetic field. The main step of RSPT is to collect all terms that depend on components of only one spin.

$$\begin{aligned}\hat{\mathcal{H}} &= E_{\mathrm{cl}} + h\sum_i (S - S_i^z) + J\sum_{\langle ij\rangle}\Big[S_i^y S_j^y + S_i^x S_j^x\cos\theta_{ij} + (S - S_i^z)(S - S_j^z)\cos\theta_{ij} \\ &+ \big(S_i^x S_j^z - S_i^z S_j^x\big)\sin\theta_{ij}\Big] - H\sum_i S_i^x\sin\theta_i.\end{aligned} \tag{2.4}$$

E_{cl} - is the classical degenerate energy of the ground state, the following terms are corrections due to fluctuations of spins. The first sum of the right-hand part is diagonal in real space site index, it represents mean-field energy renormalisation. Taken alone, as an unperturbed Hamiltonian $\hat{\mathcal{H}}_0 = h\sum_i (S - S_i^z)$ its excitation spectrum can be easily obtained. Then the rest terms represent the interaction of fluctuations of different neighbouring sites $\hat{V}$, the method treats them perturbatively over $\hat{\mathcal{H}}_0$.

$$\hat{\mathcal{H}} = E_{\text{cl}} + \hat{\mathcal{H}}_0 + \hat{V}. \tag{2.5}$$

In the following subsections we develop specific perturbation theories for classical and quantum cases. It is important to note that there is no explicit small parameter that distinguishes $\hat{V}$ from $\hat{\mathcal{H}}_0$. The method is in fact a $1/z$ expansion, where z - is the coordination number of the lattice as $\hat{\mathcal{H}}_0 = O(zJ)$, while $\hat{V} = O(J)$.

2.1.2 Thermal order by disorder

Below we elaborate real space perturbation theory for the system of purely classical spins of arbitrary length S. We take the temperature of the system to be small but finite $T \ll J$. In this case, thermal spin fluctuations S_i^x and S_i^y are small, compared to S, and we can expand

$$S^z = \sqrt{S^2 - S^{x2} - S^{y2}} = S - \frac{S^{x2}}{2S} - \frac{S^{y2}}{2S} + O\left(S^{\perp 4}\right). \tag{2.6}$$

Then decomposition (2.4) will take the form

$$\hat{\mathcal{H}} = \hat{\mathcal{H}}_0 + \hat{V}_2 + \hat{V}_3; \qquad \hat{\mathcal{H}}_0 = \frac{h}{2S}\sum_i \left[S_i^{x2} + S_i^{y2}\right]; \tag{2.7}$$

$$\hat{V}_2 = J\sum_{\langle ij\rangle}\left[S_i^y S_j^y + S_i^x S_j^x \cos\theta_{ij}\right]; \tag{2.8}$$

$$\hat{V}_3 = -\frac{J}{2S}\sum_{\langle ij\rangle}\sin\theta_{ij}\left[S_i^x\left(S_j^{x2} + S_j^{y2}\right) - S_j^x\left(S_i^{x2} + S_i^{y2}\right)\right]. \tag{2.9}$$

We have omitted classical energy E_{cl} as it has the same value for the whole degenerate manifold of states. Also, linear in S^x terms vanish because (2.7) is the decompositions around a ground state. Terms $\hat{V}_2$ - $\hat{V}_3$ are perturbations, ranged according to the power of spin deviation.

As was said before we take $\hat{\mathcal{H}}_0$ as an unperturbed Hamiltonian, and we are able to calculate all kinds of thermal averages in the usual way

$$\langle A(\mathbf{S}^\perp)\rangle = \frac{1}{Z}\int A(\mathbf{S}^\perp)e^{-\frac{\hat{\mathcal{H}}_0}{T}}\prod_i d\mathbf{S}_i^\perp, \tag{2.10}$$

where $A(S)$ - is an arbitrary function of spin fluctuations, and Z - partition function. Particularly we will be interested in the quantities like $\langle (S_i^\alpha)^k (S_j^\beta)^l\rangle$. First, as $\hat{\mathcal{H}}_0$ is a noninteracting Hamiltonian, fluctuations of different spins or of different components of one spins are independent and uncorrelated. Therefore, we have $\langle (S_i^\alpha)^k (S_j^\beta)^l\rangle = \langle (S_i^\alpha)^k\rangle\langle (S_j^\beta)^l\rangle$ unless $i = j$ and $\alpha = \beta$. Then an average of odd power of spin fluctuation vanishes since $\hat{\mathcal{H}}_0$ is an even function of S_i^α. The nonzero quantities are

$$\langle (S^\alpha)^2\rangle = \frac{ST}{h}; \qquad \langle (S^\alpha)^4\rangle = 3\left(\frac{ST}{h}\right)^2; \qquad \langle (S^\alpha)^{2k+1}\rangle = 0; \tag{2.11}$$

for arbitrary i and $\alpha = \{x, y\}$.

A thermodynamic perturbation theory is developed to calculate the entropy of degenerate states. It results in corrections to the free energy of the system:

$$F = F_0 - \frac{\langle \hat{V}^2 \rangle}{2T} + \frac{\langle \hat{V}^3 \rangle}{6T^2} + \cdots , \tag{2.12}$$

where we assumed that the perturbation V has a vanishing average $\langle V \rangle = 0$, and F_0 - is the degenerate free energy of the unperturbed Hamiltonian $\hat{\mathcal{H}}_0$. The leading correction is given by

$$\Delta F^{(2)} = -\frac{J^2}{2T} \left\langle \Big[\sum_{\langle ij \rangle} \Big(S_i^y S_j^y + S_i^x S_j^x \cos\theta_{ij} \Big) \Big]^2 \right\rangle . \tag{2.13}$$

According to eq. (2.11) and the discussion above it, the sum reduces to

$$\Delta F^{(2)} = -\frac{TJ^2S^2}{2h^2} \sum_{\langle ij \rangle} \left(1 + \cos^2\theta_{ij} \right) . \tag{2.14}$$

Thus we obtained an effective correction to the free energy, which depends on the ground state through the parameterising angles θ_{ij}. This term acts on the manifold of degenerate states and represents entropic selection by thermal fluctuations. For the considered model the nontrivial correction appeared already at the lowest level of perturbation theory, so we emphasise the relative easiness of the RSPT method. However, for other frustrated models the lowest order may be not enough, and one may need to go further and consider contributions from higher order interaction terms, for example, $\hat{V}_3$ or/and higher free energy corrections $\Delta F^{(3)} = \frac{\langle \hat{V}^3 \rangle}{6T^2}$ and so on.

These considerations can be recast into a simple cluster expansion with a graphical representation, which is especially handy when the contribution of higher order corrections have to be calculated. We present this technique as the following set of rules:

1. Each term of the k-th order of perturbation expansion is represented by a graph, which contains exactly k links. Every link that connects two sites represents one of the interaction terms $\hat{V}_l$ (2.8) - (2.9). Multiple different links per bond are allowed, but only connected diagrams should be taken into account.

2. Then one counts a total number of S_i^x and S_i^y terms brought by the links, connected to each site. It can be represented by a pair of *occupation numbers* per vertex. A cluster gives a nonzero contribution if and only if occupation numbers of each site for both polarisations are even.

3. Finally, to calculate a total contribution of the diagram one includes: a) a factor $\langle S^{\alpha 2} \rangle = \frac{ST}{h}$ for each vertex that is doubly occupied, $\langle S^{\alpha 4} \rangle = 3(\frac{ST}{h})^2$ - four-times occupied, etc.; b) a functional prefactor from expressions (2.8 - 2.9) per each link used; c) a combinatorial prefactor that equals to the number of distinct ways a graph can be constructed d) a summation over the whole lattice and a corresponding general prefactor from the perturbation theory (2.12).

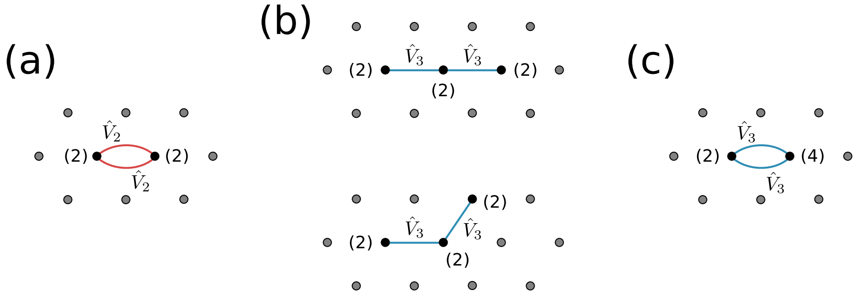

Figure 2.1: Second order perturbation theory graphs, constructed from $\hat{V}_2$ (red links) and $\hat{V}_3$ (blue links) interactions. Numbers in brackets are occupation numbers for fluctuation terms S_i^x on each vertex. Only one polarisation was used, graphs with S_i^y and both polarisations are constructed likewise.

To demonstrate this technique in figure 2.1 we present the diagrams, constructed from two interaction terms $\hat{V}_2$ and $\hat{V}_3$, which contribute to the second order correction $\Delta F^{(2)}$. The first graph 2.1(a) was calculated above in equation (2.14). The others can be similarly considered. Note that only S^x polarisation was used in clusters of Fig.2.1, the contributions of S^y component and mixed terms are calculated likewise. For visualisation figure 2.2 contains some of the third order corrections $\Delta F^{(3)}$.

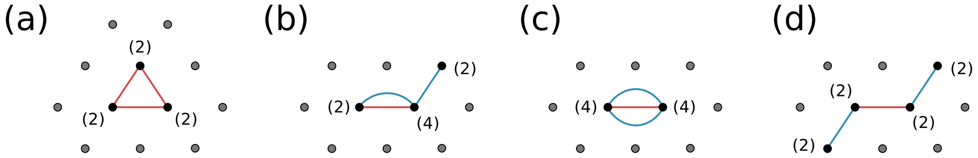

Figure 2.2: Four clusters, which contribute to $\Delta F^{(3)}$. The colour code is the same, as above, and only S_i^x polarisation is used.

The expression for its single bond contribution 2.2(c) is especially simple, we provide it for an additional illustration:

$$\Delta F^{(3c)} = 3\,\frac{1}{6T^2}\cdot\frac{9S^4T^4}{h^4}\sum_{\langle ij\rangle}\frac{J^2}{4S^2}\cos\theta_{ij}\sin^2\theta_{ij}. \tag{2.15}$$

It is interesting to compare this method with the usual way of considering thermal order by disorder by spin-wave calculations. The result of RSPT is an analytic series of effective contributions to F in two small parameters: T and $1/z$. Interaction terms $\hat{V}_3, \hat{V}_4, \ldots$ and higher correspond to anharmonic terms in spin-wave theory and are usually discarded. In RSPT it is relatively easy to obtain at least the leading contribution of these terms. As it should be, their contribution is of higher order in T as they include a higher number of averages $\langle (S^\alpha)^2\rangle \propto T$ (compare diagram 2.1(a) with 2.1(b) - (c) and 2.2(a) with 2.2(b)-(d)). On the other hand diagrams 2.1(a) and 2.2(a) are both $O(T)$, but differ in the graph length, which scales as $1/z$. They contribute to harmonic spin-wave approximation, which naturally includes the graphs of all lengths at once.

2.1.3 Quantum order by disorder

In this subsection we formulate the RSPT for the case of quantum fluctuations. The idea behind the calculations is essentially the same, as in the case of thermal order by disorder. The results also resemble the ones of the previous subsection: in the end, we obtain a series of corrections to the ground state energy with $1/z$ being the small parameter. It is interesting to note that the terms of the series can be attributed to different orders of the usual $1/S$ decomposition. However, there will also be some differences, particularly in the formulation of the graphical cluster expansion for the quantum case.

If spins are treated as quantum mechanical operators, it is natural to express spin components via ladder operators $S^{\pm} = S^x \pm iS^y$. Then the expansion of the Hamiltonian in fluctuations will take the following form:

$$\begin{aligned} &\hat{\mathcal{H}} = \hat{\mathcal{H}}_0 + \hat{V}_{2a} + \hat{V}_{2b} + \hat{V}_3 + \hat{V}_4; && \hat{\mathcal{H}}_0 = h\sum_i (S - S_i^z); \\ &\hat{V}_{2a} = -\frac{J}{4}\sum_{\langle ij\rangle}(1-\cos\theta_{ij})\left(S_i^+S_j^+ + S_i^-S_j^-\right); && \hat{V}_{2b} = \frac{J}{4}\sum_{\langle ij\rangle}(1+\cos\theta_{ij})\left(S_i^+S_j^- + S_i^-S_j^+\right); \\ &\hat{V}_3 = \frac{J}{2}\sum_{\langle ij\rangle}\sin\theta_{ij}\left(S_i^- + S_j^+\right)(S - S_i^z); && \hat{V}_4 = J\sum_{\langle ij\rangle}\cos\theta_{ij}\,(S - S_i^z)\left(S - S_j^z\right). \end{aligned} \tag{2.16}$$

Again, the first term is chosen as an unperturbed Hamiltonian, it has the form of the Zeeman Hamiltonian for noninteracting spins. The ground state $|0\rangle$ of such system is a fully saturated configuration, it corresponds to one of the degenerate mean-field states. It is the eigenstate of the S^z operator with $S^z|0\rangle = S|0\rangle$. Below we will calculate quantum corrections due to fluctuations to these states. In a saturated state we have $S_i^+|0\rangle = 0$. Therefore, our ground state is the noninteracting vacuum of spin flips

$$\langle 0|\hat{V}|0\rangle = 0. \tag{2.17}$$

The conjugate operator decreases the total spin by producing one excitation quantum $S_i^-|0\rangle \propto |1\rangle$ with the energy $\langle 1|\hat{\mathcal{H}}_0|1\rangle = h$. This allows us to treat all interaction terms perturbatively using the standard Rayleigh-Schrödinger perturbation expansion.

The second order correction to the energy is then calculated by

$$\Delta E^{(2)} = \sum_n \frac{\langle 0|\hat{V}|n\rangle\langle n|\hat{V}|0\rangle}{E_0 - E_n}. \tag{2.18}$$

The only nonzero contribution to $\Delta E^{(2)}$ is given by the $\hat{V}_{2a}$ interaction. When applied to the vacuum state, $\hat{V}_{2a}$ generates a pair of spin flips on adjacent sites - an exited state $|n\rangle$ with the energy $E_n = E_0 + 2h$, which is then annihilated by a conjugate operator. After the substitution we obtain

$$\Delta E^{(2)} = -\frac{J^2S^2}{8h}\sum_{\langle ij\rangle}(1-\cos\theta_{ij})^2. \tag{2.19}$$

In the Heisenberg triangular antiferromagnet already the second order correction has nontrivial dependence on angles θ_{ij}. However, it may happen that the second order of perturbation theory correction $\Delta E^{(2)}$ does not lift the initial ground state degeneracy. Then one has to proceed to higher order corrections, $\Delta E^{(3)}$, etc.

$$\Delta E^{(3)} = \sum_{n,m} \frac{\langle 0|\hat{V}_1|n\rangle\langle n|\hat{V}|m\rangle\langle m|\hat{V}_1|0\rangle}{(E_0 - E_n)\,(E_0 - E_m)}. \tag{2.20}$$

Similar to the case of thermal order by disorder, the determination of nonzero contributions of the perturbation theory can be done with the help of the diagrammatic technique, defined by the following rules:
1. Each term of the k-th order of perturbation series is represented by a diagram that consists of exactly k links. Every link corresponds to one of the interaction terms V_i (2.16) that acts on a specific lattice bond. More than one link per bond is allowed, but only the connected diagrams should be taken.
2. The ground state is a vacuum for the spin flips, therefore, every term of the perturbation theory starts (ends) with creation (annihilation) of a pair of spin flips upon acting of $S_i^- S_j^-$ ($S_i^+ S_j^+$) part of the V_1 term. Also, each lattice site should have an equal number of S_i^- and S_i^+ operators.

Following these rules the term (2.19) corresponds to the diagram:

$$|00\rangle \xrightarrow{S_i^- S_j^-} |11\rangle \xrightarrow{S_i^+ S_j^+} |00\rangle\,, \tag{2.21}$$

which is essentially analogous to the thermal graph (a) in figure 2.1 and the corresponding free energy correction (2.14).

This process is the only second order process that appears in the quantum perturbation expansion, below we calculate also the third order processes. There are two types of them corresponding to triangular and dimer clusters respectively. The former is described by the diagram:

$$|000\rangle \xrightarrow{S_i^- S_j^-} |110\rangle \xrightarrow{S_j^+ S_k^-} |101\rangle \xrightarrow{S_k^+ S_i^+} |000\rangle. \tag{2.22}$$

For the coplanar spin configuration the corresponding energy correction is

$$\Delta E^{(3a)}_{(ij,jk,ki)} = \frac{J^3 S^3}{32h^2}(1-\cos\theta_{ij})(1+\cos\theta_{jk})(1-\cos\theta_{ki}). \tag{2.23}$$

To obtain the final result one needs to take into account all 6 possible processes on one triangle and sum over all the plaquette of the lattice. The dimer process is described by the diagram

$$|00\rangle \xrightarrow{S_i^- S_j^-} |11\rangle \xrightarrow{S_i^z S_j^z} |11\rangle \xrightarrow{S_i^+ S_j^+} |00\rangle \tag{2.24}$$

that describes the action of $\hat{V}_1$ and $\hat{V}_4$ operators and produces the term

$$\Delta E^{(3b)} = \frac{J^3 S^2}{16h^2} \sum_{\langle i,j\rangle} (1-\cos\theta_{ij})^2 \cos\theta_{ij}. \tag{2.25}$$

Equations (2.19), (2.23) and (2.25) have the form of effective Hamiltonians, operating in the manifold of degenerate classical ground states, parameterised by the angles θ_{ij}. As in previous section they highlight the physics behind the real space perturbation expansion and its underlying difference with the commonly used harmonic spin wave calculations. $\Delta E^{(3b)}$ (2.25) is in fact a renormalisation of the second order dimer process (2.19) by the interaction of excited states.

As it originates from the anharmonic term $\hat{V}_4$, it is of higher order in $1/S$ decomposition $O(J)$. Each following order of perturbation expansion will contain expressions for further corrections. However, none of these nonlinear terms appear in the harmonic spin wave calculations. On the other hand $\Delta E^{(3a)}$ scales as $O(JS)$, and is a part of the harmonic spin wave contribution, which naturally includes all lattice loops of arbitrary length. The main difficulty in the real space perturbation expansion comes from the fact that the number of diagrams quickly grows with the order of perturbation theory, in a sense this is the price you pay for for the possibility of performing the calculations analytically.

2.2 Structural disorder

Structural disorder modifies locally exchange interactions and destroys perfect magnetic frustration at the microscopic level. As a result, magnetic moments tilt from the equilibrium bulk structure producing spin textures [12, 16, 36] and net uncompensated moments [16–18]. These magnetic moments of impurities will be studied in chapter 4.3 in the framework of the triangular antiferromagnet. The idea of uncompensated moments and related local magnetic fields was also used by Henley in his explanation of vacancy-induced degeneracy lifting in the J_1–J_2 square-lattice antiferromagnet [22]. Though simple and appealing, this approach cannot be applied to a general problem of order by structural disorder in noncollinear frustrated magnets.

In this section we develop an approach to study the effect of structural disorder on frustrated systems with continuous ground state degeneracy in the framework of real space perturbation decomposition (2.4). In the analogy with the previous section we show how bond and site disorder generate a series of effective anisotropic exchanges that act on the manifold of degenerate ground states. Despite having a similar form, disorder-induced degeneracy lifting has a qualitatively different effect on the ground state selection in the frustrated magnet, compared with the effect of thermal or quantum fluctuations, considered earlier. The corresponding correction comes primarily from the linear in spin tilting term V_1, which is absent when fluctuations around a true ground state are considered. Hence, the degeneracy breaking term will appear as a result of straightforward energy minimisation in real space due to linear impurity induced perturbation. Technically, it results in a different combination of trigonometric functions of angles θ_{ij} and in inversion of the sign of the anisotropies.

As we will show, for the Heisenberg triangular antiferromagnet a nontrivial degeneracy breaking term appears already as the effect of direct energy minimisation. But in general the anisotropy, generated by the lowest energy correction may be forbidden by symmetry. So to give a flavour of calculation of the higher order corrections in this section we present a series of effective Hamiltonians beyond the leading contribution.

Also, note that the investigated effect of order by structural disorder is essentially classical and static. So we assume that spins are three-component classical vectors with $|\mathbf{S}_i| = S$ and consider them at $T = 0$. Therefore, we do not study the effect of quantum or thermal fluctuations around the new disorder induced configurations, which is a much more involved task.

The rest of the section is organised as follows: in subsection 2.2.1 we develop a model that allows analytic treatment of diluted magnetic systems in the limit of weak nonmagnetic impurities. Then we show how the selection terms arise from minimisation of ground state energy with the impurity-induced linear perturbation. In the following subsection 2.2.2 we perform the similar calculations for the structural disorder in the form o the weak bond disorder.

2.2.1 Site disorder

A single vacancy induces a strong local perturbation of the magnetic structure in noncollinear antiferromagnets [16]. To obtain a qualitative insight into the analytic treatment of the impurity problem we use a model of weak site disorder [21]. Specifically, we let a small fraction $n_{\text{imp}} \ll 1$ of classical spins to be shorter by a small amount $\epsilon \ll 1$. These impurities are distributed randomly over the lattice and we assign a parameter $p_i = 1$ to every impurity spin and $p_i = 0$ otherwise: $\sum_i p_i = N_{\text{imp}}$. In the spin Hamiltonian impurities are included by substitution $\mathbf{S}_i \to \mathbf{S}_i(1-\epsilon p_i)$, and we have for pairwise spin-spin interactions

$$S_i^\alpha S_j^\beta \longrightarrow S_i^\alpha S_j^\beta \big[1-\epsilon(p_i+p_j)+\epsilon^2 p_i p_j\big]. \tag{2.26}$$

The last term is quadratic in ϵ and is nonvanishing only when each of the sites i and j contains a vacancy. It will be neglected in further calculations due to the considered $n_{\text{imp}} \ll 1$ and $\epsilon \ll 1$ limit. Before we proceed with the Hamiltonian decomposition, it is useful to list the summation properties of parameters p_i that follow from the definition:

$$p_i^2 = p_i; \qquad \frac{1}{N}\sum_i p_i = n_{\text{imp}}; \qquad \langle\langle \frac{1}{N_{\text{bond}}}\sum_{\langle i,j\rangle} p_i p_j \rangle\rangle = n_{\text{imp}}^2. \tag{2.27}$$

In the last equality double angular brackets explicitly indicate the averaging over all possible disorder realisations. Otherwise it can be understood as taking a thermodynamic limit when the impurity allocation is completely random. Physically its main message is that situations, which involve correlation of two or more different impurities are rare and contribute weakly to the calculated averages. So throughout this work we will never consider them as our main limit will be $n_{\text{imp}} \ll 1$.

The presence of vacancies violates the balance between interactions and reduces frustration, as a result, spins deviate from their former ground state. In the local coordinate frame, like the one introduced in subsection 2.1.1 spins acquire transverse components $\mathbf{S}_i^\perp$, which are small as long as disorder strength is small. Then we perform the same decomposition as in the previous section. Namely, we make a substitution (2.26) into equation (2.3) and collect all single-site terms. A static distortion of the equilibrium magnetic structure will be then found from a simple minimisation procedure.

Impurities modify both the mean-field ground state energy and the local fields that act on each spin. Indeed, the true local field $\mathbf{h}_i = \mathbf{H} - J\sum_{j=1}^{z}{}'\mathbf{S}_j(1-\epsilon p_j)$ now acquires a nonzero transverse component. But it is convenient to express the vacancy-induced changes explicitly, keeping unchanged pure mean-field values E_{cl} and h. Then, as long as the surrounding spin deviations are small, we can treat this transverse component as a linear force $\hat{V}_1$ that drives the system out of the degenerate equilibrium position. Of course h^z component also gets renormalised, we recast it as the renormalisation of spin deviations S^x and S^y. In the end, we obtain

$$\hat{\mathcal{H}} = E_{\rm cl} + \epsilon n_{\rm imp} h S N + \hat{\mathcal{H}}_0 + \hat{V}_1; \tag{2.28}$$

$$\hat{\mathcal{H}}_0 = \frac{h}{2S} \sum_i \left[S_i^{x2} + S_i^{y2} \right] \left(1 - \epsilon p_i - \frac{JS\epsilon}{h} {\sum_{j=1}^{z}}' \cos\theta_{ij} p_j \right); \tag{2.29}$$

$$\hat{V}_1 = JS \sum_{\langle ij \rangle} \sin\theta_{ij} \left(S_i^x - S_j^x \right) \left[1 - \epsilon \left(p_i + p_j \right) \right]. \tag{2.30}$$

The second term in the decomposition of $\hat{\mathcal{H}}$ (2.28) is an overall energy shift due to the presence of impurities. And the two extra terms in the parenthesis of (2.29) correspond to modification of length of spin i and the above mentioned renormalisation of the h^z component of the local field.

The crucial difference with the preceding section is that because of the presence of random vacancies linear in spin deviations term $\hat{V}_1$ does not vanish:

$$\hat{V}_1 = -JS\epsilon \sum_i S_i^x {\sum_{j=1}^{z}}' \sin\theta_{ij} p_j. \tag{2.31}$$

$\hat{V}_1 \neq 0$ denotes that the mean-field ground state is no longer a true ground state of the system. Indeed, spins, surrounding a defect rearrange due to the local relief of frustration. Then the new equilibrium magnetic structure can be found by minimising a new Hamiltonian $\hat{\mathcal{H}}_0 + \hat{V}_1$.

$$S_i^y = 0; \qquad S_i^x = \frac{JS^2\epsilon}{h} \frac{{\sum_{j=1}^{z}}' \sin\theta_{ij} p_j}{1 - \epsilon p_i - \frac{JS\epsilon}{h} {\sum_{j=1}^{z}}' \cos\theta_{ij} p_j}; \tag{2.32}$$

and

$$\Delta E = \hat{\mathcal{H}}_0 + \hat{V}_1 = -\frac{J^2 S^3 \epsilon^2}{2h} \sum_i \frac{\left({\sum_{j=1}^{z}}' \sin\theta_{ij} p_j \right) \left({\sum_{k=1}^{z}}' \sin\theta_{ik} p_k \right)}{1 - \epsilon p_i - \frac{JS\epsilon}{h} {\sum_{j=1}^{z}}' \cos\theta_{ij} p_j}. \tag{2.33}$$

We decompose the denominator and show the leading term in the ϵ^k series. We also remind that we are only interested in linear in $n_{\rm imp}$ terms. Then, according to (2.27) we have $\langle\langle p_i p_j \rangle\rangle = n_{\rm imp} \delta_{ij}$ and the dominant contribution to eq. (2.33) is given by

$$\Delta E^{(1)} = -\frac{J^2 S^3 \epsilon^2}{2h} \sum_i {\sum_{j=1}^{z}}' \sin^2\theta_{ij} p_j^2. \tag{2.34}$$

Averaging over possible impurity distributions, we get the expression for the energy correction due to weak vacancies in the limit of small ϵ and $n_{\rm imp}$

$$\Delta E^{(1)} = -\frac{J^2 S^3 \epsilon^2 n_{\rm imp}}{h} \sum_{\langle i,j \rangle} \sin^2\theta_{ij}. \tag{2.35}$$

For the Heisenberg TAFM this expression already depends on the angles θ_{ij}, which parameterise the ground state, and can lift the accidental ground state degeneracy. It may not be the case for other systems, so below we obtain further corrections to the energy to illustrate our approach and its analogy with the fluctuation decompositions, presented in the previous section. It may be also interesting to see the structure of further terms in the framework of possible $\epsilon \to 1$ limit, which is essential when one wants to compare the obtained results with the real dilution results.

First one can consider the interaction terms in the perturbation decomposition of the Hamiltonian (2.28), such as $\hat{V}_2$ or higher:

$$\hat{V}_2 = J\sum_{\langle ij\rangle}\left[S_i^yS_j^y + S_i^xS_j^x\cos\theta_{ij}\right]\left[1-\epsilon(p_i+p_j)\right]. \tag{2.36}$$

It represents energy modification due to correlation of two spin tilting, surrounding an impurity. We substitute (2.32) into (2.36) and recover the leading in ϵ term:

$$\Delta E^{(2)} = \frac{J^3S^4\epsilon^2}{h^2}\sum_{\langle i,j\rangle}\sum_{k=1}^{2}{}''\cos\theta_{ij}\sin\theta_{ik}\sin\theta_{jk}p_k^2. \tag{2.37}$$

The second sum here runs over the sites, neighbouring both i and j, in a triangular geometry there are two of sites for every bond. To make an analogy with the results of the previous section, correction (2.37) can be rewritten as a sum over all triangular plaquettes. Like before (2.37) is of the same order as (2.35) in dilution strength $O(\epsilon^2)$, but represents a larger elementary cluster and therefore is of higher order in $1/z$.

Also, decomposing further the denominator of equation (2.33), we get the term that represents renormalisation of a single bond energy correction (2.35)

$$\Delta E^{(3)} = -\frac{J^3S^4\epsilon^3}{2h^2}\sum_{i}\sum_{j=1}^{z}{}'\sin^2\theta_{ij}\cos\theta_{ij}p_j^3. \tag{2.38}$$

$\Delta E^{(3)}$ represents the same order term in $1/z$ expansion as $\Delta E^{(2)}$. Also, both introduce the third harmonic in angle θ_{ij}, and for certain systems can induce the leading energy shift.

2.2.2 Bond disorder

In a very similar way other types of structural disorder can be treated. For example, bond disorder that appears in real materials as a result of magneto-elastic coupling or disorder on nonmagnetic crystalline structure can be modelled via the fluctuating coupling constants

$$J\to J(1+\delta_{ij}); \qquad \sum_{\langle ij\rangle}\delta_{ij}=0; \qquad \frac{1}{N_{\text{bond}}}\sum_{\langle ij\rangle}\delta_{ij}^2 = D. \tag{2.39}$$

The fluctuating part δ_{ij} should not be confused with Kronecker delta. In this section is considered to be uncorrelated on adjacent bonds and small to keep all the exchange constants well inside antiferromagnetic parameter range $D\ll 1$. The subsequent calculation is completely similar to the previous section up to a substitution $-\epsilon(p_i+p_j)\to\delta_{ij}$. Bond disorder induces a nonvanishing linear in deviations term that causes tilting of the spins

$$\hat{V}_1 = SJ\sum_{\langle ij\rangle}\delta_{ij}\sin\theta_{ij}\left(S_i^x - S_j^x\right). \tag{2.40}$$

Minimisation of the Hamiltonian $\hat{\mathcal{H}}_0+\hat{V}_1$ with respect to S_i^x under the assumption that bonds fluctuate independently gives

$$S_i^x = -\frac{JS^2}{h}\,\frac{\sum_{j=1}^{z}{}'\delta_{ij}\sin\theta_{ij}}{1+\frac{JS}{h}\sum_{j=1}^{z}{}'\delta_{ij}\cos\theta_{ij}}. \tag{2.41}$$

In comparison with the weak impurity model (sec. 2.2.1) we now have only one small parameter D that describes the structural disorder. The type of the cluster for each correction is now determined by the properties (2.39), namely by the rule that each bond must be included in the cluster at least twice. Thus up to the lowest order in disorder strength

$$\Delta E^{(1)} = -\frac{DJ^2S^3}{h}\sum_{\langle i,j\rangle}\sin^2\theta_{ij}. \tag{2.42}$$

As in the previous section, further corrections $\Delta E^{(2)}, \Delta E^{(3)}$, etc. are obtained by considering interaction of spin deviations $\hat{V}_2 = J\sum_{\langle ij\rangle}(1+\delta_{ij})S_i^xS_j^x\cos\theta_{ij}$ and decomposing the denominator of (2.41).

The possibility to treat different types of disorder by the same method is quite functional and demonstrates the universality of the real space perturbation approach. However, in this study we mainly stay concentrated on the disorder in the form of nonmagnetic substitutions or vacancies. As will be shown in further chapters, our numerical studies cover exactly the case of true vacancies. They support our findings that for certain frustrated systems dilution stabilises new long range order phases. In order to undoubtedly extend this conclusion to the case of bond disorder, additional numerical studies are required.

Chapter 3

Numerical methods

3.1 Monte-Carlo simulations

Monte Carlo (MC) numerical techniques make use of random numbers to solve various kinds of mathematical problems. Here in this study we will be interested in the particular class of tasks: calculating the thermal average of an observable M in a canonical ensemble of a classical system

$$\langle M \rangle = \frac{1}{Z} \int_{\Omega} dx A(x) e^{-\beta E(x)}. \tag{3.1}$$

Even in this specific formulation a complete and rigorous review of various MC methods is by far not the aim of this section. For this we refer to acknowledged books, [37, 38] and instead we briefly present the methods and optimisation techniques that were used in our studies of various exchange Hamiltonians.

In the spirit of the standard MC integration technique one may think of generating a sufficient number of random microstates of the system to calculate the integral (3.1). Unfortunately, such a straightforward approach, which is called *direct sampling* fails because most of the randomly generated spin configurations would contribute negligibly to the sum due to the Boltzmann weight together with a huge number of degrees of freedom. This problem is bypassed by the *importance sampling*, the idea of which is to select spin configurations randomly and independently from the equilibrium distribution

$$P_{\text{eq}}(x) = \frac{\exp[-\beta E(x)]}{Z}. \tag{3.2}$$

These spin configurations, when sampled adequately large in number, constitute, to a very good approximation, a canonical ensemble. Therefore, average of a macroscopic property can be calculated as a simple arithmetic mean over the sampled microstates.

The organisation of the rest of the section is the following: in subsection 3.1.1 we present the Metropolis algorithm, which efficiently generates random microstates from the Boltzmann distribution. Subsection 3.1.2 is devoted to the simple but effective overrelaxation technique that highly increases the efficiency of the single spin Metropolis algorithm. The analysis of errors is made in subsection 3.1.3. Finally, in the last two subsections we concentrate on the ways to implement and optimise the presented algorithm: we discuss methods of parallelising the task and present technical details of our realisation of the MC simulations.

3.1.1 Metropolis sampling

We consider a system of classical vector spins in equilibrium and its phase space Ω with each point fully describing the microstate s_i of the system. The probability of each state is given by the Boltzmann distribution (3.2), which is not known because of the partition function in the denominator. What can be calculated, though, is the relative probability $P_{\mathrm{eq}}(s_i)/P_{\mathrm{eq}}(s_j)$, which depends only on the energy difference between two states

$$\Delta E = E_i - E_j. \tag{3.3}$$

Therefore, the problem of unknown Z can be avoided by generating a new sample state directly from the previous one using a *Markov chain* of microstates. The concept of Markov process lies in the core of Metropolis algorithm, an we present it below.

Consider a discrete stochastic process of evolution of the classical system with time. At each moment t_i the state of the system is described by a point in the phase space: $x_i = s_{t_i}$. A stochastic process is called a Markov process if the conditional probability of the future state (conditional on all its past states) depends only on the present state, in other words, it is a memoryless process. So the conditional probability to find a system in the state $x_{n+1} = s_{t_{n+1}}$, if its its predecessors were $s_{t_n}, s_{t_{n-1}}, \ldots$ equals to

$$P\left(x_{n+1} = s_{t_{n+1}} | x_n = s_{t_n}; x_{n-1} = s_{t_{n-1}}; \ldots; x_1 = s_{t_1}\right) = P\left(x_{n+1} = s_{t_{n+1}} | x_n = s_{t_n}\right). \tag{3.4}$$

The corresponding sequence of states $\{s_t\}$ is called a Markov chain, and the above conditional probability can be interpreted as the transition probability to move from state i to state j in a single step,

$$W_{ij} = W(s_i \to s_j) = P(x_{n+1} = s_j | x_n = s_i) \tag{3.5}$$

with the usual properties of transition probabilities $W_{ij} \geq 0$ and $\sum_j W_{ij} = 1$. Thus W_{ij} can be interpreted as the i,j-th element of the stochastic matrix W that completely specifies the stochastic dynamical evolution of the system given the initial state s_0 at $t = 0$.

The property of independence of transition probabilities on the evolution history is rather special, and only some real systems actually do have such a physical dynamics. The importance sampling Monte Carlo process (and the Metropolis algorithm which will be presented below) is a Markov process, with a particular choice of transition probabilities: one must satisfy the principle of detailed balance with the equilibrium probability $P_{\mathrm{eq}}(s_j)$,

$$W_{ji} P_{\mathrm{eq}}(s_j) = W_{ij} P_{\mathrm{eq}}(s_i). \tag{3.6}$$

Detailed balance guarantees that a stationary state with the probability distribution P_{eq} is sampled. Any transition rate which satisfies eq. (3.6) is acceptable. The most common choice of W_{ij} in statistical physics has the Metropolis form [39]

$$W_{ij} = \min\left(e^{-\Delta E/T}, 1\right). \tag{3.7}$$

Now we have all the ingredients of Metropolis sampling and can describe the protocol step by step:

1) For a current spin configuration choose a lattice site and a new trial spin state of this site.

2) Calculate the energy change ΔE from this trial move.
3a) If $\Delta E < 0$, accept the move as it reduces the total energy.
3b) If $\Delta E > 0$, generate a random number x, uniformly distributed in $(0,1)$. Accept the trial state if $x < \exp(-\Delta E/T)$, and stay in the former state otherwise.
4) Repeat the procedure, starting from 1).

Consecutive probing of every spin of the lattice or probing of N random spins is considered as a unit move of the protocol and is called the Monte Carlo Step (MCS). After a fixed number of MCS have been made, the observable M_n is calculated and added to the statistical average which is being kept. As the algorithm generates trial states with a probability proportional to Eqn. (3.4), the desired average $\langle M\rangle = \sum_n P_n M_n$ simply becomes an arithmetic average over the entire sample of states which is kept. A finite sample estimate of an order parameter is

$$\langle M\rangle = \frac{1}{N}\sum_{i=1}^{N} M_i. \tag{3.8}$$

The same applies to energy E or any other directly measurable observable. Employing fluctuation dissipation theorems we can similarly estimate specific heat and order parameter susceptibility

$$\begin{aligned} C &= \frac{\partial E}{\partial T} = \frac{\langle E^2\rangle - \langle E\rangle^2}{NT^2}; && (3.9)\\ \chi &= \frac{\partial M}{\partial H} = \frac{N}{T}(\langle M^2\rangle - \langle M\rangle^2). && (3.10) \end{aligned}$$

In addition to detailed balance, other important constraint on the algorithm is *ergodicity*, which states that all possible configurations of the system should be attainable. In principle, it must be possible to reach each point of the phase space, starting from any other point. There is a danger that specialised algorithms may be unintentionally nonergodic, for example, due to the symmetry restrictions of the steps, thus yielding incorrect results.

A related problem in studying the phase transitions comes from the fact that well inside the ordered phase different regions of phase space are separated by very high energy barriers, which make it practically almost impossible to explore the whole phase in one simple Metropolis run. Such trapping is called quasi-nonergodicity and can be dealt with by performing several independent simulations starting from different initial spin configurations.

3.1.2 Overrelaxation

Another efficient way to enhance the random walk through the phase space is called overrelaxation [40]. The idea of the technique is to include occasional deterministic micro-canonical steps that put a system into a remote state in the phase space with the same energy. Overrelaxation moves take the simplest form when the Hamiltonian of the system is linear in each spin and can be rewritten in terms of local fields h_i that act on each spin:

$$\hat{\mathcal{H}} = \sum_i \mathbf{S}_i \cdot \mathbf{h}_i. \tag{3.11}$$

Then it is clear that the energy of the system remains unchanged if one rotates any spin around the direction of its local field by arbitrary angle ϕ. It is convenient to choose for the micro-canonical move the most distant rotation $\phi = \pi$

$$\mathbf{S} \longrightarrow \mathbf{S}' = 2\left(\mathbf{S}\cdot\mathbf{n}\right)\mathbf{n} - \mathbf{S}, \tag{3.12}$$

where $\mathbf{n}$ - is the unit vector, pointing in the direction of the local field that acts on spin $\mathbf{S}$.

A typical use of the overrelaxation technique is to perform a micro-canonical sweep of all spins of the lattice after one or several MCS. As a final remark about overrelaxation we note that enhancement of the walk through the phase space also helps to decrease the autocorrelation time of the random Markovian process. As a result occasional overrelaxation steps decrease statistical errors, associated with the finite number of sampled microstates. This topic will be discussed in more details in the next subsection.

3.1.3 Estimate of errors

The obtained MC estimates are always a subject to errors of various types: both systematic and statistical. Considering the former, the errors that come from the finite lattice size and boundary conditions can actually be used to extract precise information about phase transition temperature, as will be explained in section 3.2. Other sources of systematic errors can be overcome by the choice of a good random number generator and by discarding a sufficient number of initial measurements to allow for a good equilibration. Below we shall discuss the origin of statistical errors of MC simulations and how one should proceed to decrease it.

The estimate of the average of an observable from N independent measurements is given by equation (3.1). Using the Central Limit Theorem of statistics the standard error of this estimate can be expressed through the variance of $\langle M\rangle$: $\Delta\langle M\rangle = \sigma(M)/\sqrt{N}$. We substitute $\sigma(M)$ by its unbiased estimate and reconstruct the formula for the computation of errors of averages from uncorrelated measurements

$$\Delta\langle M\rangle = \left[\frac{1}{N\left(N-1\right)}\sum_i \left(M_i - \langle M\rangle\right)^2\right]^{1/2}. \tag{3.13}$$

However, one cannot directly apply this result to importance sampling MC algorithm due to the autocorrelations of the subsequently generated observations $\{M_i\}$. When the generated sample states are correlated, the statistical error increases as $\Delta\langle M\rangle \rightarrow \Delta\langle M\rangle\left(1 + 2\tau_M/\delta t\right)$, where τ_M and δt are autocorrelation time, measured in MCS and time between the subsequent observations respectively. This effect is especially important close to the phase transitions, where τ_M may diverge, which results in the *critical slowing down* of the MC algorithm. In other words, close to the phase transition one needs to skip more steps to generate statistically independent configurations.

In our study we typically performed one measurement every $5 - 10$ MCS and also include *overrelaxation* moves (see subsection 3.1.2 for more details), which also help to decrease the autocorrelation times within a single scan. In any case effectively we get rid of autocorrelation effects by averaging over N_{repl} of independent runs. For the MC simulations of the system with impurities it was the averaging over different disorder realisation, for pure systems we performed a number of runs with random initial spin configurations. So in the end all our measurements and error bars are calculated by

$$\langle M\rangle = \frac{1}{N_{\mathrm{repl}}}\sum_{j=1}^{N_{\mathrm{repl}}} M_j^*; \qquad \Delta\langle M\rangle = \frac{1}{N_{\mathrm{repl}}}\left[\sum_{j=1}^{N_{\mathrm{repl}}}\left(M_j^* - \langle M\rangle\right)^2\right]^{1/2}, \tag{3.14}$$

where M_j^* itself is an average of a large number of measurements N_{meas} within a single run. Table 3.1 contains typical values for these MC parameters that we used in different studies.

3.1.4 Parallelisation techniques

In the nowadays life all modern numerical calculations require to be parallel. It is especially true for the lattice MC simulations, where large spin systems must be simulated to perform a FSS analysis. Below we briefly observe methods of parallelising classical MC simulations and describe the methods, used in the present study.

As explained above measuring an observable in the MC scheme inevitably requires sampling of the phase space of the system and averaging the momentarily measured independent values. This independence, while being the big trouble of the importance sampling (see discussion below eq. (3.13)), is the key factor that stands behind the most straightforward parallelism idea. A machine with k cores can perform k parallel independent MC runs with different initial spin configurations that are averaged at the end. Such workload when almost no intertask communication is required is often called *embarrassing* or *perfect* parallelism. This method is sometimes criticised for the necessity of independent thermal equilibration of each run, which leads to the large total computation time spent on auxiliary thermalisation process. However, it is easy to implement via the MPI protocol and it naturally helps to independently explore the phase space. Moreover, embarrassing parallelism is the natural one to use for simulation of the system with structural disorder as it involves one additional level of averaging over many random impurity configurations at the last step.

Another technique that can be applied for parallelising the MC workload is called checkerboard decomposition or *sublattice* parallelisation. If a lattice can be split into n_{subl} equal sublattices, such that the spins on one sublattice do not interact with each other, then single spin updates of all spins on this sublattice can be performed in parallel. Indeed, in this case an update of a spin does not distort the local fields h_i of other spins on the same sublattice and does not affect the acceptance probability of parallel updates. For example, the nearest neighbour cubic, triangular and pyrochlore magnets may be divided into 2, 3 and 4 sublattices respectively. Moreover, the model does not have to be restricted to nearest neighbour exchange, but in that case the number of sublattices will increase. The procedure is performed as follows: one sublattice $\alpha^{(k)}$ is chosen, and a Metropolis update is performed simultaneously on all or any number of spins on that sublattice $S_{i\in\alpha^{(k)}}$. Then another $\alpha^{(k+1)}$ is taken. One important thing to remember is that every time sublattices should be picked randomly in order to preserve detailed balance.

When choosing a way to parallelise the MC run, one should always take into account the architecture of the computational cluster, where the code will be run as there is no general ideal way to parallelise the workload. Moreover, one should remember that parallelisation may also help to solve a directly unrelated problem of optimising the memory usage of the machine.

A typical state of the art classical MC spin simulation is done on a system of $N \lesssim 10^5$ three-component spins. Coded as a double precision array of real numbers, it requires about 1 MB of memory. Such a MC run can almost entirely fit into the cache of a common CPU. However, despite the obvious low use of memory, the MC task may be surprisingly not entirely CPU-bound. Depending on the size of the spin system different amounts of L2 and L3 cache is needed for different simulations. As the access speed to these memory supplies is very different, an optimised memory usage gives a considerable increase of computational speed even for such a low in memory task. It can be especially interesting for the machines with NUMA architecture, where several CPUs, share the same high-level cache. On such machines sublattice parallelisation may be preferable to parallel tempering or embarrassing parallelisation.

3.1.5 Technical details of the realisation

Finally, we present the general scheme of our MC simulations, with minor alterations it was used in all our studies. Our simulations were made on the *Meso* calculation server of the Theory Group of INAC/SPSMS. The cluster consists of 23 nodes, each contains 48 800 MHz AMD Opteron 6176 CPU with 512kB L2 cache. The CPUs are grouped into 8 NUMA nodes (Non Uniform Memory Access) with 6 cores on each node, which share 5 MB of common L3 cache memory. This architecture proposes natural units for parallelisation: sublattice parallelisation was done on one NUMA node in 6 threads using OpenMP specification. Therefore, MC simulations of even the biggest cluster sizes fit entirely into the cache of one NUMA node, thus optimising the memory usage in addition to parallelising the task. $8 \times k$ replicas of the system were simulated in parallel using the embarrassing parallelisation scheme (k stands for the number of nodes taken for the run).

Every run started by choosing randomly $N_{\rm imp}$ lattice sites to host vacancies, the corresponding spins were set to zero. Then a random initial spin configuration was generated. Starting deep in the paramagnetic phase we decreased temperature (or the magnitude of external field), measuring a set of observables $\{M_i\}$ for each value of parameter T (H).

Initial $N_{\rm equil}$ MCS were omitted to equilibrate the system for each T (or H), then $N_{\rm meas}$ momentary snapshots of the system were used to obtain an estimate of the order parameters (3.1). After each measured snapshot $5-10$ MCS, alternating with several overrelaxation sweeps were made to drive the system to a distinct state. Every MCS consisted of $n_{\rm subl}$ single-spin Metropolis updates of all spins on one sublattice. Each time a sublattice was chosen randomly, and all the updates were performed in parallel.

Upon finishing the sweep over the desired parameter range, the procedure was repeated $N_{\rm repl}$ times for different random impurity replicas. The final values for the observables and the error bars were taken from this last averaging over disorder realisations. In the table 3.1 we list typical simulation parameters for different problems that are studied below in the manuscript.

3.2 Finite Size Scaling

There is absolutely no possible way to perform numerical simulations of the clusters that are as big as real experimental samples. All the lattices that are reachable by current numerical

	N	N_{meas}	N_{equil}	N_{repl}
HTAFM	$L^2, \quad L \leq 150$	$2 \cdot 10^5$	$0.4 \cdot 10^5$	96×1
XY pyrochlore	$4L^3, \quad L \leq 16$	$2 \cdot 10^5$	$1.5 \cdot 10^5$	96×1
XY pyrochlore in field	$4L^3, \quad L \leq 24$	$3.5 \cdot 10^5$	$3 \cdot 10^5$	1×96
120° model	$L^3, \quad L \leq 30$	$1.5 \cdot 10^5$	$2.7 \cdot 10^5$	24×24
2D 90° model	$L^2, \quad L \leq 100$	$2 \cdot 10^5$	$2.8 \cdot 10^5$	20×24
3D 90° model	$L^3, \quad L \leq 40$	$2 \cdot 10^5$	$2 \cdot 10^5$	18×24

Table 3.1: Parameters of Monte Carlo simulations of various problems in the study. In the last column number of different impurity realisations and a number of independent runs for each replica is given.

techniques are essentially final and by far small. There are two types of problems, associated with the finite lattice size. The first type of errors is due to boundary conditions. And the second, is the mismatch between the true phase transition temperature T_c and the temperatures $T_c(L)$, where singularities are observed for the system with characteristic length scale L.

Luckily $T_c(L)$ deviates from true T_c in a controllable way, and by studying $T_c(L)$ for different cluster sizes one can predict the infinite lattice phase transition point $T_c(L = \infty) = T_c$. Therefore, what seems to be a problem in fact can be turned into an incredibly powerful tool. The theory and the set of methods that treat the effects of finite lattice sizes is called *Finite Size Scaling* (FSS). In this section we will present a brief overview of the methods that we used to estimate critical temperatures of different phase transitions from our MC data.

Finite size scaling theory is especially powerful in the case of the II-nd order type phase transitions. In subsection 3.2.1 we present the brief introduction to the theory and show T_c and different critical indices can be extracted from finite size data. In the next subsection 3.2.2 we treat the case of discontinuous phase transitions. Finally, the complex phase diagram of the Heisenberg antiferromagnet on a triangular lattice contains several phases with algebraic order and Berezinsky-Kosterlitz-Thouless (BKT) phase transition. So subsection 3.2.3 is devoted to the FSS methods in the context of BKT transition.

3.2.1 Second-order transition

It is known from statistical physics that the correlation length diverges as the critical temperature of the II-nd order phase transition is approached $\xi \propto \tau^{-\nu}$. Here $\tau = |T - T_c|/T_c$ is the reduced temperature. However, in the finite lattice simulations the correlation length cannot be larger than L - the characteristic size of the system. Moreover, a finite system becomes critical already when $\xi = L$. At this point the observables, such as χ and C saturate and exhibit a rounded peak, instead of a true divergence. What makes matters worse is that it happens at the pseudocritical temperature $T_c(L) > T_c$, which depends on L. Using the scaling anzatz for the free energy F and the idea that the only way F can depend on L is via the dimensionless parameter $L/\xi \propto L\tau^{\nu}$ we will obtain methods of finite size analysis.

We are interested in the critical behaviour of the system in the vicinity of the phase transition, which can be extracted from the singular part of the free energy. According to the finite size scaling theory [41, 42] its size dependence is described by the scaling anzatz of the following form

$$F(L,T,H) = L^{-(2-\alpha)/\nu} F\left(\tau L^{1/\nu}, H L^{(\gamma+\beta)/\nu}\right), \tag{3.15}$$

where α, β, γ are critical exponents. Differentiating this function and setting $H = 0$ one gets the scaling form of various thermodynamic functions:

$$\begin{aligned} M(L,T) &= L^{-\beta/\nu} M_0(\tau L^{1/\nu}); && (3.16)\\ \chi(L,T) &= L^{\gamma/\nu} \chi_0(\tau L^{1/\nu}); && (3.17)\\ C(L,T) &= L^{\alpha/\nu} C_0(\tau L^{1/\nu}), && (3.18) \end{aligned}$$

where M_0, χ_0 and C_0 are fixed scaling functions. Here we also used a hyperscaling relation between the critical exponents $d\nu = 2 - \alpha = \gamma + 2\beta$. The main result is rather straightforward: exactly at phase transition $\tau = 0$, and the whole size dependence reduces to universal power law behaviour.

$$M_c(L) \propto L^{-\beta/\nu}, \qquad \chi_c(L) \propto L^{\gamma/\nu}, \qquad C_c(L) \propto L^{\alpha/\nu}. \tag{3.19}$$

According to the equations (3.9) and (3.10) these functions are nothing but first or second order moments of the order parameter or energy probability distributions. Similarly, one can consider fourth and higher order moments. It turns out that it is especially convenient to study the ratio of the kind $\langle m^4\rangle / \langle m^2\rangle^2$ because in this case for $\tau = 0$ the power law prefactor $L^{-\beta/\nu}$ gets cancelled, and the ratio becomes size independent. This approach was proposed by Kurt Binder and the corresponding quantity is known as Binder cumulant of the order parameter [43]

$$U_B = 1 - \frac{\langle m^4\rangle}{3\langle m^2\rangle^2}. \tag{3.20}$$

Before proceeding to the application of the FSS theory, we note that the form of scaling anzatz (3.15) is subject to additional corrections away from T_c or when system size L is not sufficiently large [44, 45].

Thus we obtain a way to extract the value of the transition temperature and critical exponents. T_c is usually obtained as the abscissa of the common intersection of $U_B^{(L)}$ when the set of functions is plotted against T. Then this estimate can be used for estimating critical exponents. First one extracts ν by plotting $U_B^{(L)}$ as a function of $\tau L^{1/\nu}$. Varying ν, one aims for the collapse of all curves to a single function. As the last step of the FSS procedure one plots a set of functions $M(L,T) \cdot L^{\beta/\nu}$ against the same combination $\tau L^{1/\nu}$ in the vicinity of the phase transition with β as an external parameter, which is being varied. All the curves merge for the correct β. Other indices are extracted in the same way using equations (3.17) and (3.18).

We note that in this work we used a less sophisticated procedure of obtaining the critical exponents. It involves plotting functions $M(L,T) \cdot L^{\beta/\nu}$ simply against T. The functions become independent of the system size exactly at $T = T_c$ for the correct value of β/ν. So varying the exponent ratio we looked for the best curves crossing and thus estimated the exponents.

3.2.2 First-order transition

The behaviour of the observables in the first order transition is very different from the continuous transition, considered before. The correlation length ξ does not diverge, instead, the energy of the system and the order parameter exhibit a finite jump, therefore there is no sense in describing the transition in terms of critical indices. But the problem of smearing of the singularities and the extraction of precise transition temperature in the finite system still exists. Good reviews of methods of extracting transition temperatures from MC simulations are made by Janke [46] and Binder [47]. Below we present the methods that were used in this work.

In the finite system no sharp singularities can develop. The jumps of E and M become smooth crossovers, ant the δ-like singularities of χ and C exhibit slightly displaced smooth peaks. The main and the only scaling parameter for the I-st order transition is the volume of the system: the height of the specific heat peak $C_c(L)$ is proportional to L^d, and its position $T_c(L)$ scales with inverse volume [48]. Therefore, to obtain the estimate of the infinite system transition temperature one can plot $T_c(L)$ against V^{-1} and linearly extrapolate to $V \to \infty$.

Often in the work we faced a problem of defining the type of transition in the first place, and determining transition temperature. For this purpose it is convenient to use Binder cumulant of energy $V_B = 1 - \frac{\langle E^4 \rangle}{3\langle E^2 \rangle^2}$. It has a specific feature: a minimum, which is absent in the case of the II-nd order transition. Similarly to specific heat peak, the position of the minimum also scales with inverse volume $1/L^d$.

The usual way of obtaining the critical temperature of the first order phase transition is by examining the distribution function of the order parameter or energy. Close to T_c it has the form of the sum of two Gaussian distribution functions around equilibrium values of the order parameter $M_\pm$ with different weights $\rho_\pm$:

$$P(M) = \rho_+ P_G(M_+) + \rho_- P_G(M_-). \tag{3.21}$$

These weights become equal exactly at $T = T_c(L)$. This method is rather cumbersome and we only used it used as an evidence for the I-st order transition type rather than to exact transition determination.

3.2.3 Berezinsky-Kosterlitz-Thouless transition

A BKT transition is associated with the formation of topological defects - binding-unbinding of spin vortices. Therefore, it is natural to describe the system with spin stiffness or helicity modulus. It is by definition the elasticity coefficient against a small nonuniform rotation of spins $\varphi(\mathbf{r}) \to \varphi(\mathbf{r}) + \delta\varphi(\mathbf{r})$ around a fixed direction [49]

$$\rho_S = \left. \frac{\partial^2 F\left(\delta\varphi\right)}{\partial\left(\delta\varphi\right)^2} \right|_{\delta\varphi=0}. \tag{3.22}$$

Exactly at $T = T_c$ ρ_S exhibits a finite universal jump of the magnitude $\rho_S = 2T_c/\pi$.

Scaling theory for the spin stiffness in the BKT transition predicts logarithmic corrections for small L [50]

$$\rho_S(T, L) = \rho_S(T, \infty) \left[1 + \frac{1}{2\ln L + C} \right]. \tag{3.23}$$

The way to proceed is then the following: for each of the available lattice sizes find $T_c(L)$, such that $\rho_S(L) = 2T_c(L)/\pi$, then interpolate obtained values with the function $T_c(L) = T_c\left[1 + (2\ln L + C)^{-1}\right]$ and obtain T_c as one of the fitting parameters.

3.3 Mean-field minimisation

Another numerical technique that is widely used in our studies is an energy minimisation algorithm for a classical spin system. It can be used to find numerically the mean-field ground state of a frustrated system. It is especially useful for the systems with structural disorder when analytical methods that use translational symmetry break down.

3.3.1 Description of the method

The core of the method lies in the possibility of expressing the energy of the system via the local fields $\mathbf{h}_i$ that are independent of the corresponding spin $\mathbf{S}_i$

$$E = -\sum_i \mathbf{S}_i \cdot \mathbf{h}_i; \qquad \mathbf{h}_i = -\sum_{j=1}^{z} J_{ij}\mathbf{S}_j + \mathbf{H}. \tag{3.24}$$

Here the sum runs over all spins that interact with $\mathbf{S}_i$, not only limited to the nearest neighbours. Then for any spin configuration setting $\mathbf{S}_i \parallel \mathbf{h}_i$ will decrease the energy of the system. Repeating the procedure iteratively for all spins leads to convergence to a minimum of the energy.

This method is fundamentally similar to the gradient descent optimisation method, where at each step the energy function is minimised with respect to a fixed part of coordinates of the full phase space. Therefore, this method can be generalised for the case of a local field that depends on the corresponding spin $\mathbf{h}_i = \mathbf{h}_i(\mathbf{S}_i)$. It is the case, for example, for the system with single site anisotropy term $\Delta H = D\sum_i S_i^{z2}$ or biquadratic interaction $\hat{V} = \sum_{\langle i,j\rangle} K_{ij}\left(\mathbf{S}_i \cdot \mathbf{S}_j\right)$. At each step one should take

$$\mathbf{S}_i = -\frac{\nabla_i E}{|\nabla_i E|}; \qquad \nabla_i E = \frac{\partial E}{\partial \mathbf{S}_i}. \tag{3.25}$$

An important question, concerning this method is the choice of initial conditions. The algorithm is deterministic, and for each initial spin configuration will converge to one minimum of energy. If the energy landscape is rough, as in the case of systems with impurities, it may contain a lot of local extrema. Therefore, one needs to sample a lot of initial spin configurations and choose a global minimum of energy among them. In addition to completely random initial conditions, we included several imposed spin configurations that were usually taken from the studied manifold of states. We compared the results with the random initial conditions on equal rights.

To sum up, our protocol was the following: starting from an initial condition, we solve iteratively the local energy minimum condition (3.25) for a randomly chosen spin. After every spin was sampled, a convergence condition was checked, which usually consisted of $\sum_i \|\mathbf{S}_i^{(k+1)} - \mathbf{S}_i^{(k)}\| < \delta$ with $\delta \simeq 10^{-6}N$. The iterations were repeated until the criterion was met. Then energy and all necessary order parameters were measured and the whole procedure repeated for another initial configuration. A global minimum of energy corresponding to each impurity replica was chosen afterwards. The final data are produced by averaging over the lowest energy magnetic structures obtained for each impurity set.

The method allows for some optimisation. First, it was noted that the convergence is reached faster if instead of the true gradient descent, (3.25) a partial step is taken: $\mathbf{S}_i^{(k)} \parallel \alpha\nabla_i E + (1-\alpha)\,\mathbf{S}_i^{(k-1)}$ with gradually growing $\alpha \to 1$. Also, as long as the Hamiltonian contains only nearest neighbour interactions, a *sublattice parallelisation* algorithm can be applied to improve the performance on parallel architectures. However, as our problems included averaging over a large number of impurity replicas, a simpler *embarrassingly parallel* scheme was usually used. For more details on parallelisation techniques refer to section 3.1.4.

Chapter 4

Dilution in triangular antiferromagnets

The antiferromagnet on a two-dimensional triangular lattice is a paradigmatic example of a frustrated system. Continuous Heisenberg and XY spin models attract considerable research interest for 30 years since pioneering works by Kawamura and Miyasita [28, 35, 51] and Lee, Joannopoulos, Negele and Landau [49, 52]. With the help of spin-wave analysis and Monte Carlo simulations these groups obtained incredibly rich phase diagrams of the classical models. Their most prominent common feature, the magnetisation plateau around $H \approx \frac{1}{3}H_s$, was observed in a number of compounds, for example, $\mathrm{RbFe(MoO_4)_2}$ [3, 4], $\mathrm{Cs_2CuBr_4}$ [5, 53] and $\mathrm{Ba_3CoSb_2O_9}$ [54, 55].

This up-up-down (uud) configuration, which is often loosely called a plateau phase, and in general the phase diagram of the pure models can be theoretically explained by the concept of order by disorder. In the magnetic field the clean classical TAFM exhibits an accidental degeneracy of ground states, consisting in an arbitrary orientation of the spin plane with respect to field direction. However, these states have different energy of thermal fluctuations, analytically it is realised by the action of a phenomenological biquadratic exchange.

We show that structural disorder in its various realisations can also lift the ground state degeneracy. Moreover, it favours the *least* collinear conical state. Such selection takes place because of the positive biquadratic exchange produced by structural disorder. In section 4.2 we derive it analytically, minimising the energy of the tilted spin states. In addition, our extensive Monte Carlo simulations show how the $H-T$ phase diagram is influenced by introducing a finite concentration of vacancies.

Section 4.3 contains our second result: a nontrivial substantial growth of an effective impurity moment m_{imp} upon increasing the fraction of vacant sites n_{imp}. In noncollinear magnets even in the absence of the external magnetic field an impurity induces a transverse local field on its neighbours and leads to the screening of magnetic moment of a missing spin. Wollny *et al.* [16] found that in the Heisenberg TAFM the magnetic moment around a vacancy is equal to $m_{\text{imp}}^{\circ} = 0.039S$. Our numerical results show deviation of m_{imp} from the independent impurity behaviour even at smallest studied $n_{\text{imp}} \leq 1\%$. We explain the observed tendency by the effects of clustering of impurities.

Our main system under study in this chapter is an isotropic Heisenberg model. However, the results can be also applied to the easy-plane TAFM, which is more relevant for experimental studies. In the last section 4.4 we discuss specific features of order by structural disorder in the XY triangular antiferromagnet.

4.1 Heisenberg triangular antiferromagnet: the model

We study the isotropic nearest-neighbour antiferromagnet in external field H

$$\hat{\mathcal{H}} = J \sum_{\langle ij \rangle} \mathbf{S}_i \cdot \mathbf{S}_i - \mathbf{H} \cdot \sum_i \mathbf{S}_i. \tag{4.1}$$

with spins $\mathbf{S}_i$ located at the vertices of an ideal two-dimensional triangular lattice. The geometry of the system allows decomposition of the Hamiltonian into a sum over elementary triangular blocks or plaquettes with three spins $\mathbf{S}_A$, $\mathbf{S}_B$, $\mathbf{S}_C$, belonging to the plaquettes. The quantity of interest is then a total magnetisation of a triangular block $\mathbf{S}_\triangle = \mathbf{S}_A + \mathbf{S}_B + \mathbf{S}_C$, as the Hamiltonian can be expressed through it

$$\hat{\mathcal{H}} = \sum_\triangle \frac{1}{4} \left[J\mathbf{S}_\triangle^2 - \frac{2}{3}\mathbf{H} \cdot \mathbf{S}_\triangle - J\left(\mathbf{S}_A^2 + \mathbf{S}_B^2 + \mathbf{S}_C^2\right) \right]. \tag{4.2}$$

The last term is constant, so the energy minimum condition corresponds to a constraint on a total spin of this block:

$$\mathbf{S}_\triangle = \frac{\mathbf{H}}{3J}. \tag{4.3}$$

This simple equality has several important consequences [28, 52]. First, the value of saturation field $H_S = 9JS$ follows directly from it. Also, equation (4.3) allows simple calculation of the local magnetic field, felt by a spin from the interaction with its neighbours and external field

$$\mathbf{h}_i = \frac{\partial E_{\rm GS}}{\partial \mathbf{S}_i} = \sum_{j=1}^{6} \frac{1}{2} JS\mathbf{n}_i = 3JS\mathbf{n}_i, \tag{4.4}$$

as only the last term in (4.2) contributes to $\mathbf{h}_i$. This means that the magnitude of the local field is independent of lattice site and of H. Of course the mean-field description assumes that each spin is pointing along its local field $\mathbf{S}_i \parallel \mathbf{h}_i \parallel \mathbf{n}_i$.

A three-spin configuration, which satisfies (4.3) on a simple plaquette is directly extended over the whole lattice. Indeed, all neighbouring triangles share two out of three spins, say $\mathbf{S}_A$ and $\mathbf{S}_B$. Then their third spins should be equal to $\mathbf{S}_C = \mathbf{H}/3J - \mathbf{S}_A - \mathbf{S}_B$. This constitutes a three sublattice ordering with a wave vector $\mathbf{Q} = (4\pi/3, 0)$.

Last but not least, a vector equation (4.3) imposes three constraints on the ground state configuration. Formed by three vector spins with six coordinate angles the ground state then has three undetermined degrees of freedom. They represent an arbitrary orientation of the spin plane in the spin space and a concrete orientation of one sublattice in this plane.

In the absence of Zeeman term this symmetry of the ground state is an exact $SO(3)$ rotation symmetry of the pure exchange Hamiltonian (4.1). The famous 120° structure, arbitrarily oriented in the spin space is the lowest energy configuration at $T = 0$. It is important to note that due to the Mermin-Wagner theorem [56] this continuous symmetry cannot be broken at finite temperature.

When the magnetic field is present $0 < H < H_S$, the Hamiltonian has only the $S^1 \otimes \mathbb{Z}_3$ symmetry. It is invariant under the rotation around the direction of magnetic field and permutations of three sublattices. There is no symmetry operation, related to other two continuous degrees of freedom. Such symmetry of the lowest energy states is called emergent symmetry, and is an artefact of the mean-field treatment of the model.

As an illustration of this phenomenon in Fig. 4.1 (a) - (f) we present various spin structures that can be realised in the Heisenberg triangular antiferromagnet in the magnetic field [49, 51].

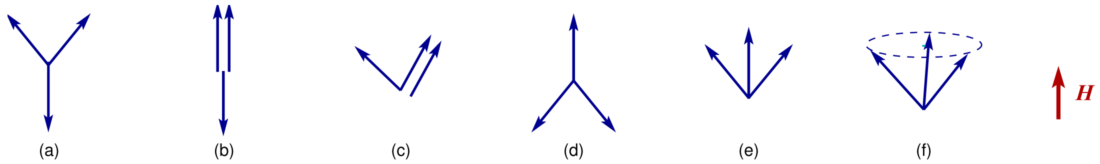

Figure 4.1: Ordered magnetic states of a TAFM in an external field. Spin configurations appearing for the TAFM without impurities: (a) coplanar Y-state, (b) collinear *uud* state, and (c) coplanar 2:1 (V) state. Spin configurations in the presence of nonmagnetic impurities: (d) anti-Y state and equivalent (e) fan state of the XY TAFM and (f) conical (umbrella) state of the Heisenberg TAFM.

For a certain fixed value of H several different spin configurations may have the same energy. For example, at $H = 3J$ a so called 1/3 magnetisation plateau or up-up-down state (b) can be formed as well as a fan structure with a right angle (e) or a noncoplanar cone (umbrella) structure (f), or any other from a two-dimensional continuous manifold of states. We note that the anti-Y (d) and the fan state (e) are equivalent from the symmetry point of view. They comprise different realisations of the same phase at different H smoothly connected via the 90° configuration at $H = 3J$.

4.2 Order by Structural disorder in the Heisenberg TAFM

The accidental degeneracy of the ground state manifold is lifted when one takes into account terms beyond the mean-field approximation. For example, one can consider spin waves around different ground states in the harmonic approximation. Calculation of the spectrum produces a correction to the energy or the free energy of the system, this mechanism is called order by disorder. In this section we address the problem of ground state selection in the Heisenberg triangular antiferromagnet by an alternative approach.

First, using the perturbation expansion in real space, introduced in the previous chapter, in subsection 4.2.1 we show that the effect of thermal and quantum fluctuations can be described by an effective biquadratic interaction term in the Hamiltonian. Since the celebrated work of Shender [2] biquadratic exchange is known to realise order by disorder in many collinear frustrated magnets. It is even proposed to emulate a quantum system in classical numerical simulations at low T [26, 57]. However, for noncollinear magnets, including the Heisenberg TAFM it was only presented phenomenologically. So derivation of the biquadratic exchange adds to the completeness of the theoretical description of the model.

Nevertheless, the main results of this section (and arguably, of the whole chapter) are presented further. In subsection 4.2.2 we show that the average gain of energy due to the vacancy-induced spin relaxation is different for degenerate states. So structural disorder can also lift the ground state degeneracy and its impact on the manifold can be represented by exactly the same biquadratic exchange anisotropy but with the opposite sign. Therefore, the true ground state of the system with defects is a result of the competition of the two opposite effects.

These conclusions are confirmed by the numerical simulations of the system with missing spins. Subsection 4.2.3 shows that, indeed, the least collinear state is selected by vacancies at $T = 0$. While Monte Carlo phase diagram of the system with $n_{\text{imp}} = 5\%$ of static vacancies, presented in sec. 4.2.4 supports the scenario of competition of biquadratic exchanges with different signs. Critical properties of the phase transitions are discussed and illustrated in the following section 4.2.5. In the last part of the section we discuss a possibility of observation of the disorder-induced phase in a real system.

4.2.1 Order by fluctuations

Real space perturbation expansion is a method of a perturbative treatment of the terms beyond the mean-field, which can be represented by different types of interactions of spin fluctuations on different sites. Using this method, which was presented in detail in chapter 2, we obtain the leading in $1/z$ corrections to energy due to thermal and quantum fluctuations of spins. In fact, as the exemplary calculations of chapter 2 were made on the TAFM, we directly use the results, obtained earlier and discuss the physical sense behind the expressions.

In a pure system at finite temperature the entropy of the degenerate states is different. In the leading order in $1/z$ thermal fluctuations can be represented by an effective biquadratic term in the free energy (2.14)

$$\Delta F = -\frac{T}{18S^4}\sum_{\langle ij\rangle}(\mathbf{S}_i\cdot\mathbf{S}_j)^2\,. \tag{4.5}$$

In the case of quantum spins a similar biquadratic term appears as the result of quantum fluctuations around the ground states (2.19)

$$\Delta E = -\frac{J}{24S^3}(\mathbf{S}_i\cdot\mathbf{S}_j)^2\,. \tag{4.6}$$

Both of the terms describe the interaction of fluctuations on neighbouring sites and come from the second order of perturbation theory: classic or quantum.

Equations (4.5) and (4.6) realise the fact that fluctuations favour the most collinear spin structures from the degenerate manifold of frustrated triangular antiferromagnet. It was observed by classical [28, 49] and quantum [27] spin-wave theory and by different numerical simulations [35, 49].

The evolution of phases of the model [35, 58, 59] is perfectly described by the effective biquadratic exchange alone. In figure 4.2 we present the Monte Carlo phase diagram of Gvozdikova *et al.* [58]. Its main features can be understood solely by considering the biquadratic anisotropy: 1) Coplanar configurations are favoured over the noncoplanar conical ones. 2) The most collinear *uud* structure produces the strongest correction. This explains an extent of the plateau phase to low fields at higher temperatures. 3) Y and V phases are favoured over their symmetrical counterparts - anti-Y phase and the fan phase (Fig. 4.1 (d) and (e)).

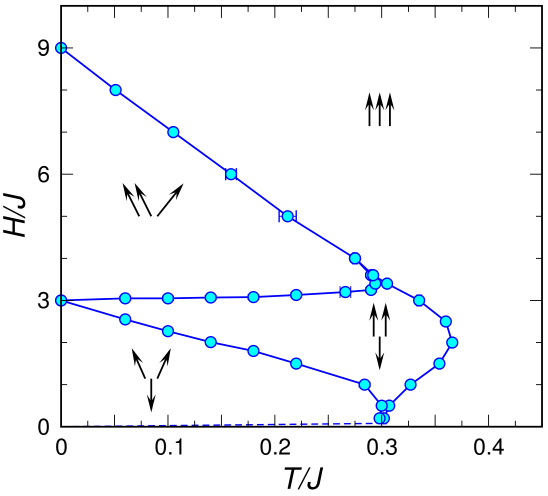

Figure 4.2: Monte Carlo $H-T$ phase diagram of a pure Heisenberg triangular antiferromagnet, obtained by Gvozdikova *et al.* [58].

While presenting the details of RSPT we have also shown that higher order corrections also lift the ground state degeneracy. But they are smaller by at least an additional $1/z$ factor, so they renormalise the order by disorder strength and introduce other weaker effective interactions, but do not affect the overall state selection tendency.

4.2.2 Ground state selection by structural disorder

Defects in magnetic structure violate locally perfect geometrical frustration, so the surrounding spins reorganise and gain in energy. This energy gain may vary in different states of the degenerate manifold. Below in a limit of weak disorder, we minimise the energy of the system with defects and obtain the effective corrections to the Hamiltonian that characterise different energy gains.

In section 2.2 we have presented the model of weak impurities. In this model a small fraction of randomly distributed spins $n_{\text{imp}} \ll 1$ is set to have smaller length $S^{(\text{imp})} = S(1-\epsilon)$ with $\epsilon \ll 1$. This approximation is analogous to restricting the impact of impurities to its nearest neighbours only and suits more for the analytical calculation than true vacancies.

The calculation of energy correction from the weak vacancies was done in eq. (2.26) - (2.35), the result can be expressed as

$$\Delta E = \frac{J\epsilon^2 n_{\text{imp}}}{3S^2} \sum_{\langle ij \rangle} (\mathbf{S}_i \cdot \mathbf{S}_j)^2 \,. \tag{4.7}$$

Therefore, a small finite concentration of weak vacancies may be described by a positive biquadratic exchange.

A very similar result was obtained for another physically relevant model of quenched disorder - a weak bond disorder. It is modelled by a variation of exchange constants $J \to J(1+\delta_{ij})$, with unbiased small random $\langle\langle \delta_{ij}^2 \rangle\rangle = D \ll 1$. In this case the energy correction depends on the ground state in the same way as for weak impurities and we have

$$\Delta E = \frac{DJS^2}{3S^2} \sum_{ij} (\mathbf{S}_i \cdot \mathbf{S}_j)^2 \,. \tag{4.8}$$

The energy corrections, generated by structural disorder have the same functional form, as (4.5) and (4.6), but the opposite sign. Therefore, structural disorder favours the *least* collinear structures in the ensemble of degenerate classical ground states. Selection of orthogonal or *anticollinear* ground states was previously known in the context of the diluted J_1–J_2 square-lattice antiferromagnet [22, 24] yet the tendency determined by (4.7) is rather general, see also refs. [21, 26] with similar conclusions.

4.2.3 Numerical determination of ground state at $T = 0$

To confirm the conclusion of the previous subsection that structural disorder robustly selects the least collinear conical states from the degenerate continuous manifold we have used different numerical techniques. First, we present the results of our energy minimisation algorithm, which searches for the ground state of the system at $T = 0$. In numerical simulations there is no need for structural disorder to be weak, so we performed all our runs on the systems with real spin vacancies. For every run a fixed number $N_{\rm imp} = n_{\rm imp}N$ of spins was set to zero, and every measurement is the result of averaging over 96 random impurity replicas.

The numerical minimisation algorithm was described in section 3.3. For each of 10^3 random initial spin configurations a local energy minimum was deterministically found, and a global ground state was then selected. Ground-state configurations of the TAFM in the magnetic field are characterised by the antiferromagnetic order parameter:

$$\mathbf{M}_Q = \frac{1}{N}\sum_i \mathbf{S}_i e^{-i\mathbf{Q}\mathbf{r}_i}. \qquad (4.9)$$

In particular, the conical state is unambiguously distinguished from the coplanar configurations by a finite $M_Q^\perp = (|M_Q^x|^2 + |M_Q^y|^2)^{1/2}$ and $|M_Q^z| = 0$.

Numerical results for transverse and longitudinal components of staggered magnetisation at $H/J = 3$ are shown in Fig. 4.3. The conical state remains stable for all studied impurity concentrations including the smallest one $n_{\rm imp} = 0.1\%$. The lack of appreciable finite-size effects in $M_Q^\perp$ indicates the absence of a spin-glass phase and the development of the true long-range

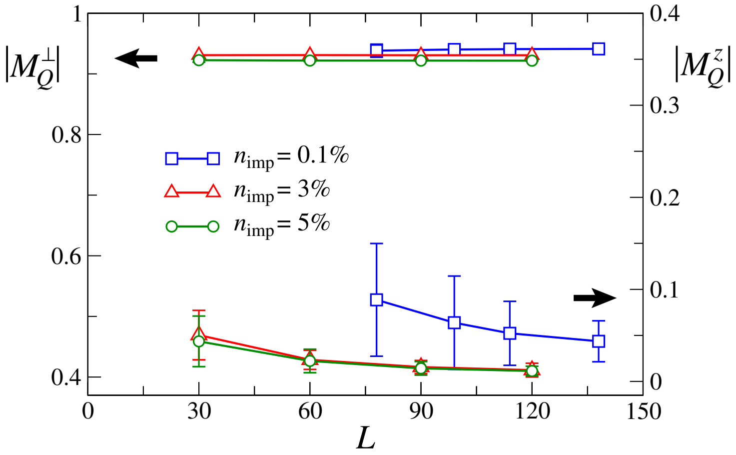

Figure 4.3: Zero-temperature transverse $|M_Q^\perp|$ and longitudinal $|M_Q^z|$ antiferromagnetic order parameters at $H/J = 3$ for clusters with different concentration of vacancies $n_{\rm imp}$ and different linear size L.

order in transverse components. Large error bars in $|M_Q^z|$ indicate that a larger number of impurity replicas has to be sampled when the number of vacancies is small. A similar behaviour is found for all $0 < H < H_s$ although with more iteration steps being required for $H \to 0$. Hence, the numerical results for the diluted TAFM fully corroborate the analytical findings of the previous subsection.

4.2.4 Phase diagram of HTAFM with impurities

In a classical model, two types of disorder, thermal and quenched, lift the ground state degeneracy, but select opposite spin configurations. They compete with each other producing a rich $H - T$ phase diagram, so we have performed the classical Monte Carlo simulations of the diluted TAFM in order to capture their cumulative effect on the frustrated system. The hybrid algorithm, presented in chapter 3 was employed in a wide range of temperatures and magnetic fields. Physical quantities and associated error bars were estimated from averaging over 96 impurity replicas. Phase transition boundaries were determined by the standard finite-size scaling analysis of clusters with linear sizes up to $L = 150$.

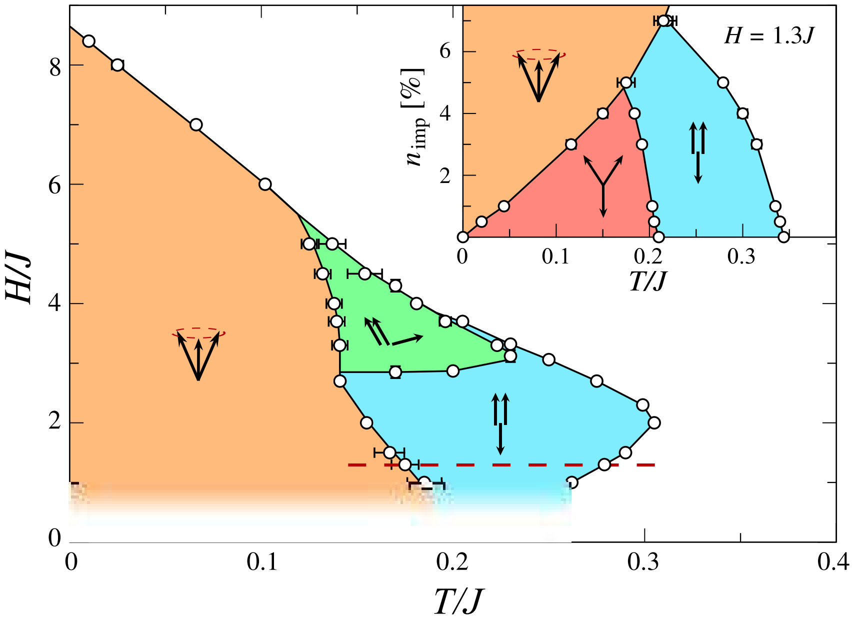

Figure 4.4: Classical Monte Carlo phase diagram of the Heisenberg TAFM with 5% of nonmagnetic impurities. Solid lines that connect data points are guides for the eye. The inset shows the concentration evolution of the ordered phases for $H/J = 1.3$, which is indicated by the dashed line on the main panel.

The magnetic phase diagram of the Heisenberg TAFM with 5% of vacancies is shown in Fig. 4.4. The main new feature in comparison with the diagram of the pure model (Fig. 4.2) is the emergence of the conical state at low temperatures for all $H \le H_S$. It is in absolute agreement with the scenario of competition of biquadratic exchanges with opposite signs (4.5) and (4.7). At high enough temperatures the increased thermal fluctuations overcome quenched disorder and magnetic phases of the pure TAFM reappear again, though the Y-phase remains absent for $n_{\rm imp} = 5\%$.

The phase transition boundaries are drawn down to $H/J \sim 1$. In lower magnetic fields, finite-size effects become stronger and require simulations of significantly larger lattices than those studied in our work. Therefore, we cannot exclude reappearance of the Y-phase at very low fields. Instead, we show the evolution of the phase boundaries with the vacancy concentration at fixed $H = 1.3J$ in the inset of Fig. 4.4. The Y-phase is present in this field for small n_{imp} and disappears at $n_{\text{imp}} \sim 4.5\%$. We note that we expect the absence of finite-T phase transitions at $H = 0$ in agreement with the Mermin-Wagner theorem, so all low H phase boundaries should end at the origin point of the diagram.

4.2.5 Phase transitions and critical properties

The effect of impurities on the critical behaviour of the TAFM can be assessed using the Harris criterion [60], which states that disorder becomes relevant for transitions with $\alpha = 2 - d\nu > 0$. In particular, the Berezinsky-Kosterlitz-Thouless (BKT) transition formally has $\nu = \infty$ and remains unaffected by vacancies as was confirmed numerically in [61]. The second-order transition into the *uud* state, which belongs to the universality class of the 2D three-state Potts model, has $\alpha = 1/3$ and is, therefore, driven by impurities to a new random fixed point, see [62, 63] and references therein. Nevertheless, the spin correlation exponent η stays very close to the clean value $\eta = 4/15$ [62] and we also found virtually no difference with the pure case for the critical behaviour of the order parameter at this transition in our Monte Carlo simulations.

In comparison with the pure system the phase diagram of the diluted model has an additional conical phase. In the high-field region $5J \lesssim H < H_s$ the direct transition from the paramagnetic to the conical state is accompanied by breaking of the $\mathbb{Z}_2 \otimes S^1$ symmetry, where $\mathbb{Z}_2$ describes chirality ordering. Therefore, this transition is similar to the one that occurs at the high field region of the pure system, where a continuous BKT and second order phase transitions occur very close to one another. Statistical errors in simulations brought by the impurities are too large to resolve a presumably tiny splitting of T_{BKT} and T_{chir} as well as an effect of the disorder on the Ising-like chiral transition.

At lower fields $H \lesssim 5J$ the transition from the planar phases to a conical state should be of the first order because of the different spin plane orientation on two sides of the boundary. However, a signature of the first-order transition was seen only for $2J \lesssim H < 3J$ from the scaling of the specific heat anomaly. At higher and lower fields the diluted TAFM shows fingerprints of a continuous transition between conical and coplanar states. We address it to a strong smearing of the first order transition by impurities, but allow another possibility: presence of an intermediate phase with the restored symmetry in a narrow temperature interval.

Below we illustrate these critical properties and, more generally, the determination of the phase boundary by presenting various FSS procedures in four different field ranges. First, we introduce various order parameters that help to distinguish different phases and determine precisely phase boundaries. Along with the usual antiferromagnetic order parameter (4.9), we used chirality, defined as a pairwise vector product of spins on one plaquette

$$\kappa = \frac{2}{3\sqrt{3}N} \sum_{\triangle} \big[\mathbf{S}_A \times \mathbf{S}_B + \mathbf{S}_B \times \mathbf{S}_C + \mathbf{S}_C \times \mathbf{S}_A\big]. \tag{4.10}$$

It vanishes when any two spins on an elementary triangle are parallel. Table 4.1 lists various phases that were observed in our study. The star signs in the corresponding cells denote quantities that have nonzero values in these phases. Longitudinal chirality $\varkappa^z$ is therefore especially practical in capturing the new conical phase, stabilised by impurities.

	Cone	Fan	Y	uud	V	PM
M_Q^z		$\star$	$\star$	$\star$	$\star$	
$M_Q^\perp$	$\star$	$\star$	$\star$		$\star$	
κ^z	$\star$					
$\kappa^\perp$		$\star$	$\star$			

Table 4.1: Components of staggered magnetisation $\mathbf{M}_Q$ and chirality κ, which were used to distinguish various phases in our MC simulations.

Precise phase boundary location was done using the finite-size scaling procedures, which were described in section 3.2. Particularly, Binder cumulant and susceptibility of the order parameters were used in determination of the discrete symmetry breaking

$$U_B = 1 - \frac{\langle M_Q^4 \rangle}{3\langle M_Q^2 \rangle^2}; \qquad \chi = \frac{N}{T}\langle M_Q^2 \rangle. \tag{4.11}$$

While scaling of spin stiffness (3.22) allowed the precise location of the BKT transition

$$\rho_s = -\frac{J}{N\sqrt{3}} \sum_{\langle i,j \rangle} \langle S_i^x S_j^x + S_i^y S_j^y \rangle \; - \; \frac{2J^2}{NT\sqrt{3}} \langle \Big[\sum_{\langle i,j \rangle} \left(S_i^x S_j^y + S_i^y S_j^x \right) (\hat{\mathbf{e}} \cdot \mathbf{r}_{ij}) \Big]^2 \rangle. \tag{4.12}$$

1) First, we present the results of the high field scan at $H = 6J$. We used scaling of κ^z, as shown in Fig. 4.5 (a) to locate the Ising transition and scaling of spin stiffness on panel (b) of the same picture to determine the BKT transition.

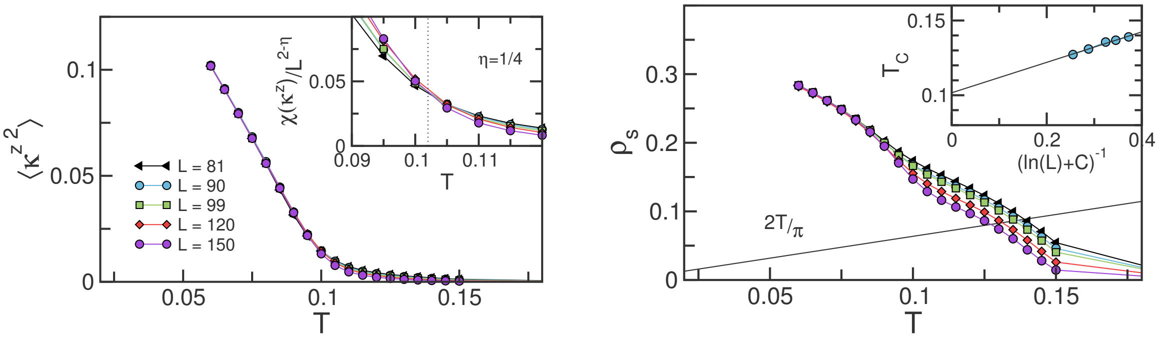

(a) Square of the longitudinal chirality $\kappa^{z\,2}$ - the order parameter of the conical phase. Inset: scaling of the corresponding susceptibility with the Ising critical exponent $\eta = 1/4$ gives the temperature of the phase transition.

(b) Determination of the BKT transition to the conical phase using scaling of spin stiffness. Finite lattice size transition temperatures $T_c(L)$ are obtained as the intersections with the $\rho = 2T/\pi$ line. Inset shows the fit with the two-parameter scaling function $T_c(L) = T_c\left(1 + (2\ln L + C)^{-1}\right)$. $C = -6.264$ was used.

Figure 4.5: Finite size scaling for $H = 6J$. $n_{\text{imp}} = 5\%$

2) When the magnetic field is below $H/J \lesssim 5$ some features of the pure phase diagram start to appear. In particular, an evolution into the conical phase happens via intermediate planar configurations. Figure 4.6 illustrates the phase evolution at $H = 4J$. The transition from the paramagnetic phase is determined like in the pure case by scaling of $\chi^{\perp}$ and ρ_s on panels (a) and (b). The weak first order phase transition T_c was defined as the crossing point of the different order parameter curves, as they exhibit weak inverse scaling behaviour. Panel (d) illustrates the absence of sharp features in the specific heat (3.9) We also note that in our field scans we observed a decrease of the $V - uud$ boundary of around 10%, compared to the pure case.

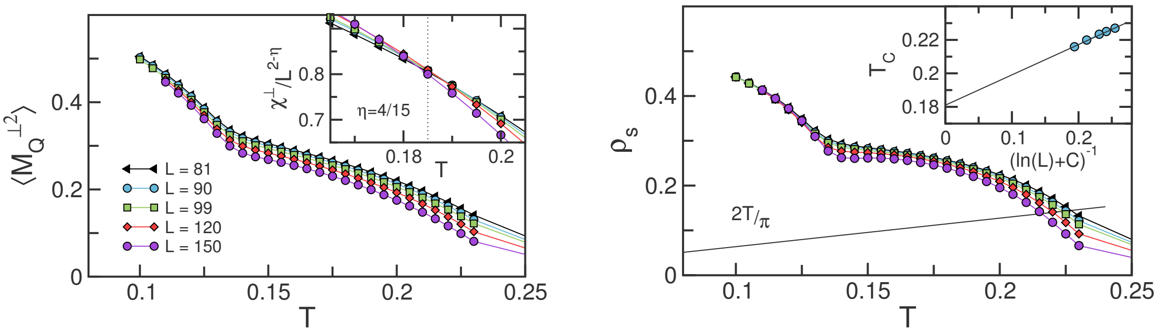

(a) Transverse component of staggered magnetisation and the corresponding susceptibility. 2D three-state Potts model critical exponent was used to determine the transition temperature $T_c = 0.185(5)$ to the V phase .

(b) Scaling of spin stiffness, as described in section 3.2.3 was used to determine the location of PM–V phase boundary. Fitting of intersection points gives $T_c = 0.181(2)$ and $C = -4.865$.

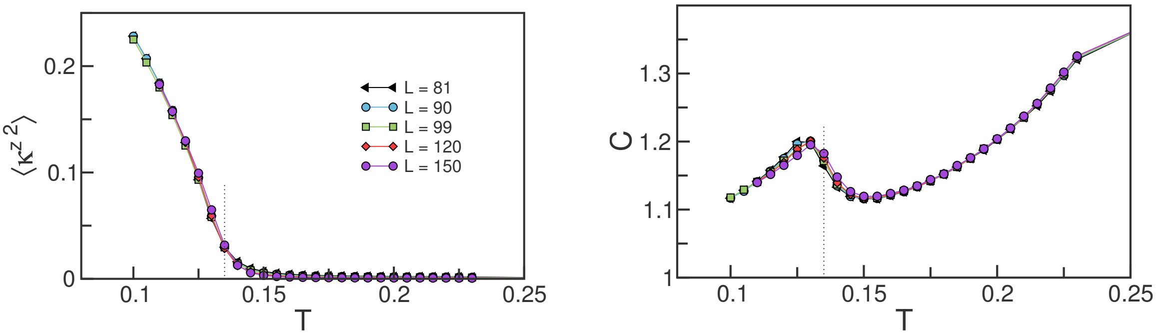

(c) Order parameter of the cone phase shows a rather continuous growth with almost no finite-size effects.

(d) Magnetic specific heat shows a broad cusp, instead of a first-order-like anomaly.

Figure 4.6: Finite size scaling for $H = 4J$. Top panels show the PM–V transition, bottom panels illustrate the transition to the impurity-induced cone phase. $n_{\mathrm{imp}} = 5\%$

3) The PM–*uud*–cone evolution at $H = 2J$ is shown in figure 4.7. In general the PM – *uud* phase boundary happens to be determined with the highest precision of all by the crossing of the Binder cumulants $U_b(M_Q^{\perp})$ (panel (b)). Scaling of susceptibilities, shown on the inset of panel (a) confirms the estimate of T_c. The lower transition in the intermediate field range shows the sharpest first order features, as seen on panels (c) and (d).

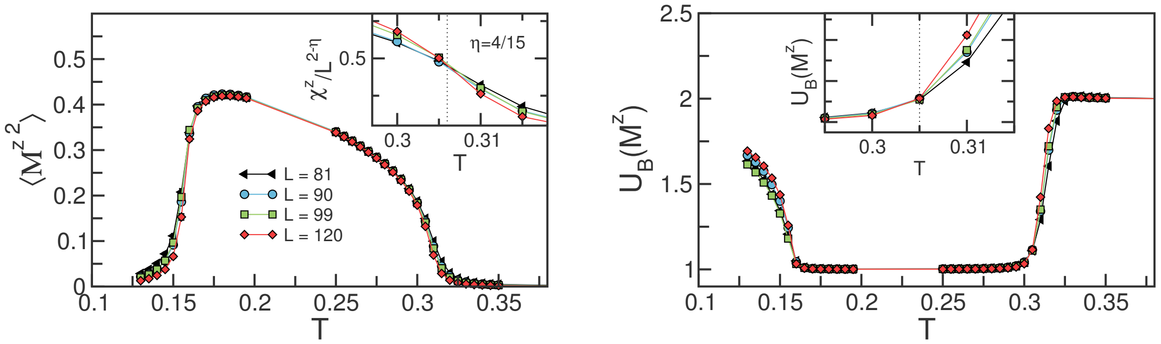

(a) Order parameter of the plateau phase. Inset shows the scaling procedure, which gives an estimate of the transition temperature $T_c = 0.306(3)$.

(b) Crossing of the Binder cumulants - the simplest way to obtain transition temperature $T_c = 0.304(2)$. Inset shows the zoom to the crossing area.

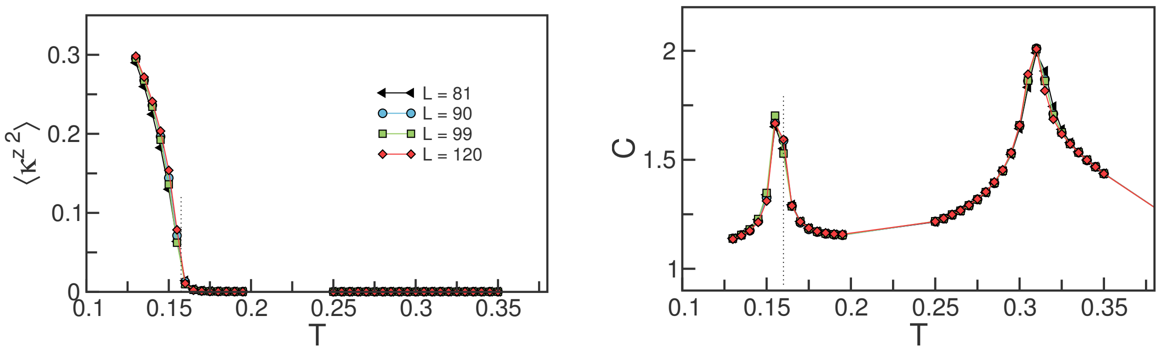

(c) Phase transition to the cone state. In the intermediate field range $2J \lesssim H \lesssim 3J$ longitudinal chirality exhibits a more rapid growth than for other H.

(d) Specific heat has two sharp maxima, which correspond to the PM–*uud*–cone phase evolution.

Figure 4.7: Finite size scaling for $H = 2J$. Top panels show the determination of PM–*uud* boundary, bottom panels illustrate the transition to the vacancy-induced cone phase. $n_{\text{imp}} = 5\%$

4) Finally, in the low-H region of the phase diagram the phase boundaries were defined by the same methods. The main difference with the previous case is that we did not rule out completely the presence of the Y phase. However, strong finite size effects did not allow to resolve the possible BKT transition (see panels (e) and (f) of Fig. 4.8) from the transition to the noncoplanar phase. This uncertainty is indicated by large error bars on the phase diagram (Fig. 4.4).

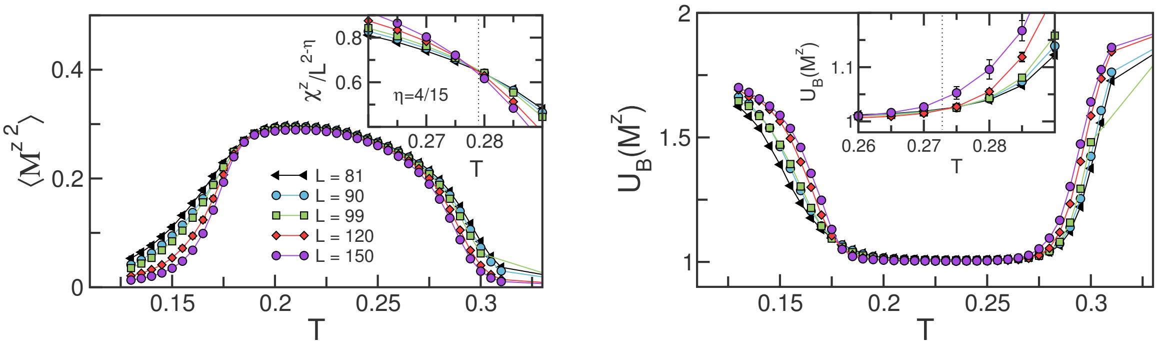

(a) The first transition to the 1/3-plateau phase is of the 2D three-state Potts universality class.

(b) Transition temperature determination using the Binder cumulants of the order parameter M^z.

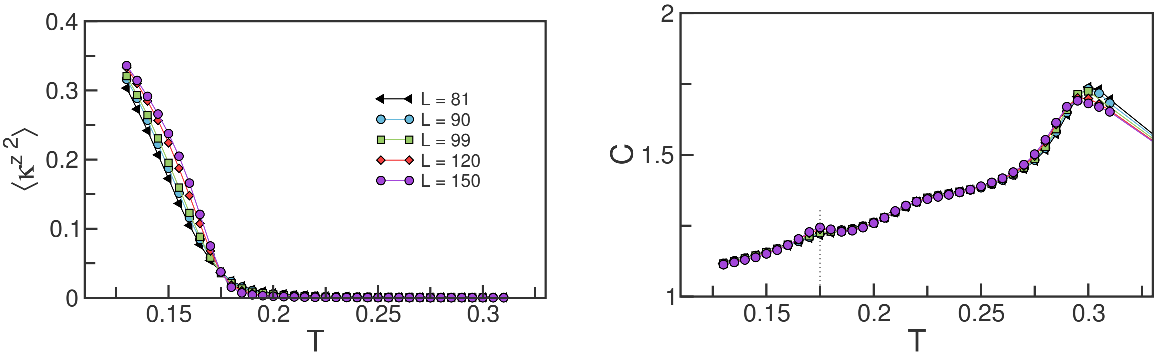

(c) Growth of κ^z indicates a transition to the cone phase at $T_c = 0.174(5)$. Inverse finite-size behaviour supports a theoretical prediction of the weak first order transition.

(d) An extremely weak anomaly in C at the lower phase transition is detected. A broad cusp around $T = 0.22$ may indicate an intermediate BKT transition to the Y phase.

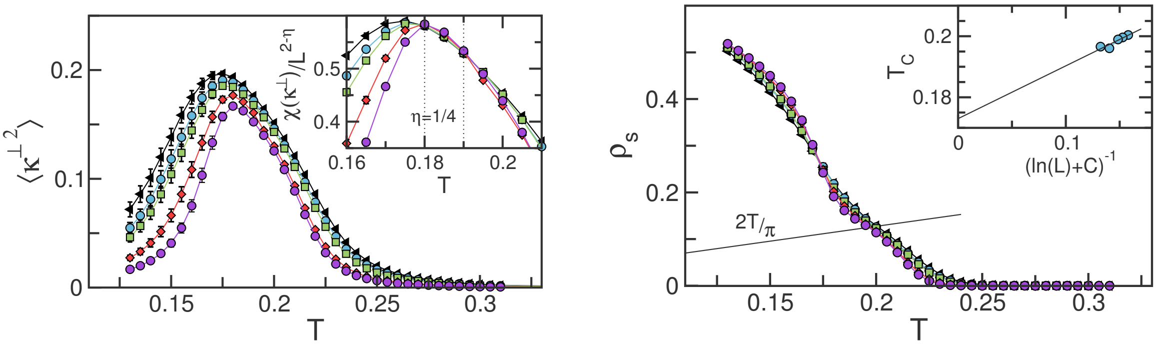

(e) Nonzero transverse chirality indicates an onset of the Y phase. Inset shows FSS scaling of the corresponding susceptibility with the BKT critical exponent $\eta = 1/4$. The available cluster sizes are not enough to unambiguously resolve a crossing of the scaling functions from their touching around $T^\star \simeq 0.185(5)$.

(f) A BKT phase transition is best traced by the scaling of the spin stiffness ρ_s. The transition, if present, occurs at $T^\star = 0.174(5)$, very close to the boundary of the cone phase. The plot may also indicate a BKT transition to the cone phase from the possible intermediate phase with the restored symmetry.

Figure 4.8: Finite size scaling of Monte Carlo results for $H = 1.3J$. Top panels show the determination of PM–*uud* boundary, middle panels illustrate the transition to the cone phase, bottom panels show the possibility of the intermediate Y phase. $n_{\mathrm{imp}} = 5\%$

4.2.6 Estimate of n_{crit} and observation perspectives

Quantum fluctuations around a mean-field state can be modelled by a negative biquadratic exchange in the Hamiltonian, as was shown in (4.6). Then beyond the classical model, quantum fluctuations will compete with the effect of dilution even at $T = 0$. For a given spin value S, there is a critical concentration of vacancies $n^c_{\mathrm{imp}} \sim 1/S$ needed to overcome the quantum selection of 'most collinear' states.

We can compare the strength of two competing effects at the plateau point $H = 3J$ in the limit of separate energy contribution from quantum fluctuation and structural defects. Consideration of the interplay of these effects greatly complicates the task because of the difficulty of calculation of the spin-wave spectra around a disorder-induced texture. We compare the total classical energy gain with the harmonic spin-wave energy in the *uud* and cone state, which is calculated as

$$\Delta E^{(s)} = \Delta E^{(s)}_Q + \Delta E^{(s)}_{\mathrm{imp}}, \qquad s = \{uud, \mathrm{cone}\}. \tag{4.13}$$

The first contribution can be determined by the harmonic spin-wave calculations. Chubukov and Golosov obtained $\Delta E^{(\mathrm{cone})}_Q - \Delta E^{(uud)}_Q = JS^2 Q$ with $Q \simeq 0.065/S$ [27]. The energy gain $\Delta E^{(\mathrm{cone})}_{\mathrm{imp}}$ is the output of our numerical minimisation technique and can be expressed as $\Delta E^{(\mathrm{cone})}_{\mathrm{imp}} = -hSn_{\mathrm{imp}} - JS^2\alpha n_{\mathrm{imp}}$ with $\alpha \simeq 0.65$. Here the second term represents the energy gain from spin reorganisation. This contribution is absent in the collinear spin structures, therefore we have $\Delta E^{(uud)}_{\mathrm{imp}} = -hSn_{\mathrm{imp}}$. Comparing these energies we find that the 1/3 magnetisation plateau of the Heisenberg TAFM is stable up to $n^c_{\mathrm{imp}} \sim 4\%$ for $S = 5/2$. This estimate of n^c_{imp} becomes even lower once quantum effects are further suppressed by weak magnetic anisotropy. Finally, the extent of the cone phase at low H suggests that critical vacancy concentration at $H < 3J$ will be lower than the one, indicated above.

4.3 Effective magnetic moment of impurities

A removed magnetic moment in an antiferromagnetic insulator induces a net magnetic moment in the system even at $H = 0$ (Note that throughout this section we will consider the magnetic field to be absent). For noncollinear magnetic structures the moment is, however, screened by a spin texture resulting from the canting of the surrounding spins [12, 16, 17]. Such a spin canting of only nearest neighbour spins is illustrated in Fig. 4.9(a). As a result, an impurity moment acquires a nonuniversal fractional value, which depends on the system details. Wollny and collaborators [16] have shown that a vacancy in the classical Heisenberg TAFM becomes slightly overcompensated, i.e. at $T = 0$ the net magnetic moment is equal to $m^{\circ}_{\mathrm{imp}} = 0.039S$ and has the *same* direction as a missing spin. At finite temperatures in the absence of long range order this purely classical moment is free to rotate in spin space leading to a Curie-like paramagnetic divergence of the magnetic susceptibility at $T \to 0$. In a system with a small but finite concentration of defects, the impurity contributions sum up to give

$$\chi(T) = \frac{N_{\mathrm{imp}} m^2_{\mathrm{imp}}}{3T} + O(1). \tag{4.14}$$

We have numerically investigated a system with a fixed concentration of vacancies, measured m_{imp} and studied how the impurity screening is modified by finite n_{imp}. First, we report results of

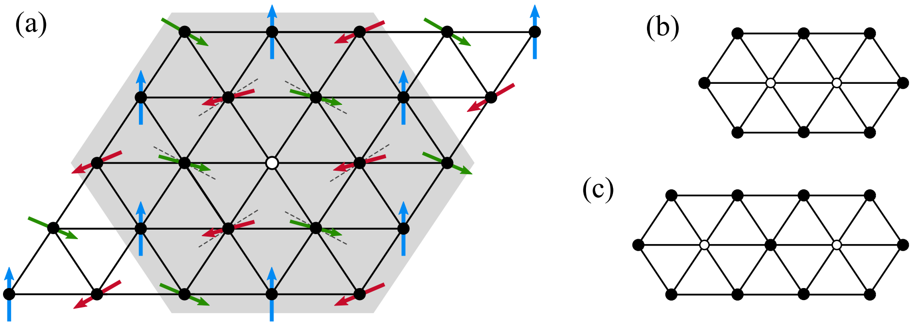

Figure 4.9: (a) An example of spin distortions around the impurity in the classical 120° ordered state. Shaded area shows all nearest neighbours up to the order 3. (b), (c) Simple clusters of impurities with the strongest distortion of screening. Effective magnetic moment of these configurations equals to $m_{\text{imp}}^{\circ\circ} = 0.11$ and $m_{\text{imp}}^{\circ\cdot\circ} = 0.08$ respectively.

zero-field Monte Carlo simulations of the classical nearest-neighbour Heisenberg antiferromagnet with a finite concentration of static vacancies. The algorithm is basically the same as the one presented in the previous section. We found that cluster size has little effect on bulk thermodynamic quantities at $T \to 0$ and, therefore, used moderate cluster size $L = 90$ in all runs for this work, except for the cases of small amount of impurities $n_{\text{imp}} < 0.01$, where larger clusters are needed for better statistics.

Figure 4.10(a) shows uniform magnetic susceptibility $\chi(T)$ normalised per spin obtained from the Monte Carlo simulations of the TAFM with and without impurities as

$$\chi = \frac{1}{3TL^2}\Big\langle\Big(\sum_i \mathbf{S}_i\Big)^2\Big\rangle. \tag{4.15}$$

The main difference between the curves is the emergent $1/T$ divergence of χ at low temperatures, which becomes stronger with increasing n_{imp}. This upturn may look counterintuitive as no extra magnetic moments are brought into the system. Note that our Monte Carlo results for $\chi(T)$ closely resemble the susceptibility data measured for nominally pure TAFM materials, for example, for LuMnO$_3$ [64].

We associate an average magnetic moment m_{imp} with every impurity and interpolate the susceptibility curves at $T \to 0$ with eq. (4.14) to determine its value. In addition, we obtain independent results for the impurity moments m_{imp} by another method: direct calculation of

$$m_{\text{imp}}^2 = \frac{1}{N_{\text{imp}}}\Big(\sum_i \mathbf{S}_i\Big)^2 \tag{4.16}$$

in the classical ground state at zero temperature from our energy minimisation algorithm. m_{imp}, obtained by both methods was averaged over at least 200 random impurity configurations.

Figure 4.10 (b) presents the main result of this section: a nontrivial growth of the single impurity moment with concentration. Values, obtained by the two methods (displayed by full and open circles respectively) match perfectly and in the following we do not make the difference between the two methods. The growth is observed even at small $n_{\text{imp}} \sim 1\%$, which is somewhat surprising as at such weak dilution one may expect a nearly independent impurity behaviour with $m_{\text{imp}} = m_{\text{imp}}^{\circ}$. Indeed, Fig. 4.10 (b) shows that m_{imp} is significantly renormalised from the

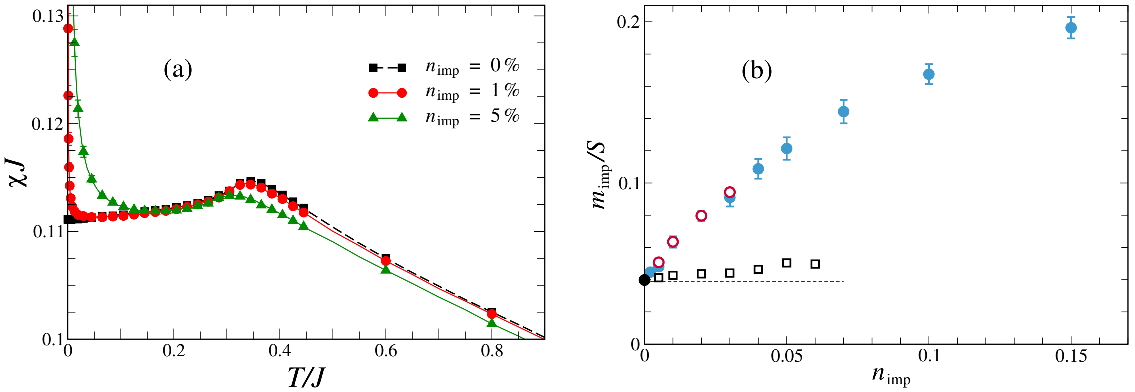

(a) Magnetic susceptibility for different concentrations of vacancies, from our Monte Carlo simulations of the Heisenberg TAFM at $H = 0$. The Curie-like singularity at $T \to 0$ gives the value of effective impurity moment m_{imp} from eq. (4.14).

(b) Growth of the effective impurity moment with vacancy concentration obtained using susceptibility interpolation (full circles) and direct measurement at the ground state (open circles). Open squares correspond to m_{imp} in the restricted impurity configurations. Dashed line and a big marker at $n_{\text{imp}} = 0$ show m°_{imp} from the work [16].

Figure 4.10: Impurity moment m_{imp} manifests itself as a Curie-like divergence of χ at $T \to 0$ (a). In noncollinear magnets it exhibits nontrivial growth from the single vacancy value.

single impurity value, even at the lowest considered $n_{\text{imp}} = 0.2\%$, which is comparable to the case of a single impurity on a cluster with $L = 12$, studied in the work of Wollny *et al.* [16].

One possible explanation of growing m_{imp} is an assumption that screening clouds from different impurity sites interact, and self-average. According to Ref. [11, 16] readjustment angles of spins, surrounding an impurity decay as $\delta\Theta(r) \sim 1/r^3$ at long distances. For a finite concentration of impurities one may expect cut off of individual screening clouds at average distances $R \sim n_{\text{imp}}^{-1/2}$. It leads to the modification of screening, consistent with the square root dependence on vacancy fraction:

$$\delta m \sim \int_R^{\infty} \Theta(r)|\mathbf{l}(r)|d^2r \sim n_{\text{imp}}^{1/2}. \tag{4.17}$$

Here $\mathbf{l}(r)$ - is a vector, pointing in the direction spin distortion, and results only in a prefactor, which is omitted. However, the measured m_{imp} (Fig. 4.10 (b)) clearly does not fit to this procedure, and therefore demands for a different explanation of the observed dependence.

We ascribe the growth of impurity moment to the effects that are quadratic in n_{imp}. Indeed, an individual impurity moment is strongly screened to a very small value m°_{imp}. Hence, one is forced to consider statistically rare cases of two impurities occupying nearby sites, see figs. 4.9 (b) and (c). If such impurity configurations have moments, which are not very well screened and significantly larger than m°_{imp}, their impact on the net magnetic moment and the low-temperature susceptibility may be quite significant.

We measured m_{imp} for a few simple vacancy configurations and show in figs. 4.9(b) and (c) two impurity clusters with the largest values of the effective magnetic moment. The calculations yield $m^{\circ\circ}_{\text{imp}} = 0.11$ and $m^{\circ\cdot\circ}_{\text{imp}} = 0.08$ respectively, the result that is several times larger than m°_{imp}. Along with the large coordination number of the triangular lattice, it overcomes the small statistical weight $P \sim n^2_{\text{imp}}$ of these configurations.

In addition, we have performed similar numerical simulations restricting vacancies from being placed within the first three neighbours from each other. The respective exclusion region is shown by the shaded area in Fig. 4.9(a). In the first place, such a computation serves to verify the above hypothesis; second, it may also model weak correlations in the structural disorder, which develop in real solids due to elastic tension etc. The results are plotted in Fig. 4.10(b) with open square markers. They demonstrate only a slight growth of m_{imp} from m°_{imp}. Therefore, at distances exceeding 2–3 lattice spacings, impurities only barely interact and behave completely individually. These results strongly support the above explanation of the growth of impurity moment due to clustering of vacancies.

4.4 Order by structural disorder in the easy-plane TAFM

Most of the known triangular antiferromagnets, including the ones that belong to the recently synthesised family $\mathrm{Ba_3TT'_2O_9}$, with transition metals $\mathrm{T} = \mathrm{Co}, \mathrm{Ni}, \mathrm{Mn}$ and $\mathrm{T'} = \mathrm{Sb}, \mathrm{Nb}$, [55, 65, 66] are not purely Heisenberg, but have a certain exchange anisotropy. The easy-plane TAFM exhibit similar accidental degeneracy of ground states, as the Heisenberg system, therefore, it is interesting to study the order by structural disorder in these models.

In this section we consider the extreme case of the XY TAFM, or the planar rotator model

$$\hat{\mathcal{H}} = J \sum_{\langle ij \rangle} \mathbf{S}_i \cdot \mathbf{S}_i - \mathbf{H} \cdot \sum_i \mathbf{S}_i \tag{4.18}$$

with two dimensional spins $\mathbf{S}_i$ and the magnetic field, directed parallel to the spin plane. Its ordered states were investigated by Lee *et al.* [49, 52]. After the application of the minimum of energy condition (4.3) one degree of freedom is left unspecified. So much like in the Heisenberg system, the planar ground states of the model are subject to the accidental degeneracy.

To study state selection in the XY model the same analysis, as in the section 4.2 can be carried out. The only difference with the isotropic case is the absence of terms, containing the out-of-plane component S^y_i in eq. (2.3) and everywhere below. But the derivation of all biquadratic exchanges from thermal and quantum fluctuations remains intact. Therefore, thermal fluctuations lift the ground-state degeneracy in favour of the same sequence of phases in magnetic field as for the Heisenberg model, see Fig. 4.1(a)–(c). The same applies to the competing term from structural disorder: vacancies and weak bond disorder can be described by an effective positive biquadratic correction. In the case when the conical state, Fig. 4.1(f), as well as other noncoplanar configurations are forbidden, it lifts the degeneracy between the coplanar structures only. More specifically, it stabilises the anti-Y (d) and the fan (e) states, which are different realisations of the same ordered phase at different magnetic fields.

We have complemented analytical consideration with a numerical search for the lowest-energy magnetic structures using the same technique as for the isotropic model. First, we constructed a proper order parameter that distinguishes different planar spin configurations. In particular, it should be able to tell the anti-Y phase, Fig. 4.1 (d) or fan phase (e) from Y, *uud* and V states. The principal order parameter of any ordered structure in the XY TAFM is again the usual staggered magnetisation with the ordering vector $\mathbf{Q} = (4\pi/3, 0)$

$$\mathbf{M}_Q = \frac{1}{N}\sum_i \mathbf{S}_i e^{-i\mathbf{Q}\mathbf{r}_i}. \tag{4.19}$$

It is a complex vector with two components $M_Q^{\|}$ and $M_Q^{\perp}$, defined relative to the direction of the magnetic field. The symmetry analysis of the study [49] shows that up to the 120° rotation in the the complex plane (in other words, up to permutations of the three sublattices) $\mathrm{Im}(M_Q) = 0$ in *uud* and V phases. On the other hand, in the fan phase $\mathrm{Im}(M_Q^{\perp})$ is nonzero. Therefore, a natural order parameter is

$$m_3^{\perp\prime\prime} = \frac{8}{N}\left|\mathrm{Im}(M_Q^{\perp 3})\right|. \tag{4.20}$$

The normalisation prefactor is chosen such that $m_3^{\perp\prime\prime} = 1$ in the perfect 120° structure. On the other hand the symmetry of Y and anti-Y phases is the same, so they differ only by the values of the order parameters. In the anti-Y configuration $m_3^{\perp\prime\prime}$ decreases with decreasing magnetic field, while in the Y state it stays smaller and grows. At the same time another component

$$m_3^{\|\prime} = \frac{8}{N}\mathrm{Re}(M_Q^{\| 3}) \tag{4.21}$$

is strictly positive in the anti-Y state, while it is negative in its counterpart.

Numerical results are fully consistent with the presence of the fan (anti-Y) state in the whole range of magnetic fields. We present the results of simulations of the model with $n_{\mathrm{imp}} = 5\%$ of vacancies in figure 4.11, which shows a clear anti-Y–fan–PM evolution of phases. The finite size analysis, shown on the inset, states that the selection of the least collinear configurations is robust, and no signs of glassy behaviour are observed. Finally, we note that a considerably larger amount of initial configurations were required to obtain a true ground state in comparison with the Heisenberg model. This explains relatively small cluster sizes, used in this study.

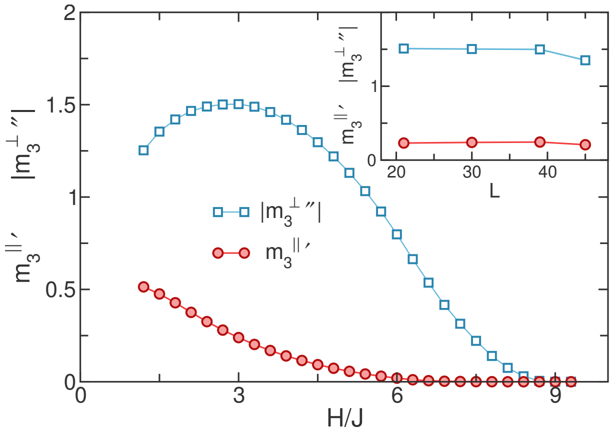

Figure 4.11: Two of four components of the cube of the order parameter $\mathbf{M}_Q^3$ at zero temperature. Calculations are performed for $L = 30$ and $n_{\mathrm{imp}} = 5\%$. Inset shows the absence of considerable finite size effects at the plateau point $H/J = 3$. Every measurement is averaged over 200 impurity replicas. $10^3 - 10^4$ initial conditions is required to systematically find the global energy minimum.

The results of this section can be directly applied to the case of moderate easy-plane anisotropy, which corresponds to the XXZ triangular antiferromagnet, an intermediate case between the Heisenberg and the planar rotator model. Stabilisation of the same least collinear fan state is expected when the magnetic field lies in the easy plane.

4.5 Summary

Nonmagnetic impurities modify the behaviour of the classical TAFM in an external magnetic field. The effect of static disorder can be qualitatively described by a positive biquadratic exchange, which competes with a similar effective interaction of the opposite sign generated by thermal and quantum fluctuations. Vacancies tend to stabilise the conical state for the Heisenberg TAFM, whereas for the XY model with an in-plane field they favour the fan spin structure. Systematic experimental studies of frustrated magnets doped with nonmagnetic impurities may, therefore, bring new fascinating physics. Apart from the fundamental interest, this can open additional possibilities in controlling electrical and magnetic polarisations in triangular multiferroics. From the theoretical perspective it would be interesting to perform thorough numerical studies of the triangular system with bond disorder or other types of defects that appear in magnetic solids. These results may shed more light on the mechanism, which stands behind the observed competition of impurities and fluctuations,

Secondly, we demonstrate that an effective fractional impurity moment revealed in the paramagnetic Curie tail of the magnetic susceptibility exhibits a substantial growth with the impurity concentration. We attribute this growth to an anomalously small value of $m_{\rm imp}$ of an isolated vacancy in the TAFM, and, as a consequence, to significance of correlated impurity effects $\sim n_{\rm imp}^2$. This effect should be experimentally detectable as Curie tails in $\chi(T)$ are often observed in magnets. Magnetic moment of a single impurity can be extracted from the study of these tails in samples with a known defect concentration. It might be also interesting to study other noncollinear helical antiferromagnets. While we expect the effect to persist, it may be quantitatively very different, for example, due to the not so small values of vacancy moments.

Chapter 5

Order by structural disorder in the XY pyrochlore antiferromagnet

The order by disorder is an elegant concept, which explains the realisation of a specific state from an otherwise degenerate ground state manifold of some frustrated systems. However, it is sometimes criticised for the fact that it lacks undoubtful experimental observation. $\mathrm{Er_2Ti_2O_7}$ is the least contested experimental realisation of the fluctuation-induced ordering, that is why it plays a central role in discussions about order by disorder.

It is natural then to ask a question, whether a mechanism of order by *structural* disorder can be extended to this compound? In addition, the properties of its ground states make $\mathrm{Er_2Ti_2O_7}$ an even more interesting case to study order by structural disorder effect. Firstly due to the fact that the *least* collinear $m_{x^2-y^2}$ state is favoured by thermal and quantum fluctuations in the pure system and secondly because biquadratic exchange, associated with ground state selection does not lift the degeneracy of the ground state manifold in XY anisotropic pyrochlore antiferromagnets.

In this chapter we present a study of the frustrated anisotropic easy-plane antiferromagnet on the pyrochlore lattice, which is relevant for $\mathrm{Er_2Ti_2O_7}$. We show that despite the aforementioned distinctions between triangular and pyrochlore antiferromagnets, our main conclusion is valid for both systems. Structural disorder breaks the continuous ground state degeneracy and selects the states that are the least favoured by the conventional order by disorder effect.

The organisation of the chapter is the following: first, we present a minimal model that describes the low-T properties of $\mathrm{Er_2Ti_2O_7}$. Then in section 5.2, following the path of the real space perturbation expansion, we derive the effective anisotropic corrections, originating from thermal and quantum fluctuations, responsible for selecting the ground state in the pure model. The next section 5.3 is devoted to the analytic treatment of pyrochlore with structural disorder and to the order by structural disorder mechanism. In section 5.4 we present our numerical results for the classical pyrochlore system. They support our scenario of competition of thermal and structural disorder in selecting the ground state of the system. Finally, in section 5.5 we discuss the possibility of experimental observation of the new impurity-induced phase in $\mathrm{Er_2Ti_2O_7}$ and the future perspectives of our findings.

5.1 Introduction and model for $\mathrm{Er_2Ti_2O_7}$

$\mathrm{Er_2Ti_2O_7}$ - is a paradigmatic example of lifting the ground state degeneracy by the order by disorder effect. In this section we present the model that suits for studying the low-T properties of the compound. In $\mathrm{Er_2Ti_2O_7}$ magnetic Er^{3+} ions reside in vertices of a pyrochlore lattice - a lattice, formed by the regular corner sharing tetrahedra. Er^{3+} ions form a $4I_{15/2}$ configuration with the total angular momentum $J = 15/2$. According to the crystal field analysis [67, 68] this multiplet is split by a strong local crystalline field with D_{3d} symmetry, producing the ground state Kramers doublet. This is a reasonable approximation as long as the energy scales of the Hamiltonian: exchange parameters $J \lesssim 0.4$ meV and the external magnetic field $H \lesssim 2$T are much smaller than the gap to higher crystal field levels $\Delta \sim 6.5$ meV [67]. The magnetic moment of this doublet is found to lie mainly in the local xy plane, so the problem can be mapped onto a $S = 1/2$ XXZ-pseudospin model. At $T_N \simeq 1.2K$ it undergoes a second order phase transition in the 3D XY-universality class [69, 70] to an ordered state. According to group theory, this state belongs do a continuously degenerate one-dimensional manifold of states. Neutron diffraction experiments show that a specific noncoplanar $m_{3z^2-r^2}$ configuration with 6 domains is realised from the manifold [67]. A combination of thermal and quantum order by disorder is the most probable explanation of this selection [6, 7, 71, 72] because $\mathrm{Er_2Ti_2O_7}$ ground state degeneracy is symmetry protected from small perturbations. Finally, recent experiments by Ross *et al.* [73] confirm the presence of a spin wave gap, corresponding to quantum fluctuations. Therefore, there is a good general agreement that it is, indeed, the order by disorder effect that is responsible for selection. We note, however, that there is an alternative point of view on the ground state selection in $\mathrm{Er_2Ti_2O_7}$, based on the effect of higher crystal field levels [74, 75].

In a pyrochlore material the unit cell contains four magnetic sites. Their positions in units of the cubic lattice parameter a are given by

$$\mathbf{r}_1 = (0,0,0)\,, \quad \mathbf{r}_2 = (\tfrac{1}{4},\tfrac{1}{4},0)\,, \quad \mathbf{r}_3 = (0,\tfrac{1}{4},\tfrac{1}{4})\,, \quad \mathbf{r}_4 = (\tfrac{1}{4},0,\tfrac{1}{4})\,. \tag{5.1}$$

When a pyrochlore system has a distinct Ising or planar anisotropy it is convenient to consider it in a local basis with $\hat{\mathbf{z}}_i$ oriented along the symmetry axis on each site (Fig. 5.1).

$$\hat{\mathbf{z}}_1 = \tfrac{1}{\sqrt{3}}(1,1,1)\,, \quad \hat{\mathbf{z}}_2 = \tfrac{1}{\sqrt{3}}(-1,-1,1)\,, \quad \hat{\mathbf{z}}_3 = \tfrac{1}{\sqrt{3}}(1,-1,-1)\,, \quad \hat{\mathbf{z}}_4 = \tfrac{1}{\sqrt{3}}(-1,1,-1)\,. \tag{5.2}$$

The most general form of the bilinear pseudospin 1/2 Hamiltonian that is compatible with the symmetry of the lattice can be written as [6, 76]

$$\hat{\mathcal{H}} = \sum_{\langle ij \rangle} J_{zz} S_i^z S_j^z + J_\perp \mathbf{S}_i^\perp \cdot \mathbf{S}_j^\perp + J_\perp^a (\mathbf{S}_i^\perp \cdot \hat{\mathbf{r}}_{ij})(\mathbf{S}_j^\perp \cdot \hat{\mathbf{r}}_{ij}) + J_{z\perp}\big[S_j^z(\mathbf{S}_i^\perp \cdot \hat{\mathbf{r}}_{ij}) + S_i^z(\mathbf{S}_j^\perp \cdot \hat{\mathbf{r}}_{ji})\big]. \tag{5.3}$$

Here $\hat{\mathbf{r}}_{ij} = (\mathbf{r}_i - \mathbf{r}_j)/|\mathbf{r}_i - \mathbf{r}_j|$ is a unit vector in the bond direction. Spin operators $\mathbf{S}_i$ are taken in the local coordinate frame with S_i^z and $\mathbf{S}^\perp$ being projections on the local trigonal axis and on the orthogonal xy plane, respectively. J_{zz} and $J_\perp$ are coupling constants of Ising and XY-type coupling constants. The third term represents the bond-dependent dipole like anisotropy, in principle both signs of $J_\perp^a$ are allowed by symmetry. And the last term is the Dzyaloshinskii-Moriya type interaction, which can also be present in pyrochlores due to the absence of inversion symmetry.

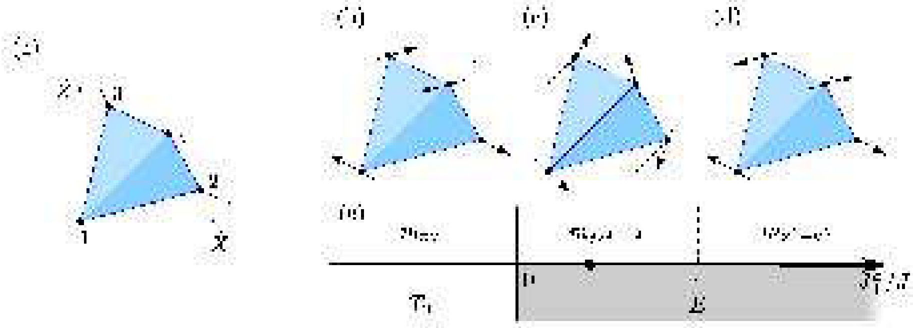

Figure 5.1: (a) Four sites of magnetic tetrahedra lattice together with their local trigonal axes $\hat{z}_i$ (5.2) in a global coordinate frame $(\hat{X}, \hat{Y}, \hat{Z})$. (b) - (d) Ordered magnetic structures of the XY pyrochlore antiferromagnet: (b) the coplanar Palmer-Chalker state m_{T_2}, (c) the noncoplanar state $m_{3z^2-r^2}$, and (d) the coplanar state $m_{x^2-y^2}$. (e) Schematic phase diagram of the model (5.7) showing the lowest-energy magnetic structures and the corresponding irreducible representations of T_d depending on the ratio $J^a_\parallel/J_\perp$. The circle marks the value of $J^a_\parallel/J_\perp$ in $Er_2Ti_2O_7$.

This form (5.3) of the Hamiltonian is independent of the choice of the $\hat{x}$ and $\hat{y}$ axis and is convenient for the calculation of classical energies and for Monte Carlo simulations. It is not the only one though. Below for the sake of completeness of introduction we present another form, which is also frequently used in the literature [7, 77, 78]

$$\begin{aligned}\hat{\mathcal{H}} = \sum_{\langle ij\rangle}\Big\{ & J_{zz}S_i^zS_j^z - J_\pm(S_i^+S_j^- + S_i^-S_j^+) + J_{\pm\pm}(\gamma_{ij}S_i^+S_j^+ + \gamma_{ij}^*S_i^-S_j^-) \\ & + J_{z\pm}\left[S_i^z(\zeta_{ij}S_j^+ + \zeta_{ij}^*S_j^-) + i\leftrightarrow j\right]\Big\}. \end{aligned} \quad (5.4)$$

The exchange constants are simply related to the ones used in equation (5.3):

$$J_\perp = 2J_\pm + 2J_{\pm\pm}, \qquad J^a_\parallel = 8J_\pm - 4J_{\pm\pm}, \qquad J_{z\perp} = -2\sqrt{3}J_{z\pm}. \quad (5.5)$$

From the fit of the $Er_2Ti_2O_7$ excitation spectrum from inelastic neutron-scattering in strong magnetic field experiments by Savary *et al.* [7] one obtains the estimates for the exchange constants of the Hamiltonian (5.4) in meV

$$J_\perp = 0.21(2), \quad J^a_\parallel = 0.35(5), \quad J_z = -0.025(2), \quad J_{z\perp} = 0.03(5). \quad (5.6)$$

The above values confirm the planar character of the interaction between Er^{3+} moments as well as a significant anisotropy for the in-plane exchange constants $J^a_\parallel/J_\perp \approx 1.7$. Since longitudinal exchange constants J_z and $J_{z\perp}$ are an order of magnitude smaller, the physical properties $Er_2Ti_2O_7$ can be quite accurately captured by the model with just two exchange parameters $J_\perp$ and $J^a_\parallel$. Such a model was used in the core of another estimate of exchanges that was done in Ref [6], based on the zero-field magnon dispersion data of Ruff *et al.* [79]. It yielded $J_\perp = 0.25$ meV and $J^a_\parallel = 0.3$ meV. There is a fairly good correspondence between the sets of exchanges, which suggests that a minimal model, in which the anisotropic spin interaction is restricted to the easy-plane spin components with $J_\perp$ and $J^a_\parallel$ interactions is

$$\hat{\mathcal{H}} = \sum_{\langle ij\rangle} J_\perp \mathbf{S}_i^\perp\cdot\mathbf{S}_j^\perp + J^a_\parallel(\mathbf{S}_i\cdot\hat{\mathbf{r}}_{ij})(\mathbf{S}_j\cdot\hat{\mathbf{r}}_{ij}). \quad (5.7)$$

with a point $J^a_\perp/J_\perp \simeq 1.5(2)$ corresponding to $Er_2Ti_2O_7$.

We begin with the description of the classical ground states of the spin model (5.7). Throughout all the work we will be interested in the antiferromagnetic sign of the main XY interaction $J_\perp > 0$. Then, depending on the sign of $J^a_\perp$, magnetically ordered states belong to one of the two different classes, which transform according to the E or T_2 irreducible representations of the tetrahedral point group. They are also labelled in the literature as (Γ_5) and (Γ_7) representations respectively. Figure 5.1(e) shows a mean-field ground state phase diagram of the model (5.7). For negative $J^a_\perp$ the anisotropic exchange has the same effect as the long-range dipolar interactions. It selects the Palmer-Chalker states, [80] represented by the m_{xy} state in Fig. 5.1(b). Their classical energy is $E_{T_2} = -S^2(J_\perp - \frac{1}{2}J^a_\perp)$. For $J^a_\perp > 0$ the ground state belongs to a two component E representation with the energy $E_E = -S^2(J_\perp + \frac{1}{2}J^a_\perp)$. Its basis is formed by the noncoplanar state $m_{3z^2-r^2}$ (ψ_2) and the coplanar $m_{x^2-y^2}$ (ψ_3) state. These are shown in figs. 5.1(c) and 5.1(d), respectively. Value $J^a_\perp = 0$ yields a highly degenerate point with many magnetic structures described by different ordering wave vectors having the same classical energy [81]. Before proceeding further we note that a small (compared to both $J_\perp$ and $J^a_\perp$) nonzero value of the two other couplings J_{zz} and $J_{z\perp}$ does not distort the phase diagram of Fig. 5.1, leaving the ground states within E and T_2 representations.

From now on we focus on $J^a_\perp > 0$, and choose the direction of local $\hat{\mathbf{x}}_i$ and $\hat{\mathbf{y}}_i$ axes such that they coincide with the direction for the $m_{3z^2-r^2}$ and the $m_{x^2-y^2}$ state on each site:

$$\begin{aligned}
&\hat{\mathbf{x}}_1 = \tfrac{1}{\sqrt{6}}(1,1,-2)\,, \quad \hat{\mathbf{x}}_2 = \tfrac{1}{\sqrt{6}}(-1,-1,-2)\,, \quad \hat{\mathbf{x}}_3 = \tfrac{1}{\sqrt{6}}(1,-1,2)\,, \quad \hat{\mathbf{x}}_4 = \tfrac{1}{\sqrt{6}}(-1,1,2)\,,\\
&\hat{\mathbf{y}}_1 = \tfrac{1}{\sqrt{2}}(-1,1,0)\,, \quad \hat{\mathbf{y}}_2 = \tfrac{1}{\sqrt{2}}(1,-1,0)\,, \quad \hat{\mathbf{y}}_3 = \tfrac{1}{\sqrt{2}}(-1,-1,0)\,, \quad \hat{\mathbf{y}}_4 = \tfrac{1}{\sqrt{2}}(1,1,0)\,.
\end{aligned} \tag{5.8}$$

Then the whole degenerate manifold of ground states can be parameterised with one angle φ as

$$\mathbf{S}_i = S\,(\hat{\mathbf{x}}_i \cos\varphi + \hat{\mathbf{y}}_i \sin\varphi)\,. \tag{5.9}$$

Angle values $\varphi = \pi k/3$ and $\varphi = \pi(k+\frac{1}{2})/3$ correspond to different $m_{3z^2-r^2}$ and $m_{x^2-y^2}$ states, respectively. A possibility to parameterise the lowest energy states with one variable follows also from the simple degree of freedom counting argument. Consider a simple building block of the lattice - one tetrahedron with four classical vector spins. Function (5.7) is minimal when all spins lie in their easy planes and when the net magnetisation of the plaquette is zero. Therefore, we have four degrees of freedom, constrained by three equations.

According to the group theory $m_{3z^2-r^2}$ and $m_{x^2-y^2}$ states remain strictly degenerate for a general case of the bilinear spin Hamiltonian involving further anisotropic terms or couplings to distant neighbours. An effective biquadratic exchange $(\mathbf{S}_i \cdot \mathbf{S}_j)^2$, does not lift this degeneracy either. The degeneracy may be lifted only by interactions of the sixth order in spin components, which are usually extremely small in real materials. Hence, the spin model (5.7) provides an interesting example of the order from disorder selection. For $0 < J^a_\perp/J_\perp < 4$, thermal and quantum fluctuations favour the noncoplanar ground states of the type $m_{3z^2-r^2}$, including the point $J^a_\perp/J_\perp \sim 1.5$ corresponding to $Er_2Ti_2O_7$ [6, 7, 70]. For $J^a_\perp/J_\perp > 4$, the selection takes a different route and fluctuations stabilise the $m_{x^2-y^2}$ states [82]. The corresponding transition at $J^a_\perp = 4J_\perp$ is indicated by a dashed line in Fig. 5.1(e). In the next section we show that quantum and thermal corrections to the classical energy generate $E_{\text{eff}} \sim -(J^a_\perp - 4J_\perp)\cos 6\varphi$ explaining the above transition.

5.2 Order by disorder

In the previous chapter we have shown that for the Heisenberg triangular antiferromagnet the leading correction beyond the mean-field approximation can be represented by an additional biquadratic exchange term in the Hamiltonian. It leads to the lifting of the mean-field degeneracy of the ground state of the system in the external field. The same argumentation applies to a number of other frustrated systems: the most collinear spin structures are selected by thermal and quantum fluctuations of spins [19, 22]. This effect is known as order from disorder.

In $Er_2Ti_2O_7$ biquadratic exchange does not break the ground state symmetry and thus cannot realise order by disorder. Indeed, substitution of (5.9) into $K(\mathbf{S}_i\cdot\mathbf{S}_j)^2$ produces a fourth harmonic of φ. But it cannot enter in the Hamiltonian as the [111] direction is not a fourfold rotation axis of the pyrochlore lattice.

In this section we will apply the formalism of the real space perturbation expansion to the easy-plane pyrochlore system and show that fluctuations break the symmetry via the sixth harmonic of φ. For this, one needs to go to the higher order in perturbation expansion - direct calculation of the second order terms results in a constant, independent of φ. Therefore, the derivation of these terms will be omitted. One of the disadvantages of the real space perturbation expansion is that the number of terms grows rapidly with the order of the theory. Third order quantum correction involves calculation of two contributions, which partly compensate each other. It causes come additional complications for the $S = 1/2$ case, which is relevant for $Er_2Ti_2O_7$. In subsection 5.2.4 we develop the modified RSPT, which helps to circumvent the problem of the exact cancellation of two terms and show that the overall tendency of degeneracy breaking holds also for $S = 1/2$ spins.

Our findings of this section correspond to the results of classical [72, 82] and quantum [6, 7] harmonic spin wave calculations. Qualitatively, we show that order by disorder favours six $m_{3z^2-r^2}$ states.

5.2.1 General formalism

To proceed with calculations for the anisotropic XY pyrochlore (5.7) we shall use an alternative form of the spin Hamiltonian

$$\hat{\mathcal{H}} = \frac{1}{12}\sum_{\langle ij\rangle} -(2J_\perp + J^a_\perp)\,(S^+_i S^-_j + S^-_i S^+_j) + (4J_\perp - J^a_\perp)\,(\mathrm{e}^{i\gamma_{ij}} S^+_i S^+_j + \mathrm{e}^{-i\gamma_{ij}} S^-_i S^-_j). \quad (5.10)$$

where the phases γ_{ij} depend on the choice of basis in the xy planes. This form of the spin Hamiltonian is similar to eq. (5.4) with a minor redefinition of complex factors, we explicitly extract phases, which greatly simplifies our subsequent expressions. For the above choice of axes (5.8) we have

$$\gamma_{12} = \gamma_{34} = 0\,, \qquad \gamma_{13} = \gamma_{24} = \frac{2\pi}{3}\,, \qquad \gamma_{14} = \gamma_{23} = -\frac{2\pi}{3}\,. \quad (5.11)$$

The real-space perturbation expansion starts with (i) rewriting the Hamiltonian in the local frame around an arbitrary ground-state spin configuration and (ii) separating all terms that depend on the deviation of only one spin. This on-site part is subsequently regarded as a noninteracting Hamiltonian $\hat{\mathcal{H}}_0$ with trivially calculated excited states. All other terms describe interactions of spin fluctuations on adjacent sites and are treated as a perturbation $\hat{V}$. Standard thermodynamic or quantum perturbation theories are used to calculate the effect of $\hat{V}$. The obtained correction terms generate effective spin-spin interactions beyond the original spin Hamiltonian and produce the order by disorder effect.

Following the course of derivation of the section 2.1, we start with a ground state, parameterised by a value of φ (5.9) in the coordinate frame, defined by equations (5.2) and (5.8). First, we transform to the local basis, such that the new $\hat{\mathbf{z}}$ axis becomes parallel to the spin direction (5.9). As the Hamiltonian contains only planar spin components, it is convenient to choose the new local $\hat{\mathbf{x}}$ axis to lie in the respective easy plane. We underline that a new frame does not cause a complication, related to the bond-dependence of the local coordinate frame, which exists for the TAFM model. Such a transform is in fact a rotation in a renamed easy $\hat{\mathbf{z}} - \hat{\mathbf{x}}$ plane, so the ladder components $S_i^{\pm}$ acquire a phase $S^{\pm} = \mathrm{e}^{\pm i\varphi}(S^z \pm iS^x)$. Then, in the new coordinate system the spin Hamiltonian takes the form

$$\hat{\mathcal{H}} = \sum_{\langle ij \rangle} \big[h_{ij} S_i^z S_j^z - M_{ij} S_i^x S_j^x - K_{ij}(S_i^x S_j^z + S_i^z S_j^x)\big], \tag{5.12}$$

where h_{ij}, M_{ij}, and K_{ij} are bond-dependent constants

$$\begin{aligned} h_{ij} &= -\frac{1}{6}(2J_\perp + J_\perp^a) + \frac{1}{6}(4J_\perp - J_\perp^a)\cos(2\varphi + \gamma_{ij}), \\ K_{ij} &= \frac{1}{6}(4J_\perp - J_\perp^a)\sin(2\varphi + \gamma_{ij}), \\ M_{ij} &= \frac{1}{6}(2J_\perp + J_\perp^a) + \frac{1}{6}(4J_\perp - J_\perp^a)\cos(2\varphi + \gamma_{ij}). \end{aligned} \tag{5.13}$$

They explicitly depend on the angle φ, which parameterises the classical ground states and on the type of the bond via the parameters γ_{ij} (5.11). Finally, we extract the on-site part and rewrite (5.12) as $\hat{\mathcal{H}} = \hat{\mathcal{H}}_0 + \hat{V}_2 + \hat{V}_3 + \hat{V}_4$, where

$$\begin{aligned} \hat{\mathcal{H}}_0 &= h\sum_i (S - S_i^z), & h &= (2J_\perp + J_\perp^a)S, \\ \hat{V}_2 &= -\sum_{\langle ij \rangle} M_{ij} S_i^x S_j^x, & \hat{V}_3 &= -\sum_{\langle ij \rangle} K_{ij}(S_i^x S_j^z + S_i^z S_j^x), \\ \hat{V}_4 &= \sum_{\langle ij \rangle} h_{ij}(S - S_i^z)(S - S_j^z). \end{aligned} \tag{5.14}$$

The constant $h = \sum_j h_{ij} S$ is an amplitude of a local magnetic field, which is the same on every site for any ground state. In the above expression, we also omitted a constant term corresponding to the classical energy. In the two following subsections we calculate the relevant energy corrections generated by thermal and quantum fluctuations.

5.2.2 Thermal order by disorder

First, we consider a model of purely classical spins of the length $|\mathbf{S}_i| = S$. At low temperatures, spins fluctuate about their equilibrium directions by small S^x and S^y corresponding to deviations within the local easy plane and out of it, respectively. As before the local fluctuations are governed by $\hat{\mathcal{H}}_0 = \frac{h}{2S}\sum(S_i^{x2} + S_i^{y2})$.

The consecutive calculation of corrections, from a cluster expansion of the section 2.1.2, yields that all processes, which involve clusters with only two links, for example, $\Delta F^{(2)}$ (2.14), do not depend on the parameter φ. It is the illustration of the fact that $\hat{\mathbf{y}}_\mathbf{i}$ are the directions of the sixfold rotation axis. In what follows, we omit all constant corrections, which is indicated by the sign $\simeq$. The sixth harmonic of φ appears in the triangular process (Fig. 2.2):

$$\Delta F^{(3)} = \frac{\langle \hat{V}_2^3 \rangle}{6T^2} = -\frac{TS^3}{h^3} \sum_{\triangle} M_{ij} M_{jk} M_{ki}. \tag{5.15}$$

Summation in (5.15) is performed over all triangular plaquettes of a pyrochlore lattice and $i, j, k \in \triangle$. Substituting M_{ij} and h from (5.13) and (5.14) we obtain

$$\Delta F^{(3)} \simeq -\frac{TN}{432} \cdot \frac{(4J_\perp - J_\perp^a)^3}{(2J_\perp + J_\perp^a)^2} \cos 6\varphi \,, \tag{5.16}$$

where N is the number of sites. The correction $\Delta F^{(3)}$ is linear in T reflecting the fact that it is produced by the harmonic fluctuations. It also has the sixfold symmetry in agreement with the $\mathbb{Z}_6$ symmetry breaking in the $m_{3z^2-r^2}$ magnetic structure [70]. The respective term changes sign when $J_\perp^a$ passes through $4J_\perp$, in total agreement with the phase diagram sketched in Fig. 5.1(e) and with the previous findings [82]. For the ratio of parameters $J_\perp^a/J_\perp \sim 1.5$ appropriate for $Er_2Ti_2O_7$, thermal fluctuations select $\varphi = 0, \pi/3, ...$ corresponding to the noncoplanar $m_{3z^2-r^2}$ spin configuration.

5.2.3 Quantum order by disorder

We now set $T = 0$ and use the Rayleigh-Schrödinger perturbation theory to calculate quantum corrections to the classical ground-state energy. We treat S^α as spin operators obeying the standard commutation relations. Again, we focus on the effect of $\hat{V}_2$, which for the quantum case is more conveniently written in terms ladder operators

$$\hat{V}_2 = -\frac{1}{4} \sum_{\langle ij \rangle} M_{ij} (S_i^+ + S_i^-)(S_j^+ + S_j^-) \,. \tag{5.17}$$

It is interesting to note that in comparison with the Heisenberg model the creation/annihilation operator $\hat{V}_{2a}$ and spin-flip hopping operator $\hat{V}_{2b}$ (2.16) have now the same amplitude and can be written in terms of a single $\hat{V}_2$ term.

The second order correction $\Delta E^{(2)}$ (2.21) does not lift the degeneracy. Selection between different ground states is determined by the third-order excitation process described by the diagram

$$|000\rangle \xrightarrow{S_i^- S_j^-} |110\rangle \xrightarrow{S_j^+ S_k^-} |101\rangle \xrightarrow{S_k^+ S_i^+} |000\rangle \tag{5.18}$$

with three sites i, j, k belonging to the same triangular plaquette. The corresponding energy correction is given by a plaquette sum

$$\Delta E^{(3a)} = -\frac{3S^3}{16h^2} \sum_{\triangle} M_{ij} M_{jk} M_{ki} \simeq -\frac{SN}{2304} \frac{(4J_\perp - J_\perp^a)^3}{(2J_\perp + J_\perp^a)^2} \cos 6\varphi \,. \tag{5.19}$$

The quantum correction scales as $\Delta E^{(3)} = O(JS)$ and, thus, represents a harmonic spin-wave contribution. The full harmonic spin-wave calculation is, of course, not restricted to triangular plaquettes and includes graphs of all possible lengths [6]. However, for $J_\perp^a \gtrsim 1$ its angular dependence as well as the corresponding prefactor is very closely reproduced by (5.19), as it is shown in Ref. [83].

The third-order real-space correction also contains a contribution $O(J)$, which goes beyond the harmonic spin-wave theory. Its contribution is described by the diagram

$$|00\rangle \xrightarrow{S_i^- S_j^-} |11\rangle \xrightarrow{S_i^z S_j^z} |11\rangle \xrightarrow{S_i^+ S_j^+} |00\rangle \tag{5.20}$$

and corresponds to a single-bond process that includes interaction of two spin flips generated by $\hat{V}_4$. The expression for the φ - dependent part is

$$\Delta E^{(3b)} = \frac{S^2}{16h^2} \sum_{\langle ij \rangle} M_{ij}^2 h_{ij} \simeq \frac{N}{4608} \frac{(4J_\perp - J_\perp^a)^3}{(2J_\perp + J_\perp^a)^2} \cos 6\varphi \,. \tag{5.21}$$

It exhibits the same functional form as eq. (5.19), but has the opposite sign and, therefore, partially compensates the energy difference between $m_{3z^2-r^2}$ and $m_{x^2-y^2}$ states. Still, for $S \geq 1$ and $J_\perp^a < 4$ the total third-order correction equals to

$$\Delta E^{(3)} \simeq -\left(S - \frac{1}{2}\right) \frac{N}{2308} \frac{(4J_\perp - J_\perp^a)^3}{(2J_\perp + J_\perp^a)^2} \cos 6\varphi \tag{5.22}$$

and selects the $m_{3z^2-r^2}$ states. However, for the case $S = 1/2$ relevant to $Er_2Ti_2O_7$, the two angular-dependent terms cancel each other and one needs to include further corrections or perform a more careful analysis of the real-space perturbation terms. In particular, we modify the quantum perturbation theory by a partial resummation of the infinite series of corrections. We present further details on that in the next subsection, though the main conclusion on the state selection by quantum fluctuations remains intact. For $S = 1/2$ the selected states are the $m_{3z^2-r^2}$ states, while the amplitude of the sixfold harmonics (5.19) is reduced by 40% due to interaction effects.

5.2.4 Quantum perturbation theory for $S = 1/2$

In the previous subsection we have found that the third-order quantum correction $\Delta E^{(3b)}$, resulting from the interaction of two spin flips, cancels the harmonic spin-wave contribution $\Delta E^{(3a)}$ leaving intact the degeneracy between $m_{3z^2-r^2}$ and $m_{x^2-y^2}$ states when $S = 1/2$. To treat more carefully interaction effects we adopt a modified real-space expansion based on a partial rearrangement of the perturbation terms in Eq. (5.14). Specifically, $\hat{V}_4$ is now included into a new unperturbed Hamiltonian

$$\hat{\mathcal{H}}_0' = h \sum_i (S - S_i^z) + \sum_{\langle ij \rangle} h_{ij} (S - S_i^z)(S - S_j^z) \,. \tag{5.23}$$

In this way the Ising part of spin-flip interaction is treated exactly. Basically, the new expansion corresponds to resummation of an infinite subset of terms in the original real-space approach. A similar trick was also applied in Ref. [84] for the Ising expansion at the fractional magnetisation plateaus.

The main difference between the two forms of the real-space expansion is in assignment of excitation energies in (2.18) and (2.20). The lowest-energy excitation, a pair of spin-flips on the same bond, costs now $E_n - E_0 = 2h + h_{ij}$. We rewrite it as

$$E_n - E_0 = \frac{1}{6}(2J_\perp + J_\perp^a)\eta + \frac{1}{6}(4J_\perp - J_\perp^a)\cos(2\varphi + \gamma_{ij})\,, \tag{5.24}$$

with $\eta = (12S - 1)$. We will use $1/\eta$ as a small parameter to decompose the excitation energy denominator. In fact, this expansion has the same physical sense, as the whole real space perturbation decomposition as $1/\eta \sim h_{ij}/h \sim 1/z$. The rest of the quantum real space perturbation theory is the same. So we can use the diagrammatic technique with the remaining interaction terms. In the second and third orders only $\hat{V}_2$ will contribute. Below we calculate both contributions, keeping the lowest order terms up to $O\left(\eta^{-3}\right)$ and dropping all unessential constants.

The second-order energy correction corresponds to single-bond processes and is expressed by

$$\Delta E^{(2)} = -\frac{S^2}{4}\sum_{\langle ij\rangle}\frac{M_{ij}^2}{2h + h_{ij}}\,. \tag{5.25}$$

After some simple but somewhat cumbersome algebra one obtains

$$\Delta E^{(2)} \simeq \frac{1}{32}\frac{NS^2}{\eta^3}\frac{(4J_\perp - J_\perp^a)^3}{(2J_\perp + J_\perp^a)^2}(\eta - 2)\cos 6\varphi\,. \tag{5.26}$$

For large S this expression matches exactly with the corresponding term in $\Delta E^{(3b)}$ (5.21).

In the third order, there is only a triangular cluster process, which provides the energy shift

$$\Delta E^{(3)} = -\frac{S^3}{4}\sum_{\triangle}\sum_{\langle jk\rangle\in\triangle}\frac{M_{ij}M_{ki}M_{kj}}{(2h + h_{ij})(2h + h_{ik})}\,. \tag{5.27}$$

The second sum here denotes different possible links with hopping operator $S_j^+S_k^- + h.c.$ on a plaquette. We also calculate it expanding in powers of $1/\eta$ as

$$\Delta E^{(3)} \simeq -\frac{1}{192}\frac{NS^2}{\eta^3}\frac{(4J_\perp - J_\perp^a)^3}{(2J_\perp + J_\perp^a)^2}\left(\eta^2 + \eta + \frac{3}{4}\frac{(4J_\perp - J_\perp^a)^2}{(2J_\perp + J_\perp^a)^2}\right)\cos 6\varphi\,. \tag{5.28}$$

The first leading term again matches the angular-dependent part of the previous expression (5.19).

Comparing now $\Delta E^{(2)}$ and $\Delta E^{(3)}$, we do see the cancellation of the leading $1/\eta$ terms for $S = 1/2$. Still the coefficient in front of the cosine is negative:

$$\Delta E = -\frac{N}{8000}\frac{(4J_\perp - J_\perp^a)^3}{(2J_\perp + J_\perp^a)^2}\left(1 + \frac{1}{16}\frac{(4J_\perp - J_\perp^a)^2}{(2J_\perp + J_\perp^a)^2}\right)\cos 6\varphi\,. \tag{5.29}$$

Thus, for $S = 1/2$ the quantum order by disorder selection acts in the same way as for large spins. The main consequence of spin flip interactions is ∼ 40% reduction of the amplitude of the cosine harmonics as compared to the noninteracting result (5.19).

5.3 Order by structural disorder

Building on the previous works about order by structural disorder in frustrated systems [21, 22, 24] and foremost on our results on the triangular antiferromagnet with impurities of chapter 4 we study the effect of lattice defects on the ground state of the XY anisotropic pyrochlore antiferromagnet. We show that the impact of quenched disorder in the form of weak vacancies or weak bond disorder on the ground state of the system can be described by an effective $\cos 6\varphi$ anisotropy term with the *positive* sign. Thus defects favour the opposite configurations in comparison with the ones, selected by fluctuations (see sec. 5.2). For $\mathrm{Er_2Ti_2O_7}$ this implies stabilisation of the $m_{x^2-y^2}$ spin configuration.

Also, recently Andreanov and McClarty [85] studied spin textures around vacancies in the same model. By minimising the energy of the system with missing spins they reached similar conclusions of the $m_{x^2-y^2}$ state selection by vacancies in $\mathrm{Er_2Ti_2O_7}$. They also showed, that this scenario is realized already when a single impurity is placed on a lattice.

Technically impurities in $\mathrm{Er_2Ti_2O_7}$ may arise from the substitution of magnetic Er^{3+} ion by a nonmagnetic Y^{3+}, which has a very similar ionic radius. Similar defects were considered in Ising pyrochlores $\mathrm{Dy_{2-x}Y_xTi_2O_7}$ and $\mathrm{Ho_{2-x}Y_xTi_2O_7}$ [86, 87] with spin-ice ground state. Besides, substitution of nonmagnetic Ti^{4+} by a magnetic erbium ion may lead to a random bond-like disorder, like in $\mathrm{Yb_{2+x}Ti_{2-x}O_7}$ [88].

5.3.1 Nonmagnetic impurities

To study analytically the effect of spin vacancies we use a toy model of weak site disorder [21]. Specifically, we let some fraction n_{imp} of classical spins to be shorter by a small amount $\epsilon \ll 1$. These impurities are distributed randomly over the lattice and we assign a parameter $p_i = 1$ to every impurity spin and $p_i = 0$ otherwise: $\sum_i p_i = N_{\mathrm{imp}}$. In the spin Hamiltonian impurities are included by substitution $\mathbf{S}_i \to \mathbf{S}_i(1-\epsilon p_i)$ and to leading order in ϵ we have for pairwise spin-spin interactions $S_i^\alpha S_j^\beta \to S_i^\alpha S_j^\beta\,[1-\epsilon(p_i+p_j)]$.

We perform the same decomposition of the spin Hamiltonian as described in sec. 5.2. There are two main differences with the preceding section: the noninteracting Hamiltonian gets renormalised in the presence of impurities, and the part of the Hamiltonian, linear in spin deviations $\hat{V}_1$ does not vanish:

$$\hat{\mathcal{H}}_0 = \frac{h}{2S}\sum_i \left[S_i^{x2}+S_i^{y2}\right]\left(1-\epsilon p_i - \frac{S\epsilon}{h}\sum_{j=1}^{6}{}' p_j h_{ij}\right); \tag{5.30}$$

$$\hat{V}_1 = S\sum_{\langle ij\rangle} K_{ij}\epsilon\,(p_i+p_j)\,(S_i^x+S_j^x)\,, \tag{5.31}$$

describing the fact that spins that are adjacent to impurities tilt from their equilibrium orientations in the bulk. Minimisation of the quadratic form $\hat{\mathcal{H}}_0+\hat{V}_1$ over S_i^x gives

$$S_i^x = \frac{S^2\epsilon}{h}\,\frac{\sum_{j=1}^{6}{}' K_{ij}p_j}{1-\epsilon p_i - \frac{S\epsilon}{h}\sum_{j=1}^{6}{}' h_{ij}p_j}\,, \tag{5.32}$$

similar to what was obtained for the triangular system (2.32). Substitution of this new minimum condition into $\hat{\mathcal{H}}_0+\hat{V}_1$ produces an energy correction in the form an effective biquadractic exchange. As before, for the easy-plane pyrochlore this energy correction is independent of the angle φ. According to derivations of section 2.2, the leading third order term $\Delta E^{(2)}$ comes from the substitution of S_i^x into the interaction term $\hat{V}_2 = -\sum_{\langle ij\rangle} M_{ij} S_i^x S_j^x$. We restrict ourselves to the lowest order in impurity strength ϵ and concentration n_{imp}, as it is done in section 2.2. then the correction takes the form

$$\Delta E^{(2)} = -\frac{S^4\epsilon^2}{h^2} \sum_{\langle ij\rangle} \sum_{k=1}^{2}{}'' M_{ij} K_{ik} K_{jk} p_k^3 \,, \tag{5.33}$$

where the last summation is over two sites sharing the same tetrahedron with i and j. Finally, substituting the expressions for bond-dependent parameters M_{ij} and K_{ij} from (5.13) we obtain

$$\Delta E^{(2)} \simeq \frac{S^2\epsilon^2 N n_{\text{imp}}}{144} \, \frac{(4J_\perp - J_\perp^a)^3}{(2J_\perp + J_\perp^a)^2} \cos 6\varphi \,. \tag{5.34}$$

This total energy correction has the sixfold symmetry, but the opposite sign compared to Eqs. (5.16) and (5.19). Hence, for $J_\perp^a < 4J_\perp$ the on-site disorder favours magnetic configurations (5.9) with $\varphi = \pi(1+2n)/6$. These correspond to six coplanar $m_{x^2-y^2}$ states.

5.3.2 Bond disorder

Another type of randomness in magnetic solids is bond disorder. In pyrochlore materials it may appear as a result of doping on the nonmagnetic B sites. We model this type of disorder by small random variation of $J_\perp$ and $J_\perp^a$:

$$J_\perp \longrightarrow J_\perp^{ij} = J_\perp(1+\delta_{ij}) \,, \qquad J_\perp^a \longrightarrow J_\perp^{a\,ij} = J_\perp^a(1+\delta_{ij}) \,. \tag{5.35}$$

The fluctuating part δ_{ij} is assumed to be uncorrelated between adjacent bonds and relatively small, $\langle \delta_{ij}^2 \rangle = D \ll 1$, such that it does not change the sign of the exchange constants.

The subsequent calculation is completely similar to the previous subsection up to a substitution $\epsilon(p_i + p_j) \to \delta_{ij}$. The state-dependent energy correction has the form

$$\Delta E^{(3)} = -\frac{S^4}{h^2} \sum_{\langle ij\rangle} M_{ij} K_{ij}^2 \delta_{ij}^2 \simeq \frac{S^2 D N}{288} \, \frac{(4J_\perp - J_\perp^a)^3}{(2J_\perp + J_\perp^a)^2} \cos 6\varphi. \tag{5.36}$$

Again, we obtain that structural disorder has the same tendency of lifting the degeneracy in favour of $m_{x^2-y^2}$ states independent of the form of quenched randomness. Both weak impurities and bond disorder thus compete with the conventional order by disorder mechanism and select the contrary spin configurations.

5.4 Numerical results

In this section the analytic results obtained for weak disorder are corroborated by a numerical investigation of genuine vacancies in the classical anisotropic XY pyrochlore antiferromagnet. For that we return back to the original spin Hamiltonian

$$\hat{\mathcal{H}} = \sum_{\langle ij\rangle} J_\perp \mathbf{S}_i^\perp \cdot \mathbf{S}_j^\perp + J_\perp^a (\mathbf{S}_i^\perp \cdot \hat{\mathbf{r}}_{ij})(\mathbf{S}_j^\perp \cdot \hat{\mathbf{r}}_{ij}) \tag{5.37}$$

and set $J_\perp = 1$, in other words, we measure T and $J_\perp^a$ in the units of $J_\perp$. In three dimensions vacancies are on average situated close to each other already for small doping concentrations making it difficult to observe experimentally a single impurity behaviour. Therefore, we consider outright a finite density of impurities. Overall, two types of numerical data are considered: determination of the ground-state magnetic structure at zero temperature and Monte Carlo simulations of finite-temperature properties. In both cases numerical computations were performed on periodic clusters of $N = 4L^3$ classical spins. Random vacancies were introduced by setting $|\mathbf{S}_i| = 0$ for a fixed number of sites $N_{\rm imp} = n_{\rm imp}N$. For all computations we employed about 100 independent impurity configurations used to average numerical data and to estimate the error bars.

For $J_\perp^a > 0$, magnetic states of the XY pyrochlore antiferromagnet are characterised by two order parameters. The first one, m discriminates ordering within the E-manifold from other irreducible representations of the tetrahedral group

$$m = \sqrt{m_x^2 + m_y^2}, \qquad m_x = \frac{1}{N}\sum_i \mathbf{S}_i \cdot \hat{\mathbf{x}}_i\,, \qquad m_y = \frac{1}{N}\sum_i \mathbf{S}_i \cdot \hat{\mathbf{y}}_i. \tag{5.38}$$

Here, two components m_x and m_y are defined using the above choice of axes in the local xy planes, see eq. (5.8). The clock order parameter $m_6 = m\cos 6\varphi$ distinguishes between the different E-states [70] and is in fact the main interest of this study.

$$m_6 = \frac{1}{m^5}\,\mathrm{Re}\{(m_x + im_y)^6\}. \tag{5.39}$$

m_6 has a positive value for six noncoplanar states $m_{3z^2-r^2}$ and becomes negative for coplanar spin configurations $m_{x^2-y^2}$.

5.4.1 Ground state minimisation

We begin with minimisation of the classical energy (5.37) for a fixed concentration of static vacancies. The method consists of solving iteratively the classical energy minimum condition for each spin $\mathbf{S}_i = \mathbf{h}_i/|\mathbf{h}_i|$ and therefore moving down the energy landscape on each step. More details on the method can be found in section 3.3. For each value of the anisotropy parameter $J_\perp^a > 0$ we performed numerical minimisation for several cluster-sizes up to $L = 20$. For each measurement we used up to $5 \cdot 10^3$ random initial conditions with the number increasing for larger clusters, and $N_{\rm repl} = 96$ ($N_{\rm repl} = 192$ for $n_{\rm imp} = 0.5\%$) different impurity replicas.

Figure 5.2 shows our results for the clock order parameter m_6 in the XY pyrochlore antiferromagnet with $n_{\rm imp} = 5\%$ of nonmagnetic impurities. Negative values of m_6 confirm appearance of the coplanar $m_{x^2-y^2}$ state induced by impurities for $J_\perp^a < 4$. The absolute value of the order parameter grows with increasing cluster size, leaving no doubts about the existence of the true long-range order. Note that a nonzero value of $1 - |m_6|$ for $L \to \infty$ signifies small spin canting from an ideal $m_{x^2-y^2}$ magnetic structure, which appears due to local lifting of frustration and is, finally, responsible for the selection of the coplanar state.

For large $J_\perp^a > 4$, which is not relevant for $Er_2Ti_2O_7$, but may be realised in other anisotropic pyrochlores, random impurities stabilise the noncoplanar $m_{3z^2-r^2}$ magnetic structure characterised by positive $m_6 > 0$. The value $J_\perp^a = 4$ corresponds to the isotropic XY spin model in the site-dependent local frame. Consequently, two states, $m_{3z^2-r^2}$ and $m_{x^2-y^2}$, remain exactly degenerate

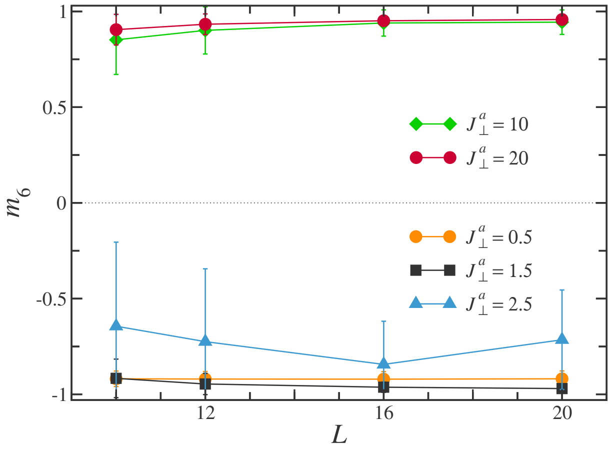

Figure 5.2: Zero-temperature energy minimisation results for the clock order parameter m_6 obtained for an XY pyrochlore antiferromagnet with $n_{\rm imp} = 5\%$ of nonmagnetic impurities for several cluster sizes L and different values of the anisotropic exchange $J^a_\perp$. Positive and negative values of m_6 correspond to $m_{3z^2-r^2}$ and $m_{x^2-y^2}$ magnetic states, respectively.

for this value of $J^a_\perp$: neither thermal/quantum fluctuations [82], nor impurities (Sec. 5.3) can lift this degeneracy determined by an emergent $SO(2)$ rotational symmetry of the spin Hamiltonian. For $J^a_\perp$ close to 4, convergence of the iterative procedure becomes very slow, see the $L = 20$ point for $J^a_\perp = 2.5$ in Fig. 5.2. One needs to employ a significantly larger number of initial configurations to approach the true minimum state. This may indicate the development of some type of glassiness in the system. The similar effect is also present for very small $J^a_\perp \lesssim 0.1$ because of an additional degeneracy appearing for $J^a_\perp = 0$. Finally, we also studied different impurity concentrations in the range $0.5\% < n_{\rm imp} < 7\%$ and obtained the ground state selection independent of $n_{\rm imp}$.

5.4.2 Monte Carlo simulations

Monte Carlo simulations of the classical XY pyrochlore antiferromagnet were performed using the Metropolis algorithm alternating five Metropolis steps with five microcanonical overrelaxation sweeps before every measurement. In total, $2\cdot 10^5$ measurements were taken at every temperature and averaging was done over 96 impurity configurations. Refer to section 3.1.5 for more details of the algorithm. We simulated the model (5.37) in the range of the anisotropy parameter $0.3 \leq J^a_\perp \leq 2$ and impurity concentration $0 < n_{\rm imp} < 10\%$.

The temperature dependence of the two order parameters m and m_6, defined in (5.38) and (5.39), for $J^a_\perp = 0.5$ and $n_{\rm imp} = 5\%$ is shown in Fig. 5.3. The transition temperature $T_c = 0.415$ was determined from intersection of Binder cumulants $U_L = \langle m^4\rangle/\langle m^2\rangle^2$ (see inset of Fig. 5.3). The obtained $T_C = 0.415(5)$ is somewhat reduced compared to the transition into the pure model $T^0_c = 0.4454$ for the same value of $J^a_\perp$, which is a usual behaviour of diluted magnetic systems. The critical behaviour of the model (5.37) belongs to the 3D XY universality class [70] with the known value of the correlation length exponent $\nu \approx 0.672$ [89]. We can now use the Harris criterion, [60] which states that the critical behaviour for phase transitions with $d\nu > 2$ remains unchanged in the presence of disorder. Since ν is slightly larger than 2/3, the critical point in the

XY pyrochlore antiferromagnet remains unaffected upon dilution with nonmagnetic impurities. Observation and confirmation of this fact is an interesting challenge, which is left out of the scope of this work as we did not perform a precise enough FSS analysis

Nevertheless, the diluted antiferromagnet exhibits a peculiar temperature dependence of the clock order parameter m_6, see the right panel of Fig. 5.3. Just below T_c, m_6 is positive, as expected for the $m_{3z^2-r^2}$ state, and grows at fixed T with the system size L. Such 'inverse' finite-size scaling is attributed to the dangerously irrelevant role of the sixfold anisotropy in the XY transition in three dimensions and is explained by the presence of an additional length-scale $\xi_6 \gg \xi$ [70]. Upon further cooling, the clock order parameter shows a sharp jump to negative values at $T_1 \approx 0.12$. This jump signifies a phase transition into the $m_{x^2-y^2}$ state stabilised by impurities. Basically, the temperature dependence of m_6 is determined by competition of two terms: the impurity correction ΔE_2 given by eq. (5.34) and the free-energy correction $\Delta F^{(3)}$ generated by thermal fluctuations (5.16). They have different signs and at $T \to 0$ the impurity contribution dominates selecting the $m_{x^2-y^2}$ state. However, thermal fluctuations grow with temperature and above T_1 the effective anisotropy $\Delta F^{(3)}$ wins over ΔE_2 leading to the $m_{3z^2-r^2}$ state right below T_c.

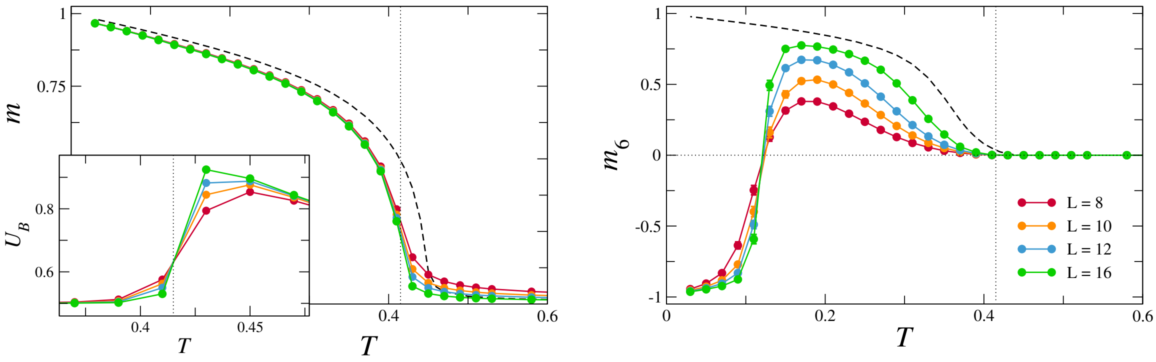

Figure 5.3: Finite size analysis of the Monte Carlo results for the antiferromagnetic m (left panel) and the clock m_6 (right panel) order parameters for the XY pyrochlore antiferromagnet (5.37) with $J^a_\perp = 0.5$ and 5% of vacancies. The dotted vertical line indicates the transition temperature. Dashed lines show the behaviour of m and m_6 for a pure system with $L = 16$. The inset shows the crossing of Binder cumulants, which is used to define T_C.

The phase transition between $m_{3z^2-r^2}$ and $m_{x^2-y^2}$ states is expected to be of the first order on symmetry grounds. (Another possibility is two closely located second-order transitions with an intermediate low-symmetry phase.) We collected histograms for the clock order parameter m_6 for a few impurity concentrations, which confirm the first-order nature of the transition. On the other hand, no anomaly is seen in the specific heat or magnetic susceptibility even for the largest clusters. Thermodynamic signatures of the first-order transition appear to be blurred by the disorder. Such behaviour is similar to what was observed in the previous chapter, where a triangular antiferromagnet was studied.

The observed sequence of ordered phases remains stable under variations of n_{imp} and $J^a_\perp$. Figure 5.4 shows dependence on vacancy concentration for $J^a_\perp = 0.3$. We include only Monte Carlo results for the largest clusters with $L = 16$. The first-order transition temperature progressively grows between $T_1 = 0.025$ for $n_{\text{imp}} = 1\%$ to $T_1 = 0.125$ for $n_{\text{imp}} = 10\%$. The order parameter

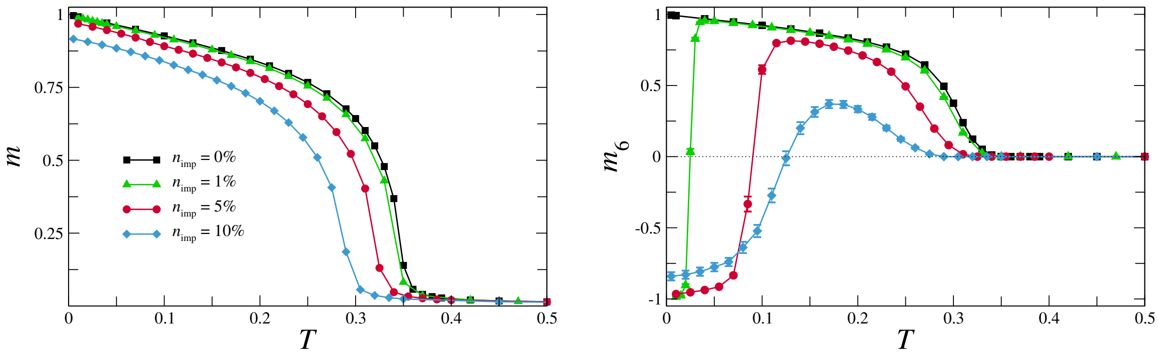

Figure 5.4: Temperature dependence of the magnetic order parameters for different impurity concentrations. Monte Carlo results are for $J_\perp^a = 0.3$ and $L = 16$.

jump is very sharp for the lowest impurity concentration, but becomes significantly smeared for $n_{\text{imp}} = 10\%$. We attribute this effect to a substantial finite-size scaling at large impurity concentrations. Monte Carlo simulations of significantly bigger clusters are required for a precise determination of the transition point between the two E states for large density of vacancies.

Finally, dependence on $J_\perp^a$ is illustrated in Fig. 5.5. As expected, the $m_{x^2-y^2}$ state is present at low temperatures for all studied values of the anisotropic exchange, including $J_\perp^a = 1.5$, which is very close to the experimental estimate of $Er_2Ti_2O_7$. Somewhat surprisingly, the thermal selection of the $m_{3z^2-r^2}$ state in the vicinity of T_c is also remarkably stable under variations of n_{imp} or $J_\perp^a$. This can be considered as a consequence of the Harris criterion, which asserts irrelevance of quenched disorder for transitions in the 3D XY universality class.

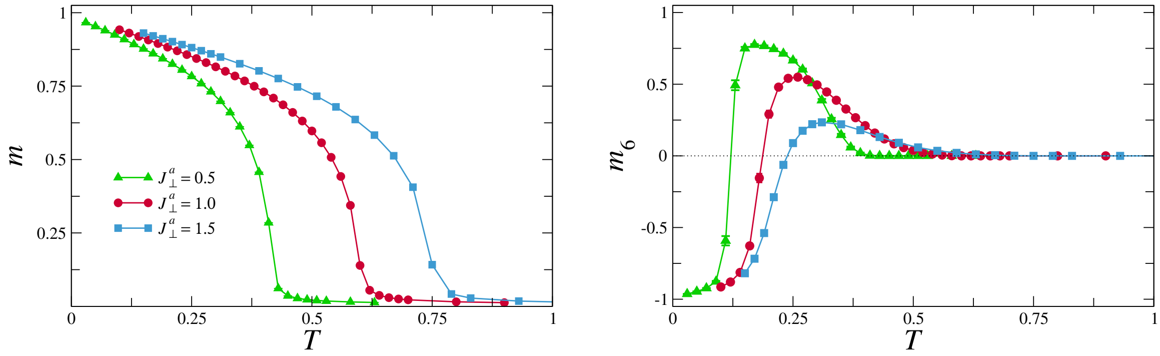

Figure 5.5: Temperature dependence of the magnetic order parameters for fixed impurity concentration $n_{\text{imp}} = 5\%$ and different values of $J_\perp^a$. Monte Carlo results are for $L = 16$ clusters.

5.5 Structural vs quantum disorder and observation perspectives

The Monte Carlo results of the previous section give a general idea about competition between impurities and thermal fluctuations in the ground-state selection. Beyond the classical model, similar competition exists also for the structural disorder and quantum effects, even at $T = 0$. There must be a critical impurity concentration above which the quantum selection gives way to the spin configurations stabilised by vacancies. Since the energy gain produced by impurity substitution is a purely classical effect, the critical impurity concentration scales with the spin length as $n_c \sim 1/S$. This raises a legitimate question about observability of the structural order from disorder effect in spin-1/2 frustrated magnets, in particular, in diluted $\mathrm{Er_2Ti_2O_7}$.

Even an approximate calculation of n_c is a fairly difficult theoretical problem. One can calculate the harmonic energy correction from quantum fluctuations as well as relaxation energy gain due to impurities. However, direct comparison of these quantities is complicated by the fact that competing $m_{3z^2-r^2}$ and $m_{x^2-y^2}$ configurations cease to be the classical ground states in the presence of impurities and, hence have ill-defined harmonic excitation spectra.

Here, we circumvent the difficulty of treating nonlinear quantum effects for an impurity-induced spin texture in $\mathrm{Er_2Ti_2O_7}$, by assuming that concentration of vacancies is low. Then, the quantum energy correction can be approximated by that for the pure $S = 1/2$ pyrochlore antiferromagnet (5.19), whereas the classical energy gain from impurities is estimated from eq. (5.34) by substituting $\epsilon = 1$. In this way we obtain a rather large but not excessive value of the critical impurity concentration $n_c \approx 14\%$ being only weakly dependent on the exchange constants $J_\perp$ and $J^a_\perp$.

Instead of using the harmonic results, we can regard further degeneracy breaking corrections, where renormalisation by the anharmonic processes is taken into account. For quantum selection it implies considering a correction (5.21). Or a more accurate result (5.29) with a 40% reduced amplitude of the sixfold harmonics due to renormalisation by interaction effects. For the structural disorder correction in the limit $\epsilon \to 1$ we need to calculate the correction of the kind (2.37). It is caused by the reduction of the strength of the local field and is of the same order in $1/z$ expansion. Following the path of section 2.2.1 we obtain

$$\Delta E^{(3)} \simeq -\frac{S^2\epsilon^3 N n_{\mathrm{imp}}}{288}\,\frac{(4J_\perp - J^a_\perp)^3}{(2J_\perp + J^a_\perp)^2}\cos 6\varphi\,. \tag{5.40}$$

It also renormalises the harmonic result, but not the overall selection sign. Comparing the prefactors of ΔE_Q from (5.29) and $\Delta E^{(2)} + \Delta E^{(3)}$, we obtain the similar $n_c \approx 15\%$.

Undoubtedly, the above estimate is rather crude and there are good chances that the critical impurity concentration for $\mathrm{Er_2Ti_2O_7}$ is smaller than the estimates above. We have seen that inclusion of the higher order corrections can cause significant renormalisation of the strength of degeneracy breaking terms. Moreover, the approximation adopted for derivation of (5.34) treats only tilting of nearest-neighbour spins around a vacancy. Inclusion of full-range spin relaxation in an impurity-induced magnetic texture should further increase the corresponding energy gain and, hence reduce the critical value of n_{imp}. Nevertheless, Niven *et al.* [90] found that long range order in diluted $\mathrm{Er_2Ti_{2(1-x)}Y_{2x}O_7}$ persists for $x \lesssim 18\%$. Therefore, we conclude that even for rather conservative estimate $n_c = 15\%$ the experimental observation of impurity-induced $m_{x^2-y^2}$ phase in $\mathrm{Er_2Ti_2O_7}$ is very likely.

Chapter 6

Pyrochlore in external magnetic field

Most of the experimental studies, performed on $Er_2Ti_2O_7$ are made under an applied magnetic field. At the same time, an extensive theoretical description of this easy-plane pyrochlore in a magnetic field has been lacking so far. One of the reasons for it may be the relative simplicity of the observed $H-T$ phase diagrams [69, 79, 91, 92]: no phase transitions inside the ordered phase has yet been detected. The only exception may be the magnetisation curves of Petrenko *et al.* [92], which show extra features in magnetic susceptibility at very low field for $\mathbf{H} \parallel [110]$ and [001] directions.

In this study we present a theory of the easy-plane pyrochlore antiferromagnet in an external magnetic field. In particular, we investigate the evolution of the spin structure inside the antiferromagnetically ordered phase. Basing on the symmetry analysis and on low-H perturbative calculations, we predict that the magnetic field lifts the emergent $U(1)$ symmetry of the ground state of the model. Remarkably, its effect varies depending on the direction of H. We predict the presence of the nontrivial phases well inside the long-range ordered state when $\mathbf{H} \parallel \langle 001 \rangle$ and $\mathbf{H} \parallel \langle 111 \rangle$. On the other hand, field evolution of the antiferromagnetic structure in the $\mathbf{H} \parallel \langle 110 \rangle$ case is continuous and does not undergo a phase transition.

These findings can be applied to real $Er_2Ti_2O_7$ compound: the benchmark of our theory will be the detection of the phase transition when $\mathbf{H} \parallel [001]$ and its absence in the other case $\mathbf{H} \parallel [110]$. Value of the critical field will allow to quantify the strength of quantum order by disorder at zero field. So far, the predicted positions of the paramagnet-antiferromagnet phase boundaries for three field direction, obtained with our Monte Carlo simulations at $T \to 0$, are is in good agreement with the experimental results.

The organisation of the chapter is the following: first, we perform a symmetry analysis and anticipate the general form of the terms, responsible for selecting a ground state of $Er_2Ti_2O_7$ in the presence of the magnetic field. Then in section 6.2 treating the Zeeman term as perturbation and minimising the energy of the system, we obtain the analytic expression for these degeneracy lifting terms in the limit of low magnetic field. Section 6.3 contains the results of our Monte Carlo simulations of the system. In particular, we present the $H-T$ phase diagrams of the classical model, which agree well with the analytical predictions of the symmetry analysis. In the next section 6.4 we consider quantum corrections to the theory. They are treated within the framework real space perturbation theory, developed in the previous chapter. We also make predictions for the phase transition location in the real system. Finally, our findings and predictions are summarised in section 6.5.

6.1 Landau symmetry analysis

In this section we obtain the general form of the lowest order anisotropy terms in the free energy that are allowed by symmetry. When the magnetic field is absent, these terms have the $\cos 6\varphi$ form, which is in total agreement with effective anisotropies, generated by fluctuations or structural disorder, as was presented in the previous chapter. The presence of the magnetic field gives way to lower harmonics of φ. The sign and the exact form of the term will depend on the direction of $\mathbf{H}$. Motivated by the results of our numerical simulations, which showed an additional phase transition for the $\mathbf{H} \parallel \langle 111\rangle$ case, we go further and obtain the form of the subleading anisotropy term.

The minimal model that describes well the low temperature properties of $Er_2Ti_2O_7$ was introduced in the previous chapter. In the presence of an external field it has the form

$$\hat{\mathcal{H}} = \sum_{\langle ij\rangle} J_\perp \mathbf{S}_i^\perp \cdot \mathbf{S}_j^\perp + J_\perp^a (\mathbf{S}_i^\perp \cdot \hat{\mathbf{r}}_{ij})(\mathbf{S}_j^\perp \cdot \hat{\mathbf{r}}_{ij}) - \sum_i g_{\alpha\beta} H_i^\alpha S_i^\beta . \tag{6.1}$$

When $H = 0$ the magnetic structure of the ground state transforms under E or T_2 irreducible representation (irrep) depending on the sign of of anisotropic exchange $J_\perp^a$. As in the previous chapter we are interested in the $J_\perp^a > 0$ case, for which on the mean-field level the continuous manifold of states has the same lowest energy $E_{\mathrm{MF}} = -J_\perp - 1/2 J_\perp^a$. In the coordinate frame, defined by the (5.8) these states can be parameterised by a single variable φ

$$\mathbf{S}_i = S\left(\hat{\mathbf{x}}_i \cos\varphi + \hat{\mathbf{y}}_i \sin\varphi\right). \tag{6.2}$$

Beyond the mean-field approximation this emergent $U(1)$ symmetry is lifted, for example, via the order by disorder process. Application of external field can also select certain states from the degenerate manifold (6.2). Below we present the symmetry analysis, which allows to anticipate the general form of the free energy corrections with the nontrivial dependence on φ.

We start the analysis with the list of possible symmetry operations that leave the pyrochlore lattice invariant. They are presented in the character table of the tetrahedral point group T_d (Fig. 6.1 (a)). We also show the examples of rotation axes C_3, C_2, S_4 and a mirror plane σ_d in figure 6.1 (b). The ground state (6.2) belongs to the two component E irrep with basis vectors m_x and m_y with the following transformation properties:

$$\begin{aligned} m_x &= \sum_i \mathbf{S}_i \cdot \hat{\mathbf{x}}_i, & m_x &\sim z^2 - \frac{1}{2}x^2 - \frac{1}{2}y^2, \\ m_y &= \sum_i \mathbf{S}_i \cdot \hat{\mathbf{y}}_i, & m_y &\sim \frac{\sqrt{3}}{2}(x^2 - y^2). \end{aligned} \tag{6.3}$$

To construct nontrivial invariants it is practical to consider structures of the kind

$$m_x \pm i m_y \sim \mathrm{e}^{\pm 2\pi i/3} x^2 + \mathrm{e}^{\mp \frac{2\pi i}{3}} y^2 + z^2. \tag{6.4}$$

$\mathbf{T_d}$	E	$8C_3$	$3C_2$	$6S_4$	$6\sigma_d$
A_1	1	1	1	1	1
A_2	1	1	1	-1	-1
E	2	-1	2	0	0
T_1	3	0	-1	1	-1
T_2	3	0	-1	-1	1

(a) Character table of T_d.

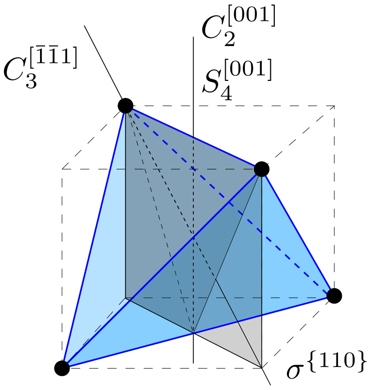

(b) Visualisation of the symmetry elements of T_d. Twofold and improper fourfold rotation axis coincide. The mirror plane $\sigma^{\{110\}}$ is shown in grey.

Figure 6.1: Symmetry of the tetrahedral point group T_d

They are directly related to the variable φ, which parameterises different ground states: $m_x \pm im_y = m\mathrm{e}^{\pm i\varphi}$. Also, they have simple transformation properties:

$$\begin{aligned} C_3^{[111]}(m_x \pm im_y) &= \mathrm{e}^{\mp 2\pi i/3}(m_x \pm im_y), \\ C_2^{[001]}(m_x \pm im_y) &= m_x \pm im_y, \\ \sigma_d^{\{110\}}(m_x \pm im_y) &= m_x \mp im_y, \\ S_4^{[001]}(m_x \pm im_y) &= m_x \mp im_y, \\ T(m_x \pm im_y) &= -(m_x \pm im_y). \end{aligned} \tag{6.5}$$

The last equality describes transformation properties under time-reversal operation. Eqs. (6.5) lead to a set of restrictions on the invariant combination, constructed from $m_x \pm im_y$: i) the power k of $(m_x \pm im_y)^k$ should be a multiple of three and even; ii) the invariant has to be an even function of $m_{x,y}$ and real. All these conditions are satisfied for the term

$$\Delta F = -A_6^{\mathrm{ObD}}\left[(m_x + im_y)^6 + (m_x - im_y)^6\right] = -A_6^{\mathrm{ObD}} m^6 \cos 6\varphi. \tag{6.6}$$

It is exactly the sixfold anisotropy term that represented fluctuation selection in the previous chapter

Introduction of the mixing of m with the magnetic field allows to construct additional invariants. H transforms under a three-component T_1 representation of T_d, here are its transformation properties under the symmetry operations

$$\begin{aligned} C_3^{[111]}\ (H_x, H_y, H_z) &= (H_y, H_z, H_x), \\ C_2^{[001]}\ (H_x, H_y, H_z) &= (-H_x, -H_y, H_z), \\ \sigma_d^{\{110\}}\ (H_x, H_y, H_z) &= (H_y, H_x, H_z), \\ S_4^{[001]}\ (H_x, H_y, H_z) &= (H_y, -H_x, -H_z), \\ T\ (H_x, H_y, H_z) &= -(H_x, H_y, H_z). \end{aligned} \tag{6.7}$$

In antiferromagnets linear in H invariants are absent, therefore first, we consider the symmetrised direct product

$$\{T_1 \otimes T_1\} = A_1 + E + T_1. \tag{6.8}$$

The scalar component - is of course the magnitude of magnetic field $H^2 \sim A_1$, which is invariant under all symmetry operations. Therefore, the simplest possible term that breaks the ground state degeneracy can be constructed as

$$\Delta F = A_6 H^2 m^6 \cos 6\varphi. \tag{6.9}$$

However, it is not the only invariant quadratic in H. Let's consider the E component of eq. (6.8) with the basis

$$h_x = H_z^2 - \frac{1}{2}H_x^2 - \frac{1}{2}H_y^2; \qquad h_y = \frac{\sqrt{3}}{2}\left(H_x^2 - H_y^2\right). \tag{6.10}$$

One can make a scalar out of the direct product of two or more E irreps as $\{E \otimes E\} = A_1 + A_2 + E$. This scalar will be the desired invariant, if we take

$$\Delta F = A_2\left[(m_x + im_y)^2(h_x + ih_y) + (m_x - im_y)^2(h_x - ih_y)\right]. \tag{6.11}$$

Substituting expressions (6.10) we get

$$\Delta F = A_2 m^2\left[\left(H_z^2 - \frac{1}{2}H_x^2 - \frac{1}{2}H_y^2\right)\cos 2\varphi - \frac{\sqrt{3}}{2}\left(H_x^2 - H_y^2\right)\sin 2\varphi\right]. \tag{6.12}$$

This term is only quadratic in the order parameter m, and usually prevails over (6.9). Different directions of the magnetic field, introduced into (6.12) will produce various two-minima selection with the angles φ and $\varphi + \pi$. The only exception would be the field along the trigonal axis $\mathbf{H} \parallel \langle 111\rangle$. In this case both terms in (6.12) vanish. It happens because this direction of magnetic field is orthogonal to the components h_x and h_y.

The interplay of leading in H degeneracy breaking terms (6.9) and (6.12) define ordered structure for any field direction. However, our numerical simulations, which will be presented further in the chapter, do not support the scenario of ordering by only a sixfold term when $\mathbf{H} \parallel \langle 111\rangle$. The high-field ordered state does not correspond to any of selection terms (6.9) or (6.12). It is the reason why we go on in our analysis and obtain the following cubic in H correction to the free energy. The decomposition of H^3 over irreducible representations is governed by

$$\{\{T_1 \otimes T_1\} \otimes T_1\} = A_1 + E + 3T_1. \tag{6.13}$$

As we have seen before the E component is absent in the $\mathbf{H} \parallel \langle 111\rangle$ case. Mixing of T_1 with E from the order parameter can not produce a scalar invariant combination either. Instead, the $H_x H_y H_z \sim A_1$ combination can be coupled to a scalar, generated from the corresponding power of the order parameter. In the presence of H^3 term the constraint of T-invariance in (6.5) now demands for the odd power of m, so the cubic term is allowed

$$\Delta F = A_3 H_x H_y H_z\left[(m_x + im_y)^3 + (m_x - im_y)^3\right]. \tag{6.14}$$

It is interesting to note that cubic contribution vanishes for the other two directions of magnetic field $\mathbf{H} \parallel \langle 001\rangle$ and $\mathbf{H} \parallel \langle 110\rangle$. When it is parallel to the $\langle 111\rangle$ axis, it reduces to

$$\Delta F = A_3 H^3 m^3 \cos 3\varphi. \tag{6.15}$$

Equations (6.9), (6.12) and (6.15) lie at the heart of our results of this chapter. In the further subsections we will show how they interact with the order by disorder selection (6.6) and establish the $H - T$ phase diagrams of easy-plane pyrochlore.

Of course, symmetry analysis cannot predict the sign of the terms, which will be realised in the system, both are allowed by symmetry. Above in equations (6.9), (6.12) and (6.15) we chose an overall sign such that the selected states correspond to our numerical results for positive amplitudes A_6, A_2 and A_3. An overall minus sign is introduced in the order by disorder term (6.6) also to consider $A_6^{\mathrm{ObD}} > 0$.

6.1.1 $\mathbf{H} \parallel \langle 001\rangle$

The selection is especially simple when $\mathbf{H}$ is directed along the symmetry axes of the crystal. First, we consider the magnetic field directed along one of the main cubic axes $H_x = H_y = 0; H_z = H$. Then (6.12) takes the form

$$\Delta F^{[001]} = A_2 m^2 H^2 \cos 2\varphi \tag{6.16}$$

and favours states with $\varphi = \pi/2, 3\pi/2$. At $T = 0$ these $m_{x^2-y^2}$-like configurations are the ground states for any $0 < H < H_S$. At finite temperatures the situation is more complex because two competing degeneracy lifting terms (6.16) and (6.9) are present. At not very large T and H we can take $m = 1$ and explicitly extract linear temperature dependence in the prefactor of the order by disorder term

$$F = A_2 H^2 m^2 \cos 2\varphi - A_6^{\mathrm{ObD}} T m^6 \cos 6\varphi. \tag{6.17}$$

Simple minimisation of this equation then gives a set of minima

$$\begin{aligned}
H > H_C: &\qquad \varphi = \frac{\pi}{2} + \pi k;\\
H < H_C: &\qquad \varphi = \pm\frac{1}{2}\arccos\left(\frac{1}{2}\sqrt{1 + \frac{A_2 H^2}{3A_6^{\mathrm{ObD}} T}}\right) + \pi k;\\
&\qquad \varphi = \pi k \qquad \text{(local minima)}.
\end{aligned} \tag{6.18}$$

At the critical field $H_C = 3\sqrt{\frac{A_6^{\mathrm{ObD}} T}{A_2}}$ a second order phase transition occurs: each of the minima is split into two. The evolution of the lowest energy states with magnetic field at constant T is schematically presented in figure 6.2 (a).

The field-selection term is absent at $H = 0$, but for $H \to H_S$ prevails over order by disorder independently of T. Therefore, the ordered state undergoes a phase transition at any temperature, we show a sketch of the phase diagram in figure 6.2 (b). The expression for H_C, however, is valid only when both H and T are small. At higher T the behaviour of the critical field is more complex, we expect it to be nonmonotonic. Increase as $H \propto \sqrt{T}$ at low temperatures due to the onset of thermal order by disorder should be followed by the eventual drop to $H_C(T = T_N) = 0$. This drop at higher T should occur due to the decrease with temperature of m. Close to T_N the

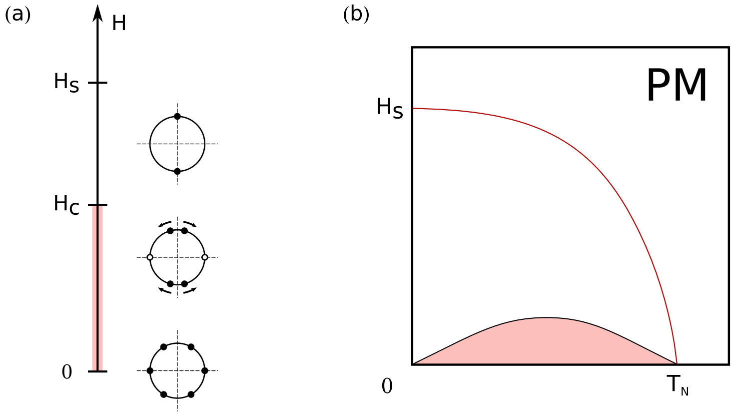

Figure 6.2: $\mathbf{H} \parallel \langle 001 \rangle$ (a) Field evolution of the antiferromagnetic structure in the presence of the zero-field anisotropy. Circles represent the manifold of degenerate ground states (6.2). Full (open) markers on them denote global (local) minima of the function (6.17). (b) Qualitative sketch of the phase diagram of the system in magnetic field. The red line denotes the transition from the paramagnetic to the antiferromagnetic phase with $\mathbf{Q} = 0$. The black line illustrates the new transition to the $m_{3z^2-r^2}$-like phase stabilized in the shaded region.

order parameter of the E irrep has a well known critical behaviour $m \propto (T - T_N)^{\beta}$. This results in $H_C(T) \propto (T - T_N)^{2\beta}$ at $T \to T_N$. It would be interesting to observe the nonmonotonic $H_C(T)$ experimentally.

6.1.2 $\mathbf{H} \parallel \langle 110 \rangle$

We pass on to the case of the magnetic field along the diagonal of the cubic face, we substitute $\mathbf{H} = (H, H, 0)/\sqrt{2}$ into (6.12) and obtain

$$\Delta F^{[110]} = -\frac{A_2}{2} m^2 H^2 \cos 2\varphi. \tag{6.19}$$

Therefore, the magnetic field along the [110] axis stabilises a pair of states with $\varphi = 0, \pi$. These are two of the six domains that belong to $m_{3z^2-r^2}$ state, which is selected by thermal fluctuations.

The minimisation analysis is unnecessary in this case because both terms favour the same states. So we conclude that at the $H - T$ phase diagram will have a single phase at all H and T, it is sketched in figure 6.3 (b). Upon decreasing H a two-domain state with $\varphi = 0, \pi$ evolves continuously into a state with $\varphi = 2\pi k/3$. At $H = 3\sqrt{\frac{2A_6^{\mathrm{ObD}}T}{A_2}}$ four local minima of free energy appear and gradually become deeper. However, they become true ground states only when $H = 0$. This evolution is presented in Fig. 6.3 (a).

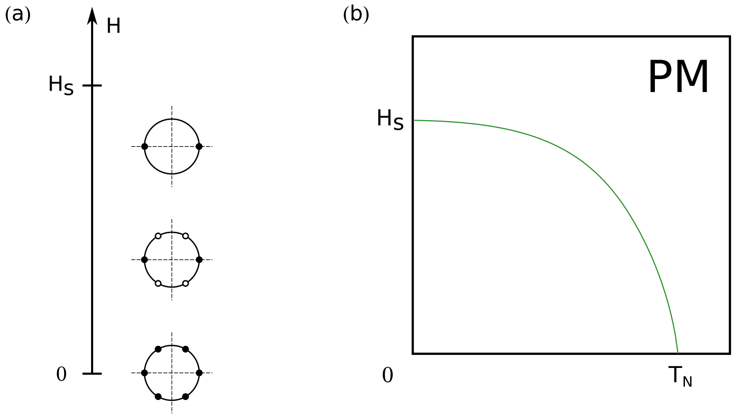

Figure 6.3: **H** $\parallel \langle 110 \rangle$ (a) Field evolution of the lowest energy states of the system in the presence of the zero-field anisotropy. (b) Sketch of the $H-T$ phase diagram with a single PM-AFM phase transition.

6.1.3 H $\parallel \langle 111 \rangle$

In this case the degeneracy lifting by the magnetic field is governed by two terms (6.9) and (6.15). Together with the correction from fluctuations (6.6) they give

$$F = A_3 H^3 m^3 \cos 3\varphi + A_6 H^2 m^6 \cos 6\varphi - A_6^{\mathrm{ObD}} T m^6 \cos 6\varphi. \tag{6.20}$$

Now the selection scheme is more complex and is governed by the ratio

$$\zeta = \frac{4m^3(A_6 H^2 - A_6^{\mathrm{ObD}} T)}{A_3 H^3}. \tag{6.21}$$

The parameter ζ depends on all selection strengths and at each T and H determines a configuration with the lowest free energy:

$$\begin{aligned} \zeta > 1: \qquad & \varphi = \pm\frac{1}{3}\arccos\left(-\zeta^{-1}\right) + \frac{2\pi k}{3}; \\ -1 < \zeta < 1: \qquad & \varphi = \frac{\pi}{3} + \frac{2\pi k}{3}; \\ \zeta < -1: \qquad & \varphi = \frac{\pi}{3} + \frac{2\pi k}{3}; \\ & \varphi = \frac{2\pi k}{3} \qquad \text{(local minima).} \end{aligned} \tag{6.22}$$

To illustrate these equations we consider several limiting cases.

1) When $H = 0$, lifting of the degeneracy happens only due to the order by disorder process, which selects six $m_{3z^2-r^2}$ states. It corresponds to $\zeta = -\infty$, where three local minima become global ones.

2) At the opposite limit of high magnetic field $H \to H_S$ the cubic term grows faster than quadratic one and may eventually become dominant. Then a configuration with three $m_{3z^2-r^2}$-like states is stabilised. It corresponds to $|\zeta|$ becoming small due to a rapidly growing denominator.

3) Finally, the second term in (6.20) is dominant when both H and T are small, it selects six $m_{x^2-y^2}$-like configurations. This case is equivalent to ζ being large and positive.

4) A limit of vanishing $T = 0$ when the selection by fluctuations is absent is also important. It

allows one to easily calculate the critical field $H_C = 4m^3 A_6/A_3$.

Figure 6.4 demonstrates the evolution of minima and a possible phase diagram of the system. We emphasise that differently with the previous schemes the transformation of states is shown as a function of ζ. Qualitatively different paths of evolution with H are shown by three broken lines. Like in the $\mathbf{H} \parallel \langle 001 \rangle$ case the new phase transition is of the Ising universality class as it is associated with splitting/merging of pairs of states.

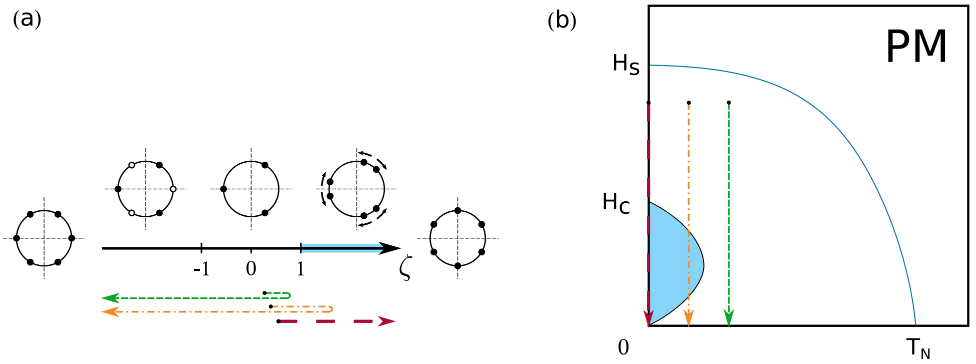

Figure 6.4: $\mathbf{H} \parallel \langle 111 \rangle$ (a) Magnetic structure of the system as a function of the dimensionless parameter $\zeta(H, T)$, defined in eq. (6.21). Three qualitatively different magnetisation processes are shown by three discontinuous lines below the scheme and on the phase diagram (the third line lies on top of the $T = 0$ axis.) (b) Sketch of the classical $H - T$ phase diagram with its main feature -the new $m_{x^2-y^2}$-like phase, located al low T and H.

6.1.4 $J_\perp^a > 4$ case

In the above analysis of phase transitions we considered only the case of $J_\perp^a < 4$, and hence of positive A_6^{ObD} in a prefactor of the fluctuation selection terms (6.6). This case is usually more relevant, due to the direct application to $\mathrm{Er_2Ti_2O_7}$ with is modelled by $J_\perp^a = 1.5$. In this subsection for the sake of completeness, we consider the opposite situation of $J_\perp^a > 4$ and briefly discuss the possible phases and transitions in this sector of parameter range.

First, we may assume that the sign of the field selection terms (6.9), (6.12) and (6.15) does not change as we vary the parameters of the Hamiltonian. Indeed, lifting of the ground state degeneracy by the external field should not be affected by internal couplings of the system. This assumption will be confirmed in the following section, where we derive selection terms in the limit of small H. On the contrary the sign of order by disorder correction (6.6) is reversed, as we saw in chapter 5.2.

Then the pictures for $\mathbf{H} \parallel \langle 001 \rangle$ and $\mathbf{H} \parallel \langle 110 \rangle$ cases at $A < 0$ are reversed. In the former case we predict no phase transition, but when the field is applied along the $\langle 110 \rangle$ direction, on the contrary, the system evolves from the zero field $m_{x^2-y^2}$ state to the configurations with $\varphi = 0, \pi$ via an Ising phase transition at all $T > 0$.

For $\mathbf{H} \parallel \langle 111 \rangle$ two last terms in (6.20) favour the same $m_{x^2-y^2}$ state. Therefore, the situation is significantly simplified: for any $T \geq 0$ there is a competition between the $m_{x^2-y^2}$ phase, stabilised at low magnetic field and the $m_{3z^2-r^2}$-like configuration with three minima at $\varphi = \pi/3 + 2\pi k/3$.

This suggests a field evolution via a single Ising phase transition at all temperatures, and the phase diagram similar to the one, presented on Fig. 6.2 (b).

6.2 Low-H perturbative calculations for the field induced anisotropies

In this section analytic expressions for field selection anisotropy will be obtained in the limit of small H. We treat the Zeeman term in the Hamiltonian as a linear perturbation to the ground state and minimise the energy with respect to it. The obtained energy corrections will be treated as field-induced anisotropic terms in the Hamiltonian. The expressions for the degeneracy lifting terms for three different directions of magnetic field will constitute the main result of this section. Also, in subsection 6.2.5 we show that these expressions are in perfect quantitative agreement with the numerical energy minimisation results.

We follow the steps of the real space perturbation theory, developed for pyrochlores in the previous chapter and consider the Hamiltonian, written in the form (5.12)

$$\hat{\mathcal{H}} = \sum_{\langle ij\rangle}\big[h_{ij}S_i^zS_j^z - M_{ij}S_i^xS_j^x - K_{ij}(S_i^xS_j^z + S_i^zS_j^x)\big] - \sum_i g_{\alpha\beta}H_i^\alpha S_i^\beta. \tag{6.23}$$

This Hamiltonian is obtained as a result of coordinate transform from the usual frame, defined by (5.2) and (5.8) to the local frame, where $\hat{\mathbf{z}}_i$ denotes a quantisation axis for a particular ground state, labelled by φ. In equation (6.23) h_{ij}, M_{ij}, and K_{ij} are coupling constants, which explicitly depend on the angle φ:

$$\begin{aligned}
h_{ij} &= -\frac{1}{6}(2J_\perp + J_\perp^a) + \frac{1}{6}(4J_\perp - J_\perp^a)\cos(2\varphi + \gamma_{ij}),\\
K_{ij} &= \frac{1}{6}(4J_\perp - J_\perp^a)\sin(2\varphi + \gamma_{ij}),\\
M_{ij} &= \frac{1}{6}(2J_\perp + J_\perp^a) + \frac{1}{6}(4J_\perp - J_\perp^a)\cos(2\varphi + \gamma_{ij}),\\
h &= \sum_{i=1}^{6} h_{ij} = (2J_\perp + J_\perp^a)\,S,
\end{aligned} \tag{6.24}$$

and on the bond-dependent phase angles

$$\gamma_{12} = \gamma_{34} = 0\,, \qquad \gamma_{13} = \gamma_{24} = \frac{2\pi}{3}\,, \qquad \gamma_{14} = \gamma_{23} = -\frac{2\pi}{3}\,. \tag{6.25}$$

We consider the g tensor in the last term of (6.23) to be diagonal in the local basis with components $g = \{g^\perp, g^y, g^\perp\}$. We denote by ξ_i the angle that the in-plane component of magnetic field constitutes with the original $\hat{\mathbf{x}}$ axis (5.8). Then in the transformed frame the Zeeman term is written as

$$\hat{\mathcal{H}}_Z = -\sum_i \Big[g^yH_i^yS_i^y + g^\perp H_i^\perp\left(S_i^x\sin(\varphi - \xi_i) + S_i^z\cos(\varphi - \xi_i)\right)\Big]\,. \tag{6.26}$$

Below we provide explicit values of in-plane field component $H^{\perp} = \sqrt{H^2 - H^{y2}}$ and polar angle ξ for three distinct directions of magnetic field in the specific coordinate frame, defined by (5.8):

$$\begin{array}{lll}
H \ \| \ [001] & H \ \| \ [110] & H \ \| \ [111] \\
H_1^{\perp} = \sqrt{\frac{2}{3}} H; \quad \xi_1 = \pi; & H_1^{\perp} = \frac{1}{\sqrt{3}} H; \quad \xi_1 = 0; & H_1^{\perp} = 0; \\
H_2^{\perp} = \sqrt{\frac{2}{3}} H; \quad \xi_2 = \pi; & H_2^{\perp} = \frac{1}{\sqrt{3}} H; \quad \xi_2 = \pi; & H_2^{\perp} = \frac{\sqrt{8}}{3} H; \quad \xi_2 = \pi; \\
H_3^{\perp} = \sqrt{\frac{2}{3}} H; \quad \xi_3 = 0; & H_3^{\perp} = H; \qquad \xi_3 = -\pi/2; & H_3^{\perp} = \frac{\sqrt{8}}{3} H; \quad \xi_3 = -\pi/3; \\
H_4^{\perp} = \sqrt{\frac{2}{3}} H; \quad \xi_4 = 0; & H_4^{\perp} = H; \qquad \xi_4 = \pi/2; & H_4^{\perp} = \frac{\sqrt{8}}{3} H; \quad \xi_4 = \pi/3.
\end{array} \tag{6.27}$$

6.2.1 Minimisation procedure

We start from the ground state, parameterised by a fixed value of angle φ and introduce a weak magnetic field $H \ll J_{\perp};\ J_{\perp}^{a}$. This field will generate a distortion of the system through nonzero but small S_i^x and S_i^y. As before, we can expand $S_i^z \simeq S - \frac{S^{x2}}{2S} - \frac{S^{y2}}{2S}$. Substituting this into equations (6.23) and (6.26) and keeping only quadratic in fluctuations terms, we get:

$$\hat{\mathcal{H}} = \frac{h}{2S} \sum_i \left[S_i^{x2} + S_i^{y2}\right] - \sum_{\langle ij \rangle} M_{ij} S_i^x S_j^x - g^y \sum_i H_i^y S_i^y - g^{\perp} \sum_i H_i^{\perp} S_i^x \sin(\varphi - \xi_i). \tag{6.28}$$

In what follows, we find a new minimum of energy in the limit of small distortions and obtain the correction to ground state energy for each value of parameter φ.

First, we deal with the out of plane part of the Hamiltonian. It is diagonal in spins, therefore straightforward minimisation gives

$$\Delta E_Z^y = -\frac{S(g^y)^2}{2h} \sum_i H_i^{y2} = -\frac{2}{3} \frac{(g^y H)^2 N}{(2J_{\perp} + J_{\perp}^{a})}. \tag{6.29}$$

This correction is constant for all ground states and all directions of external magnetic field.

Minimisation over the in-plane fluctuation part is more involved due to the presence of interaction terms. The ordered ground state (6.2) is a $\mathbf{Q} = 0$ spin structure. Then the whole lattice is described by a single unit cell with four spins $i, j = 1, \ldots 4$, and the quadratic form reduces to a 4 by 4 matrix. In order to compensate for the reduction of the number of the neighbours of each spin, we double the magnitude of off-diagonal interaction terms in (6.28), the local field felt by each of the four spins is of course left the same $h = (2J_{\perp} + J_{\perp}^{a})S$. Due to the properties of phase angles (6.25) the matrix of the quadratic form M has a highly symmetric structure:

$$M = -\begin{pmatrix} -h/(2S) & M_{12} & M_{13} & M_{14} \\ M_{12} & -h/(2S) & M_{14} & M_{13} \\ M_{13} & M_{14} & -h/(2S) & M_{12} \\ M_{14} & M_{13} & M_{12} & -h/(2S) \end{pmatrix} \tag{6.30}$$

and is relatively easy to diagonalise. The eigenmodes $\Lambda = \frac{1}{3}\mathrm{diag}\{\lambda_1;\lambda_2;\lambda_3;\lambda_4\}$ are calculated by $\Lambda = T^{-1}MT$, where T - is the suitable orthogonal transformation matrix

$$T = \frac{1}{2}\begin{pmatrix} -1 & -1 & 1 & 1 \\ -1 & 1 & -1 & 1 \\ 1 & -1 & -1 & 1 \\ 1 & 1 & 1 & 1 \end{pmatrix}. \tag{6.31}$$

We obtain the following set of eigenmodes

$$\begin{aligned} \lambda_1 &= 2(2J_\perp + J_\perp^a) - (4J_\perp - J_\perp^a)\cos(2\varphi + \gamma_{12}), \\ \lambda_2 &= 2(2J_\perp + J_\perp^a) - (4J_\perp - J_\perp^a)\cos(2\varphi + \gamma_{13}), \\ \lambda_3 &= 2(2J_\perp + J_\perp^a) - (4J_\perp - J_\perp^a)\cos(2\varphi + \gamma_{14}), \\ \lambda_4 &= 0. \end{aligned} \tag{6.32}$$

The zero energy mode λ_4 corresponds to the transformation of the spin state within the degenerate manifold, it does not contribute to the lifting of the ground state degeneracy.

$$\hat{\mathcal{H}} = \sum_{i=1}^{3} \lambda_i \sigma_i^2 - g^\perp \sum_{i,j=1}^{4} H_j^\perp \sin(\varphi - \xi_j) t_{ji} \sigma_i. \tag{6.33}$$

The correction to the ground state energy is then obtained by direct minimisation of this diagonal Hamiltonian

$$\Delta E_Z^\perp = -\frac{(g^\perp)^2}{4}\frac{N}{4}\sum_{i=1}^{3} \frac{\left(\sum_{j=1}^{4} H_j^\perp \sin(\varphi - \xi_j) t_{ji}\right)^2}{\lambda_i}. \tag{6.34}$$

Introducing a normalisation factor $N/4$, we extend the result to the full lattice. In the following subsections we present the results for the three interesting field directions by substituting corresponding projections of H (6.27) and performing simple trigonometric calculations.

6.2.2 H $\parallel$ $\langle 001 \rangle$ result

When the applied field is parallel to one of the crystallographic axes, only one term, containing λ_1 in the sum (6.34) will be not zero and the energy correction has a simple form

$$\Delta E_Z^\perp = \frac{(g^\perp H)^2 N}{8(2J_\perp + J_\perp^a)}\, \frac{\cos 2\varphi - 1}{1 - \varepsilon\cos 2\varphi}, \tag{6.35}$$

where we introduced a dimensionless model parameter $\varepsilon = \frac{4J_\perp - J_\perp^a}{4J_\perp + 2J_\perp^a} = \frac{J_{\pm\pm}}{2J_\pm}$. In the parameter region, spanned by positive $J_\perp$ and $J_\perp^a$, it varies inside $-0.5 < \varepsilon < 1$. More generally, the ground state of the model belongs to E irrep when $-1 < \varepsilon < 1$ [82]. Therefore, for all relevant ε the denominator of (6.35) stays strictly positive, and the state selection is governed by $\Delta E_Z^\perp \sim H^2 \cos 2\varphi$.

By minimising the Hamiltonian of a pyrochlore in small magnetic field, we recovered the result of the Landau symmetry analysis of the previous section (6.16). The magnetic field along the [001] axis selects two $m_{x^2-y^2}$ - like states with $\varphi = 0, \pi$. Moreover, taking the Fourier integral, one can obtain the expression for the amplitude of the leading harmonic, in the limit of weak magnetic field. In (6.16) it was denoted as A_2:

$$A_2 = \frac{(g^{\perp}H)^2 N}{4(2J_{\perp} + J^a_{\perp})} \frac{1}{1 + \varepsilon + \sqrt{\frac{1+\varepsilon}{1-\varepsilon}}}. \tag{6.36}$$

Finally, comparison with the numerical results suggests that the quadratic correction to energy (6.35) is valid within 5% of accuracy up to $H_{\text{lim}} \simeq 0.8J_{\perp}$ (see section 6.2.5 for more details).

6.2.3 $\mathbf{H} \parallel \langle 110 \rangle$ result

For $\mathbf{H} \parallel \langle 110 \rangle$ two other eigenmodes λ_2 and λ_3 contribute to the energy shift. Using the same notations, as in the previous case we obtain

$$\Delta E^{\perp}_{Z} = -\frac{(g^{\perp}H)^2 N}{16(2J_{\perp} + J^a_{\perp})} \frac{2 - \frac{\varepsilon}{2} + (\varepsilon + 1)\cos 2\varphi + \varepsilon \cos 4\varphi}{1 - \frac{\varepsilon^2}{4} + \varepsilon \cos 2\varphi + \frac{\varepsilon^2}{2}\cos 4\varphi}. \tag{6.37}$$

The form of the correction is now more complex, the magnetic field explicitly generates two different harmonics $\cos 2\varphi$ and $\cos 4\varphi$. However, one can still proceed with the same analysis as in the previous subsection and see that i) denominator is again finite and positive ii) $\varphi = \pi/2, 3\pi/2$ states have the minimal energy iii) the corresponding $\cos 2\varphi$ harmonic has an amplitude $-A_2/2$ from eq. (6.36). These facts are clear for $\varepsilon = 0$ but also hold for any $-1 < \varepsilon < 1$. The most striking is the correspondence of Fourier harmonics of $\mathbf{H} \parallel \langle 110 \rangle$ and $\mathbf{H} \parallel \langle 001 \rangle$ cases up to a factor $-1/2$ in complete agreement with the symmetry analysis of the previous subsection.

6.2.4 $\mathbf{H} \parallel \langle 111 \rangle$ result

Now the energy correction equals to

$$\Delta E^{\perp}_{Z} = \frac{(g^{\perp}H)^2 N}{8(2J_{\perp} + J^a_{\perp})} \frac{-4 + 2\varepsilon + \varepsilon^2 + \varepsilon^2 \cos 6\varphi}{1 - \frac{3\varepsilon^2}{4} - \frac{\varepsilon^3}{4}\cos 6\varphi}. \tag{6.38}$$

Like before the denominator is always positive. The selection term is proportional to $\cos 6\varphi$ with a nonnegative coefficient. This correction is minimal for the $m_{x^2-y^2}$-like states, characterised by $\varphi = \frac{\pi}{6} + \frac{\pi}{3}k$. Note that ground state-dependent terms vanish at $J^a_{\perp} = 4$ ($\varepsilon = 0$), where the rotational $U(1)$ symmetry becomes exact for the Hamiltonian, and the magnetic field $\mathbf{H} \parallel \langle 111 \rangle$ does not break it.

Equation (6.38) partially confirms the results of section 6.1.3, specifically, the equation (6.9). The second invariant (6.15) is not present here because we considered only the leading $O(H^2)$ correction to energy. Our numerical minimisation, however, suggests that it will give a significant 5% contribution starting from $H_{\text{lim}} \simeq 0.4J_{\perp}$. Thus the validity of $\Delta E^{\perp}_{Z}$ for $\mathbf{H} \parallel \langle 111 \rangle$ is somewhat reduced, compared to the $\mathbf{H} \parallel \langle 001 \rangle$ case. More details on numerical check of formulas (6.35) and (6.38) will be given in the following subsection.

6.2.5 Numerical minimisation

We used the deterministic algorithm of searching the ground state of the classical system, which was presented in section 3.3 of this work. It consists of iterative minimisation of energy of each spin by setting

$$\mathbf{S}_i \parallel \mathbf{h}_i^{\text{loc}}; \qquad \mathbf{h}_i^{\text{loc}} = \sum_{j=1}^{6} \left[J_\perp \mathbf{S}_j^\perp + J_\perp^a (\mathbf{S}_j^\perp \cdot \hat{\mathbf{r}}_{ij})\hat{\mathbf{r}}_{ij} \right]^\perp - g^\parallel H^\parallel \hat{\mathbf{z}}_i - g^\perp \mathbf{H}^\perp, \tag{6.39}$$

where $\hat{\mathbf{z}}_i$ - is a local trigonal axis for site i, and the sum runs over six neighbours of the site i. The procedure was repeated until convergence for 500 different random initial spin configurations, and a global minimum was determined for each value and direction of the magnetic field. We checked that with periodic boundary conditions the size of the cluster does not play any role, which is the consequence of the studied $\mathbf{Q} = 0$ spin structure, so we took $L = 1$. This protocol corresponds to the search for the ground state of the system at $T = 0$. The obtained sequence of ordered phases for all three cases corresponds to the $T = 0$ analysis of section 6.1.

To allow for the quantitative comparison of our analytical results we modified the numerical algorithm to get an estimate of the angular dependence of $\Delta E_Z(\varphi)$. We minimised the energy (6.39) for the spins on three out of four sublattices, while fixing the azimuthal angle φ_1 and the out of plane component S_1^z of the spin on the first sublattice. Then we swept through all S_1^z and chose the global minimum of energy $E(\varphi, H)$.

At low H these results can be compared with the energy corrections ΔE_Z^y and $\Delta E_Z^\perp$, calculated above in equations (6.29), (6.35), (6.37) and (6.38). In figure 6.5 we present the comparison of analytically (solid lines) and numerically (symbols) calculated correction $\Delta E_Z = \Delta E_Z^y + \Delta E_Z^\perp$ for $H = 3.47 \cdot 10^{-3} J_\perp$ and for three different field directions.

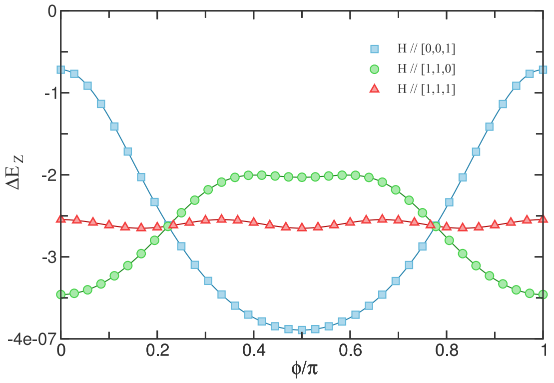

Figure 6.5: Field induced correction to energy, for the whole degenerate manifold of states, calculated analytically (solid lines) in eq. (6.29) (6.35), (6.37) and (6.38) and numerically (symbols) using the minimisation procedure. The set of parameters, relevant to $Er_2Ti_2O_7$ is used in the numerics: $J_\perp = 1$, $J_\perp^a = 1.5$, $g^\perp = 1$, $g^\parallel = 0.5$. The magnetic field is set $H = 3.47 \cdot 10^{-3} J_\perp$.

While Fig. 6.5 evidences the correctness of our analytics at low H, this numerical method can be also used to estimate the applicability limits of the calculations of this section at higher magnetic fields. We found that for the $\mathbf{H} \parallel [001]$ case our low-field minimisation procedure gives a 5% accuracy result up to $H_{\text{lim}} \simeq 0.8 J_\perp$. As we will show in the following section, the phase transition in the classical model occurs at $H \simeq 0.15 J_\perp$ (figure 6.6), which is well below H_{lim}

This is a promising result, as it allows to describe the effects of the magnetic field at the phase transition not only in the classical case, but also very likely in the real system (see section 6.4 for more details on quantum effects on the phase transitions). In the second interesting case of $\mathbf{H} \parallel [111]$ the 5% accuracy of equation (6.38) is reached at somewhat lower $H_{\text{lim}} \simeq 0.4J_\perp$. It happens due to the emergence of $\cos 3\varphi$ harmonic (6.15), which vanishes at low field as H^3, and therefore is not present in the quadratic correction to energy (6.38).

Also, it is interesting to note that in our numerical results we recovered the change of sign of the fourth harmonic term with ε (6.37). While the second harmonic stays always negative, the prefactor of $\cos 4\varphi$ term becomes positive for $J_\perp^a > 4J_\perp$. It can modify the simple two domain structure with $\varphi = 0, \pi$, predicted in section 6.1.4. Indeed, a more complex ground state was observed at some parameter range in our simulations.

6.3 Finite temperature Monte Carlo studies

To study the properties of the system at finite temperatures we performed Monte Carlo simulations. The general algorithm was described in section 3.1, below we present some details, relevant for the particular model.

A measurement was made after five consecutive Metropolis MCS, followed by five microcanonical overrelaxation sweeps of the cubic lattice with $N = 4L^3$ spins, $L \leq 24$. Most of the Monte Carlo runs were performed at fixed T, starting from a random spin configuration at high field $H > H_S$ and moving down to the lower fields. In this study we used more independent runs than usual to sample the phase space better, as for higher fields the algorithm exploded a small area of phase space in the vicinity of one global minimum. Each point on a figure is a statistical average over 96 independent runs, during each run measurements were taken during up to $2 \cdot 10^5$ MCS, and first $5 \cdot 10^4$ MCS were omitted for thermalisation. A total number of MCS was higher for larger clusters.

In our runs we measured several order parameters. First, m, the order parameter of E irrep was used to determine the PM-AFM transition.

$$m = \sqrt{m_x^2 + m_y^2}, \qquad m_x = \frac{1}{N}\sum_i \mathbf{S}_i \cdot \hat{\mathbf{x}}_n, \qquad m_y = \frac{1}{N}\sum_i \mathbf{S}_i \cdot \hat{\mathbf{y}}_n. \tag{6.40}$$

To answer the question of lifting the continuous degeneracy within the E manifold, we measured a series of Potts-like order parameters $M_k^{'}$ and $M_k^{''}$ with $k = 2, 3, 4, 6$:

$$M_k^{'} = \frac{1}{m^{k-1}}\text{Re}\{(m_x + im_y)^k\} = m\cos k\varphi; \tag{6.41}$$

$$M_k^{''} = \frac{1}{m^{k-1}}\text{Im}\{(m_x + im_y)^k\} = m\sin k\varphi \tag{6.42}$$

and corresponding Binder cumulants

$$U(M_k) = 1 - \frac{\langle M_k^4 \rangle}{3\langle M_k^2 \rangle^2}. \tag{6.43}$$

First, we present the results for the case of the magnetic field parallel to one of the main crystallographic axis $\mathbf{H} \parallel [001]$. The results are summarised in the figure 6.6 (a). For each field sweep we first observed a PM-AFM second order phase transition, followed by another

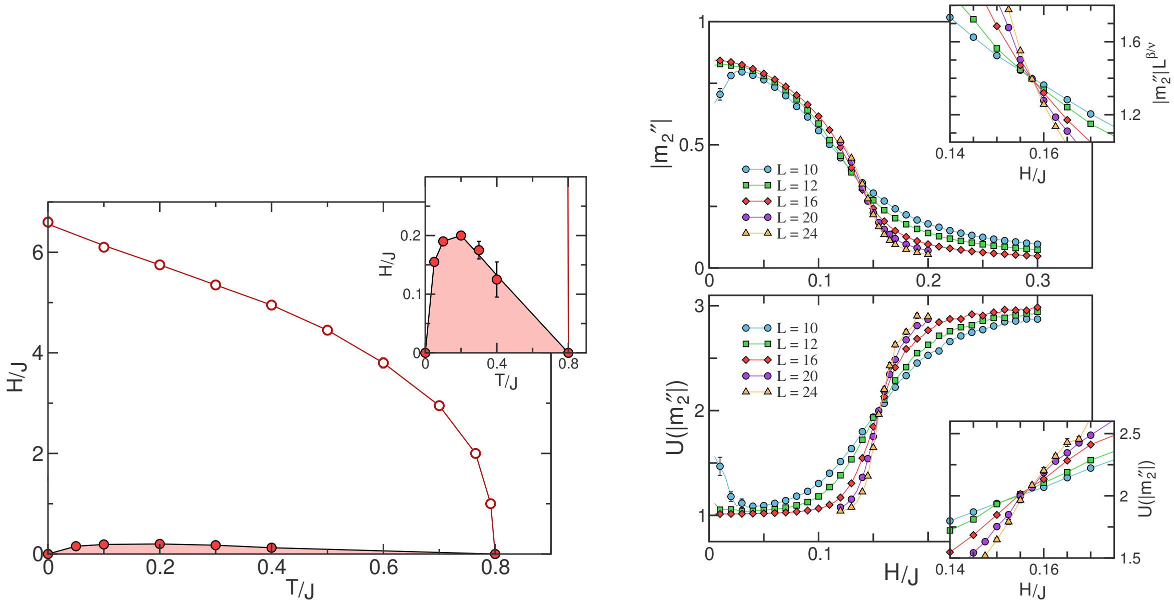

(a) Monte Carlo $H-T$ phase diagram of the easy-plane pyrochlore. The parameters of simulations are chosen to represent $Er_2Ti_2O_7$: $J_\perp^a = 1.5J_\perp, g^\perp = 1, g^z = 0.5$. The red line denotes the PM-AFM phase boundary, while the black line denotes the transition to the low-H $m_{3z^2-r^2}$-like antiferromagnetic phase (shaded region). The inset shows a zoom to the low-field region.

(b) Finite size analysis for $T = 0.05J_\perp$. Top panel: inverse scaling of the order parameter $|M_2''|$. The inset shows a procedure of β/ν ratio determination. The best crossing was observed for $\beta/\nu = 0.70(5)$. Bottom panel: crossing of Binder cumulants defines the transition field $H_C = 0.156(2)J_\perp$, and the inset shows the zoom into the intersection area .

Figure 6.6: Monte Carlo results for the $\mathbf{H} \parallel [001]$ case.

second order transition at $H = H_C$ well inside the AFM phase. We concentrate on the latter transition, and show the example of the finite size analysis $T = 0.05J_\perp$ with $|M_2''|$ as a primary order parameter on panel (b) of Fig. 6.6. Critical field $H_C = 0.156(2)J_\perp$ was determined by the crossing of the Binder cumulants $U(|M_2''|)$ (bottom panel). Also, rough estimates of the critical exponents η and β/ν were obtained by the simple protocol, described in the last paragraph of section 3.2.1. The best crossing was achieved when $\beta/\nu = 0.70(5)$ and $\eta = 0.40(5)$ respectively. The abscissa of the crossing point gives $H_C = 0.157(2)J_\perp$, consistent with the value, obtained from Binder functions. The example of the scaling procedure is shown in the inset of figure 6.6 (a).

Finally, we note that at higher temperatures the system is subject to strong finite size effects. We did not observe a single intersection of $U(|M_2''|)$ lines even for the largest clusters, this is depicted by larger error bars at $T \geq 0.3J_\perp$ on the phase diagram. This extremely slow convergence of $U(|M_2''|)$ and inverse scaling of the order parameter $|M_2''|$ (Fig. 6.6 (a)) - another peculiar scaling behaviour - is caused by the dangerous irrelevance of the $\mathbb{Z}_6$ anisotropy, which drives this phase transition. For further details see [70] and reference therein.

We repeated all procedures for the other case of $\mathbf{H} \parallel [111]$, and present the results in figure 6.7 (a). Now the lower phase transition occurs only in the region of small $T \leq 0.1J_\perp$ and $H \leq 1.5J_\perp$ and is traced by nonzero $|M_3''|$. The same finite size analysis, as in the previous case, was carried out, the main features of it are shown in figure 6.7 (b). Now we have to investigate two phase transitions. However, we were able to precisely study only the upper one due to very strong

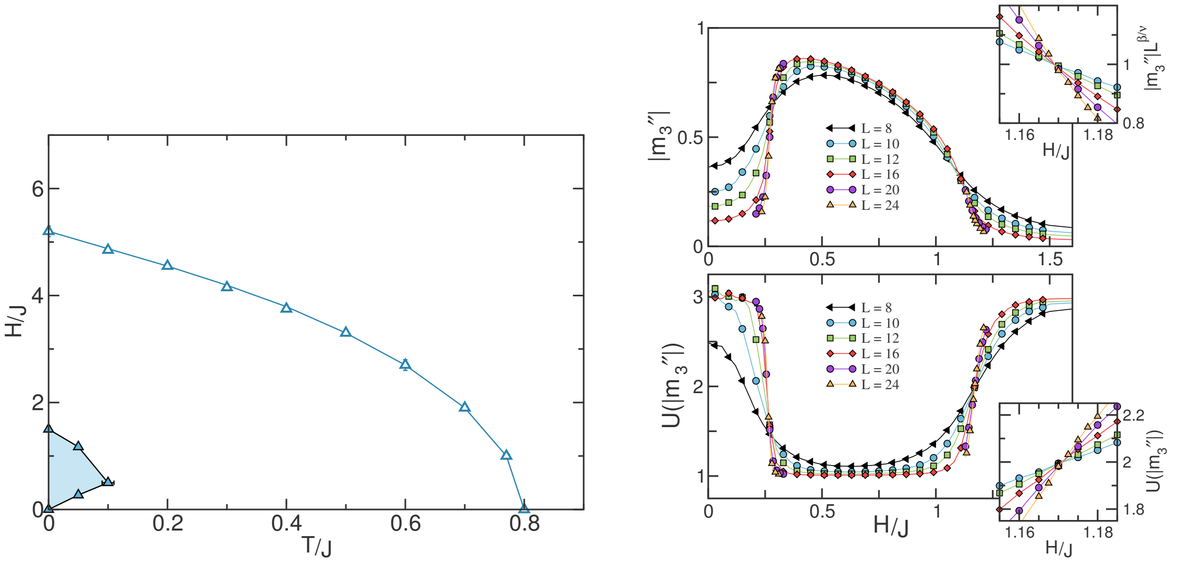

(a) Monte Carlo $H-T$ phase diagram of the classical easy-plane pyrochlore, all lines are guides for the eye. Shaded area represents the new $m_{x^2-y^2}$-like phase induced by the magnetic field. The parameters of simulations are chosen to represent $Er_2Ti_2O_7$: $J^a_\perp = 1.5J_\perp, g^\perp = 1, g^z = 0.5$. The blue line represents the PM – AFM phase boundary, while the black line represents the transition between different $\mathbf{Q} = 0$ phases.

(b) Finite size analysis for $T = 0.05J_\perp$. Top panel: inverse scaling of the order parameter $|M''_3|$. The inset shows a procedure of β/ν ratio determination. The best crossing was observed for $\beta/\nu = 0.65(5)$. Bottom panel: crossings of Binder cumulants define transition fields $H_{C1} = 0.27(1)J_\perp$ and $H_{C2} = 1.171(3)J_\perp$. The inset is a the zoom into the area around H_{C2}.

Figure 6.7: Monte Carlo results for the $\mathbf{H} \parallel \langle 111 \rangle$ case.

autocorrelation effects at lower transition. Much longer simulation time is needed to reduce the noise in the fourth order Binder cumulants $U_B(|M''_3|)$ at low T and H. The critical properties of the upper transition are governed by $\beta/\nu = 0.65(5)$ and $\eta = 0.35(5)$.

The inner phase transitions for both $\mathbf{H} \parallel [001]$ and $\mathbf{H} \parallel [111]$ are expected to belong to the $3D$ Ising universality class. They are associated with the splitting or merging of several pairs of minima. In the former case a two-domain structure with $\varphi = \pi/2, 3\pi/2$ transforms into a configuration with four domains. In the latter, three minima with $\varphi = \pi/3, \pi, 5\pi/3$ continuously evolve into six $m_{x^2-y^2}$-like states and backwards upon decreasing the strength of magnetic field. $3D$ Ising transitions critical exponents are known with high precision: $\beta/\nu = 0.5181(8)$ and $\eta = 0.0364(5)$. It is clear that our values for the critical indices are significantly higher than the benchmark ones. Nevertheless, we do not think that the transitions belong to the new universality class. The more probable scenario is the effect of a dangerously irrelevant $\mathbb{Z}_6$-like local field [70].

Finally, the same simulations were performed for the third case $\mathbf{H} \parallel [110]$. And no sign of additional phase transition was seen at any T and H. This agrees well with the theoretical prediction of section 6.1.2: a configuration with $\varphi = 0, \pi$, selected by H transforms smoothly into the $m_{3z^2-r^2}$ ordered structure at $H = 0$. This rather trivial phase diagram is shown in Fig. 6.8.

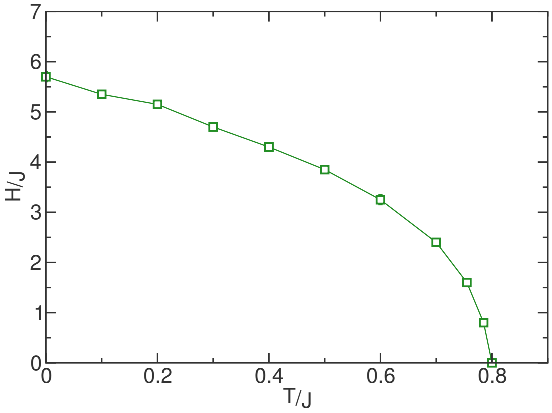

Figure 6.8: Monte Carlo phase diagram for $\mathbf{H} \parallel \langle 110\rangle$ with only one paramagnetic-antiferromagnetic second order phase boundary. Four domains of the $m_{3z^2-r^2}$ phase are energetically unfavourable when $H > 0$, so there is no symmetry breaking at finite field.

Before moving on, we note that when we set $\mathbf{H} \parallel [001]$ and $\mathbf{H} \parallel [110]$, the observed PM-AFM transition was always of the second order. On the contrary for $\mathbf{H} \parallel [111]$ the transition should be of the first order, as it is driven by the cubic invariant (6.15). However, even $T \to 0$ the observed discontinuity in magnetisation or the order parameter was very small. At temperatures, higher than $T \gtrsim 0.2J_\perp$, the system evolved through a crossover, rather than a sharp first order transition.

6.3.1 Monte Carlo and distribution functions

To illustrate the phase transitions and the evolution of the ordered states we measured probability distribution functions of states $\rho(\varphi)$ at different T and H. Starting at a random initial spin state in the paramagnetic region, we decreased the temperature at fixed H, equilibrating the system at each step using the same Monte Carlo procedure, as described earlier in this section. Upon reaching the desired T, we took the snapshots of the system, every 50 MSC, measuring m_x and m_y (see eq. (6.40)) and calculating the angle φ:

$$\varphi = \operatorname{sign}(m_y) \arccos\left(\frac{m_x}{m}\right). \tag{6.44}$$

The whole procedure was repeated 2400 times, each starting from a new initial configuration, making a total of 10^5 snapshots.

Subsequently we plot the histogram for the ordering angle φ, which is a measure of the angle distribution function $\rho(\varphi)$. Panels (a) of figures 6.9 and 6.10 show $\rho(\varphi|H)$ for the two interesting cases at $T = 0.05$. Each line corresponds to a star symbol of the same colour on a phase diagram (panels (b)). The splitting and merging of minima as well as the emergence of local minima at low fields is clearly visible for both field directions. This data strongly supports our picture of Ising phase transitions in anisotropic pyrochlore in a field.

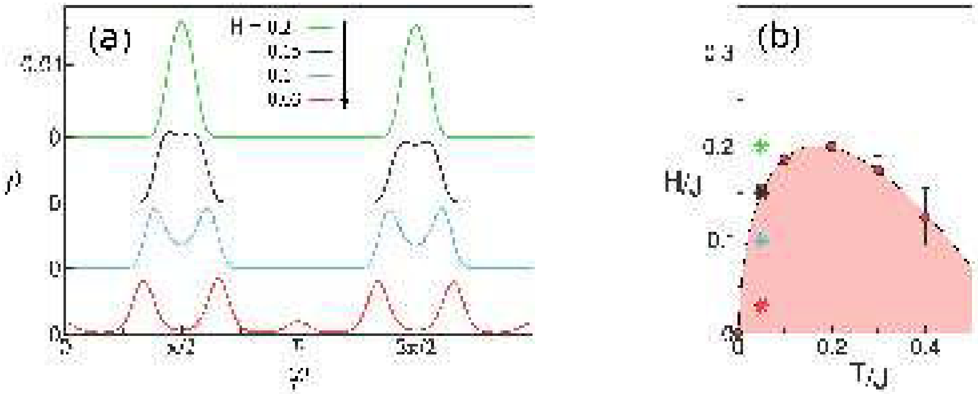

Figure 6.9: (a) Probability distribution of states with different angle φ for different values of H. All measurements are made at $\mathbf{H} \parallel [001]$ and $T = 0.05J_\perp$. Curves for different H are plotted with the uniform offset. (b) Low H part of the MC phase diagram. Star markers correspond to the $\rho(\varphi)$ curves on the panel (a), round markers are results of MC simulations.

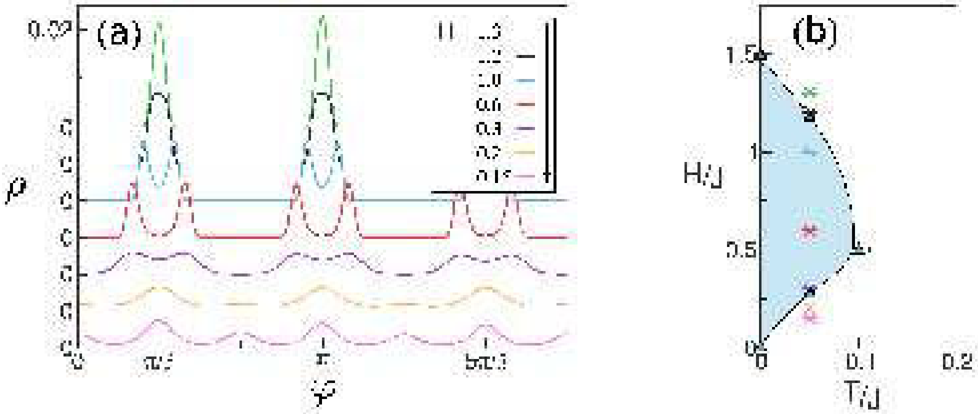

Figure 6.10: (a) Probability distribution of states with different angle φ for different H. All measurements are made at $\mathbf{H} \parallel [111]$ and $T = 0.05J_\perp$. Curves for different H are plotted with the uniform offset. (b) Low H, low T part of the MC phase diagram. Star markers correspond to the $\rho(\varphi)$ curves on the panel (a), round markers are results of MC simulations.

6.4 Quantum effects and observation perspectives

In the previous sections we predicted the phase diagrams of the purely classical model (6.25). In this section we study how quantum effects modify our predictions. For the easy-plane pyrochlore we calculated quantum effects in the framework of real space perturbation theory in section 5.2.1 of the previous chapter. Strictly speaking, those results are valid for the $H = 0$ case only, but we expect them to give a good estimate of quantum effects also when H is small.

Zero point fluctuations give rise to an effective anisotropy term of the form $\Delta E_Q = -\gamma_6 \cos 6\varphi$ with positive γ_6, it selects one of the six ψ_2 states from the E manifold even at $T = 0$ [6, 7]. The expression for the sixfold anisotropy for $S = 1/2$ is given in equation (5.20):

$$\Delta E = -\frac{\kappa^3 N}{16^3 S}\left(1 - \frac{\kappa^2}{4}\right)\cos 6\varphi \tag{6.45}$$

The effect of quantum fluctuations has essentially the same form as thermal order by disorder. Therefore, it effectively enhances the $-\cos 6\varphi$ anisotropy by a constant factor. In the following, two subsections we study the effect of this correction for two field directions. For $\mathbf{H} \parallel \langle 001\rangle$ we estimate the shift of the phase transition boundary. And for the field along the trigonal axis $\mathbf{H} \parallel \langle 111\rangle$ we the existence of a $m_{x^2-y^2}$ phase is discussed. We note that for the third case $\mathbf{H} \parallel \langle 110\rangle$ inclusion of quantum effects does not significantly modify the behaviour of the system under applied field.

6.4.1 Phase transition shift for $\mathbf{H} \parallel \langle 001\rangle$

Quantum zero point fluctuations produce a $-\cos 6\varphi$ term (6.45), which results in a shift of the phase transition boundary. The expression for H_C was obtained in section 6.1.1:

$$H_C = 3\sqrt{\frac{A_6^{\mathrm{Th}}T + A_6^{\mathrm{Q}}}{A_2}}. \tag{6.46}$$

The shift due to A_6^Q is present at all $0 \le T < T_N$, it is especially interesting to estimate the new value for H_C at $T = 0$. Then we substitute values for amplitudes from (6.36) and (6.45) and obtain for the parameters, relevant for $\mathrm{Er_2Ti_2O_7}$: $J_\perp^a = 1.5J_\perp$, $g^\perp = 1$, $\varepsilon = 5/14$ and $S = 1/2$ that $H_C(0) = 0.24(1)J_\perp$. Note that this fairly small shift of H_C legalises the employed quadratic approximation of the field-induced anisotropy. The estimate is still rather crude mainly because of the difficulty of calculation of quantum effects, even at $H = 0$.

Equation (6.46) can be also treated the other way round: once the experimental value of $H_C(0)$ is obtained, one can calculate the magnitude of the order by disorder effect. In this sense it is an alternative to the spin-wave gap measurements that were done recently by Ross *et al.* [73].

6.4.2 Existence of phase transition for $\mathbf{H} \parallel \langle 111\rangle$

Contrary to the previous case, for $\mathbf{H} \parallel \langle 111\rangle$ quantum fluctuations act against the nontrivial phase stabilised by the magnetic field. It may happen that the $m_{x^2-y^2}$-like phase gets completely suppressed in a real system. Below we obtain a critical value of the amplitude $A_{6\,\mathrm{crit}}^{\mathrm{Q}}$ of the quantum order by disorder term, which still let the additional second order transition. After that we will compare it with the prefactor in equation (6.45).

To explain the suppression of the $m_{x^2-y^2}$-like phase at high magnetic field, both invariants (6.9) and (6.15) are necessary. Unfortunately, the quadratic approximation of section 6.2 gives us analytic expression only for the first term. So we use our angular-resolved minimisation algorithm (sec. 6.2.5) and obtain the amplitude of $\cos 6\varphi$ and $\cos 3\varphi$ harmonics numerically. We proceed as follows: a series of minimisation runs at different H is made. Every time the result is fit by the three-parameter function $\Delta E(\varphi) = A_6 \cos 6\varphi + A_3 \cos 3\varphi - C$. The obtained amplitudes are plotted in figure 6.11, from where, making another fit, the field dependence of the coefficients is extracted

$$A_6(H) = A_6^{(2)}H^2 + A_6^{(4)}H^4 + O(H^6); \qquad A_3(H) = A_3^{(3)}H^3 + O(H^5). \tag{6.47}$$

Simple analysis of section 6.1.3 states that the phase transition occurs at $\zeta = 1$ (see eqs. (6.21) and (6.22)), or when the magnetic field satisfies the condition $A_6(H_C) - A_6^Q = A_3(H_C)/4$.

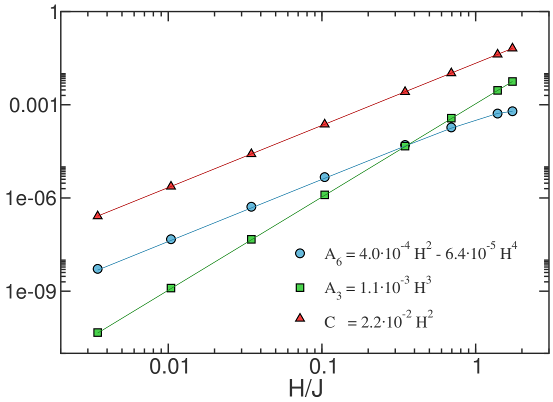

Figure 6.11: Data points are the amplitudes of harmonics of $\Delta E(\varphi) = A_6 \cos 6\varphi - A_3 \cos_3 \varphi - C$ from numerical angle-resolved energy minimisation (see section 6.2.5) for $T = 0$ and different strengths of magnetic field $\mathbf{H} \parallel [111]$. Lines - are fits of the data to expressions (6.47). The corresponding fitting parameters are given in the legend.

Below we maximise A_6^Q as a function of magnetic field to obtain its critical value when the transition still exists. Using (6.47), we obtain that an extremum $A_{6\,\mathrm{crit}}^Q$ is reached when

$$A_6^{(2)} - \frac{3}{8} A_3^{(3)} H + 2 A_6^{(4)} H^2 = 0. \tag{6.48}$$

Using the interpolated values of coefficients (see legend of Fig. 6.11) and the critical field from the solution of (6.48) ($H_C = 0.79 J_\perp$), we obtain the estimate of the maximum of the quantum order by disorder strength, which allows the appearance of the new field-driven phase $A_{6\,\mathrm{crit}}^Q = 0.9 \cdot 10^{-4} J_\perp$. If we compare this value with the prefactor in eq. (6.45) ($A_{6\,\mathrm{RSPT}}^Q = 1.6 \cdot 10^{-4} J_\perp$), we see that it is probable that in real $\mathrm{Er_2Ti_2O_7}$ quantum fluctuations hide the new phase completely. However, as the values are close, due to the aforementioned uncertainty in the order by disorder strength, the absence of phase transition should still be confirmed in the experiment.

6.5 Summary

To summarise, in this chapter we have presented the theory for the anisotropic easy-plane pyrochlore antiferromagnet in the external magnetic field. It is directly applicable for the rare-earth pyrochlore compound $\mathrm{Er_2Ti_2O_7}$. We have made a series of predictions that are observable and that would be interesting to study experimentally. We list them below.

1) A finite field second order Ising phase transition inside the antiferromagnetic phase is present for $\mathbf{H} \parallel \langle 001 \rangle$ case *and* absent when $\mathbf{H} \parallel \langle 110 \rangle$. The transitions can be detected either by magnetisation measurements, or by observing different neutron diffraction patterns above and below the critical field.

2) At $T = 0$ it occurs at $H_C(0) = 0.040 H_S$. The whole transition line is nonmonotonic with the broad maximum $H_C^{\max} = 0.047 H_S$ around $T = 0.2 T_N$.

3) The measured value of $H_C(0)$ is directly associated with the quantum order by disorder strength. It may be used as a benchmark for theoretical calculations of [6, 7, 83], alternative to the measurements of the spin-wave gape of Ross *et al.* [73].

4) The maximum in H_C is caused solely by the thermal order by disorder, its observation would mean a direct probe of the effect.

5) At $\mathbf{H} \parallel \langle 111 \rangle$ the possibility of a pair of transitions at very low T is not completely ruled out. However, a very precise sample orientation is needed as even a small misalignment of the magnetic field from the symmetry axis wipes out the effect even in the classical system.

Chapter 7

Order by structural disorder in orbital models

Orbital models are usually taken on regular bipartite lattices: square, cubic or hexagonal. However, due to the directional nature of interactions, the models are highly frustrated and have nontrivial sets of discrete gauge-like symmetries. In addition, their ground state manifold is subject to an emergent continuous rotation symmetry, which can be lifted via the order by disorder mechanism. Indeed, thermal [93–95] and quantum [96] fluctuations are known to stabilise ordered phases in these models. Similar to antiferromagnetic systems, discussed above, we can study state selection and ordering by impurities in orbital models. This introduces a new family of frustrated models for probing our scenario of competition between fluctuations and structural disorder. Furthermore, it gives access to a whole new class of real systems, where a concept of order by structural disorder can be observed experimentally - doped Mott insulators.

Diluted orbital models were studied numerically in a series of works by Tanaka and collaborators [97–99]. In the classical limit, the long range order was found to be suppressed by dilution much faster than in the corresponding Heisenberg models. The reason for this is the directional nature of the couplings and effective dimensional reduction that takes place in the models. This is especially relevant for the t_{2g} model, where the long-range order state is quasi-one-dimensional and very susceptible to structural defects.

In this work we study essentially the same systems: randomly diluted classical orbital models. However, we raise a different and more fundamental question of the possibility of long range order, stabilised by structural disorder. Surprisingly, the results for e_g and t_{2g} models are notably distinct from the triangular and pyrochlore systems, studied above and also differ from each other. In section 7.2 we study the low-temperature properties of the e_g orbital model. It exhibits a nontrivial impurity-induced phase, which is stabilised necessarily by both thermal fluctuations and structural disorder. On the other hand gauge-like symmetries of 2D and 3D t_{2g} models do not allow the appearance of a new phase. In sections 7.3 and 7.4 we show that impurities restore the symmetry broken in the nematic phase, so both systems exhibit a reentrant transition a to a disordered phase at low T.

7.1 Introduction and physical origins of 120° and 90° compass models

In this chapter we study the effect of random dilution on three different but closely related frustrated models. They all can be written in a general symmetrical form as

$$\hat{\mathcal{H}} = -J \sum_{i,\alpha} S_i^\alpha S_{i+\mathbf{e}_\alpha}^\alpha, \tag{7.1}$$

with the crucial common feature: the internal spin degrees of freedom of the models are coupled to the external spatial ones, so the interaction is directionally dependent. One of the outcomes of this is that orbital models are highly frustrated, even when the underlying lattice is not, which opens a new dimension in the field of frustrated systems.

The most basic realisation of directional model, described by the Hamiltonian (7.1) is when α are Cartesian directions $\alpha = \{x, y, z\}$, so that $\mathbf{e}_\alpha$ correspond to three unit translation vectors of the cubic lattice in the real space. Pseudospins S^α denote Cartesian components of classical vector spins. Then the Hamiltonian can be written in the explicit form as

$$\hat{\mathcal{H}} = -J \sum_{i} S_i^x S_{i+\mathbf{e}_x}^x + S_i^y S_{i+\mathbf{e}_y}^y + S_i^z S_{i+\mathbf{e}_z}^z, \tag{7.2}$$

Following the terminology of the review [100], we call this model the 3D 90° compass model. Spins interact with three different components along three Cartesian axes.

Its two dimensional counterpart is defined exactly the same way, with spins being planar XY-type vectors, residing on a square lattice, so $\alpha = \{x, y\}$. This model may be less captivating from the point of view of direct application, but it is certainly more illustrative and simple, and in many aspects it behaves similarly to the cubic 3D 90° compass model.

In the third considered model α again defines three coordinate axes, which we denote now by $\alpha = \{a, b, c\}$. In the real space they coincide with Cartesian coordinates $(\mathbf{e}_a, \mathbf{e}_b, \mathbf{e}_c) = (\mathbf{e}_x, \mathbf{e}_y, \mathbf{e}_z)$, while in the spin space they define three equally spaced directions in *two* dimensions:

$$S^a = -\frac{1}{2} S^z + \frac{\sqrt{3}}{2} S^x, \qquad S^b = -\frac{1}{2} S^z - \frac{\sqrt{3}}{2} S^x, \qquad S^c = S^z, \tag{7.3}$$

like it is done in Fig. 7.1 (a). The relative angle between the axes is $2\pi/3$, so the model is called the 120° compass model or the e_g model (see below).

Next to motivate our study, we give a brief overview of physical phenomena that are characterised by compass models. For a more extensive information one can refer to recent extensive reviews on the models written by Nussinov and van den Brink [100] and Khaliullin [101]. Compass models are known to describe an orbital degree of freedom of the open d shell of transition metal ions in different materials. The crystal field from the surrounding atoms split five d levels into two e_g and three t_{2g} levels. Depending on the number of electrons, occupying the shell, the atomic configuration can be described by an e_g or t_{2g} orbital degree of freedom. Their interaction is directionally dependent due to different spatial extension of five orbitals.

$$\mathbf{e_g}: \qquad \frac{1}{\sqrt{3}}\left(3z^2 - r^2\right), \qquad x^2 - y^2;$$

$$\mathbf{t_{2g}}: \qquad xy, \qquad yz, \qquad zx.$$

Two-flavour e_g and three-flavour t_{2g} orbital states are described by two- and three-component spinors respectively. Then pseudospin operators $\mathbf{S}$, which generate rotations in the degenerate orbital states are represented by a vector of Pauli matrices $\boldsymbol{\sigma}$ or Gell-Mann matrices $\boldsymbol{\lambda}$. In the classical analogues of the models, orbital state is described by a unit vector on a circle or a sphere, therefore the pseudospins $\mathbf{S}$ in the Hamiltonian are two- and three-component classical unit vectors.

The quantum versions of the compass models emerge from the Hubbard Hamiltonian via the Kugel-Khomski mechanism [102], which is the direct generalisation of the superexchange mechanism to orbitally degenerate systems. The multiorbital Hubbard model at half filling in the limit of strong on-site repulsion can be written in the following form $\hat{\mathcal{H}} = \hat{\mathcal{H}}_{\text{spin}} \times \hat{\mathcal{H}}_{\text{orbit}}$. When spin dynamics is absent, as, for example, in ordered ferromagnets, one is left only with the pure orbital part, which takes exactly the form of eq. (7.1).

Purely classical models, which are studied in this work arise when one studies lattice-mediated interaction of orbitals [102, 103]. A selection of a particular orbital state on one site causes a local lattice distortion around it, which itself leads to coherent deformations around neighbouring ions and consecutive orbital selection on them. This collective Jahn-Teller effect induces long-range orbital order at high temperatures. The effect is especially strong for the orbitals of e_g symmetry as they are directed along the ligands (for example, $T_{oo} = 800K$ in KCuF$_3$ [104]). At such high T spin dynamics can be safely integrated out, which authorises the consideration of classical orbital only models.

120° and 90° compass models are often called e_g and t_{2g} orbital models due to their origin. But they are also relevant for describing other physical phenomena, such as superconducting Josephson-junction arrays [105], cold atom systems [106] and magnetic order in some frustrated magnets [107].

Throughout this chapter we refer to the variables of our model (7.1) as spins in analogy with the previously studied magnetic systems. However, one has to remember that usually $\mathbf{S}_i$ describe orbital degrees of freedom, and not magnetic properties of the compound. Similarly, vacancies in these systems represent the absence of a free orbital on this site. In practice this is achieved by doping the compound with electrons or holes. For example, it can be the Cu$^{2+}(3d^9) \rightarrow$ Zn$^{2+}(3d^{10})$ substitution, as in KCu$_{1-x}$Zn$_x$F$_3$ [108] or Fe$^{2+}(3d^6) \rightarrow$ Mn$^{2+}(3d^5)$ in Fe$_{1-x}$Mn$_x$CrO$_4$ [109].

7.2 Order by structural disorder in 120° model

Substitution of spin projections (7.3) into eq. (7.1), gives the Hamiltonian for the classical 120° model

$$\hat{\mathcal{H}} = -J \sum_{i=1}^{N} \left[S_i^z S_{i+\mathbf{e}_c}^z + \frac{1}{4}(S_i^z - \sqrt{3}S_i^x)(S_{i+\mathbf{e}_a}^z - \sqrt{3}S_{i+\mathbf{e}_a}^x) + \frac{1}{4}(S_i^z + \sqrt{3}S_i^x)(S_{i+\mathbf{e}_b}^z + \sqrt{3}S_{i+\mathbf{e}_b}^x) \right]. \tag{7.4}$$

Spins $\mathbf{S_i}$ - are two-component vectors of unit length that are placed on a regular cubic lattice with translation vectors $\{\mathbf{e}_a, \mathbf{e}_b, \mathbf{e}_c\}$. For two-component spins on a regular bipartite lattice the choice of an overall interaction sign is arbitrary. One can always rotate all spins that belong to one sublattice by the angle π around the out-of-plane $\hat{\mathbf{y}}$ axis. Such operation is legitimate and transforms $\mathbf{S}_i \to -\mathbf{S}_i$ for every second spin, it can be viewed as the change of interaction sign. So for simplicity we have chosen the interaction to be ferromagnetic.

Two dimensional unit spins can be parameterised using a single polar angle φ_i. Then the Hamiltonian can be rewritten in the simple form

$$\hat{\mathcal{H}} = -J \sum_{i,\alpha} \cos(\varphi_i + \gamma_\alpha) \cos(\varphi_{i+\mathbf{e}_\alpha} + \gamma_\alpha). \tag{7.5}$$

Three angles $\gamma_\alpha \in \{\frac{4\pi}{3}, \frac{2\pi}{3}, 0\}$ define projections of spins on a, b and c axes (see Fig. 7.1 (a)).

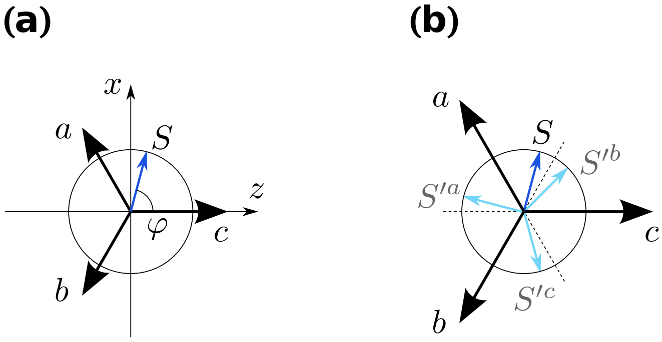

Figure 7.1: (a) A classical 120° model consists of two-component unit spins $\mathbf{S} = (S^z, S^x)$ with bond-dependent coupling. A symmetric form of the model (7.1) is written via the interaction of projections of $\mathbf{S}$ on coordinate axes $\hat{\mathbf{a}}$, $\hat{\mathbf{b}}$ and $\hat{\mathbf{c}}$. (b) Emergent symmetries of the ground state of the model: a circle represents $U(1)$ rotation (type (i)). Light blue arrows illustrate discrete symmetry of type - (ii). S'^a arrow shows a reflection of spin across the $\hat{\mathbf{a}}$ direction that can be done on any $\mathbf{e}_b - \mathbf{e}_c$ plane of the cubic lattice. S'^b and S'^c are defined likewise

Up to an unimportant constant, equation (7.5) can be rewritten as

$$\hat{\mathcal{H}} = \frac{J}{2} \sum_{i,\alpha} \left(\cos(\varphi_i + \gamma_\alpha) - \cos(\varphi_{i+\mathbf{e}_\alpha} + \gamma_\alpha)\right)^2. \tag{7.6}$$

The last expression is obviously minimised by any constant field $\varphi_i = \varphi_0$. Therefore, the ground state of the model is degenerate under $U(1)$ rotations of all spins of the lattice. Throughout this section we call it degeneracy of type (i).

Interestingly, this does not comprise all ground states of the model. In addition to the continuous manifold, there exists an infinite number of distinct spin configurations with the same energy, constructed in the following way. Starting from a state with all $\varphi_i = \varphi_0$ one chooses a direction in the real space $\mathbf{e}_\alpha$, $\alpha \in \{a, b, c\}$. Then one reflects simultaneously all spins that belong to one plane normal to $\mathbf{e}_\alpha$ across the α direction in the spin space (Fig. 7.1(b)). This operation keeps the S^α component untouched, but swaps two other projections $S^{\alpha'} \longleftrightarrow S^{\alpha''}$, so the energy of the state is preserved. This operation can be performed on any number of planes, so in a $N = L^3$ cubic lattice there exists $3 \cdot 2^L$ various stratified ground states. In the following we call it discrete degeneracy of type (ii).

Neither of these two types of degeneracy are true symmetries of the model, but rather belong to the ground state sector of (7.4). It is known that both of them are lifted via the mechanism of thermal order by disorder [93], [94]: entropic selection favours the uniform $\mathbf{Q} = 0$ structure (i.e. with no plane reflections) with $\varphi_i = \frac{\pi k}{3}$. The global aim of the study is to answer the following question: which (if any) of the degeneracies are lifted by structural disorder and how does it modify the ordered state at $T \neq 0$?

7.2.1 Thermal order by disorder

In this subsection we treat analytically a simpler problem of the continuous degeneracy lifting only. Starting from an arbitrary uniform ground state $\varphi_i = \varphi$ we derive corrections to free energy function or mean-field energy, due to thermal and structural disorder. It will be done using the formalism of the real space perturbation theory, presented in chapter 2 and successfully applied to the analogous problems of degeneracy lifting in triangular and pyrochlore frustrated magnets.

First, the entropic selection term is derived. We consider a pure classical system at low T, therefore, the deviations of spins from the ordered state are purely of thermal nature. Following the ideas of chapter 2 we decompose the Hamiltonian (7.5) in a series of small perturbations to the ordered state. In cylindrical coordinates it is convenient to express them in small deviation of the angle $\varphi_i = \varphi + \xi_i$.

$$\begin{aligned}
\hat{\mathcal{H}} &= E_{\mathrm{cl}} + \hat{\mathcal{H}}_0 + \hat{V}_1 + \hat{V}_2 + \cdots\,; \\
\hat{\mathcal{H}}_0 &= \frac{h}{2}\sum_i \xi_i^2; \qquad\qquad h = 3J; \\
\hat{V}_1 &= -\frac{J}{2}\sum_{i,\alpha}(\xi_i + \xi_{i+\mathbf{e}^\alpha})\sin(2\varphi + \gamma_\alpha); \\
\hat{V}_2 &= -J\sum_{i,\alpha}\xi_i\xi_{i+\mathbf{e}^\alpha}\sin^2(\varphi + \gamma_\alpha).
\end{aligned} \tag{7.7}$$

In the pure system the linear term $\hat{V}_1$ is absent and we use the cluster technique on a cubic lattice with interaction $\hat{V}_2$ over an unperturbed Hamiltonian $\hat{\mathcal{H}}_0$. In the 120° model a certain complication comes from the fact that degeneracy lifting terms only appear in the fourth order of perturbation theory. The corresponding correction to the free energy equals to

$$\Delta F_4 = -\frac{\langle \hat{V}_2^4 \rangle}{24T^3} + \frac{\langle \hat{V}_2^2 \rangle^2}{8T^3}, \tag{7.8}$$

where only the first term contributes to the lifting of continuous degeneracy. Indeed, the second order contribution $\Delta F_2 = -\frac{\langle \hat{V}_2^2 \rangle}{2T}$ (and hence the second term in (7.8)) does not depend on the ground state φ. The following correction $\Delta F_3 = \frac{\langle \hat{V}_2^3 \rangle}{6T^2}$ also vanishes because regular cubic lattice, in contrast with the pyrochlore lattice, does not contain triangles. Note that as we got to the fourth order of perturbation theory, we should have included the corrections to the Hamiltonian of higher order in perturbations: $\hat{V}_3$ and $\hat{V}_4$. In particular, third order clusters, depicted in Fig. 7.2 (e) lift the continuous ground state degeneracy. But their contribution is essentially of the higher order in T, so we do not present it in this work.

As follows from the graph technique, described in section 2.1.2, ΔF_4 contributes by four types of coupled clusters. We present them in figure 7.2 (b) - (e), their corresponding combinatorial prefactors are 1, 6, 24 and 24. Gathering all the elements, we get an expression for the contribution of the first cluster

$$\Delta F_4^{(1)} = -\frac{1}{24T^3}\langle \xi^4 \rangle^2 \sum_{i,\alpha} \sin^8\left(\varphi + \gamma_\alpha\right). \tag{7.9}$$

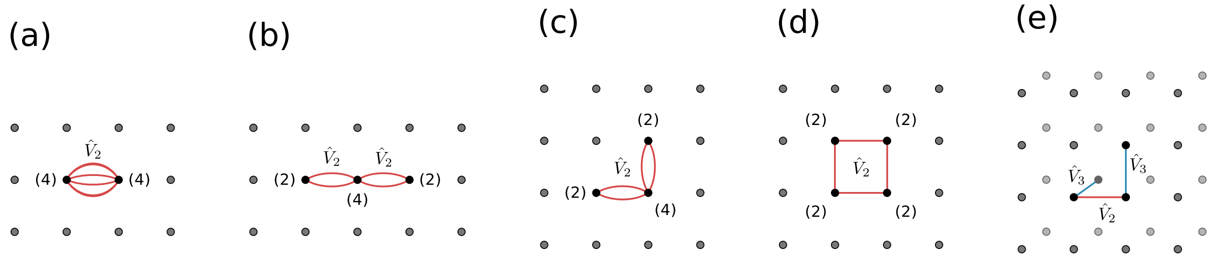

Figure 7.2: (a) - (d) different types of clusters, constructed from $\hat{V}_2$ fluctuation interaction that contribute to the degeneracy breaking in the fourth order of thermodynamic real space perturbation theory. (e) An example of a third order cluster, which also lifts the ground state degeneracy, but is of higher order in T.

Other three terms are calculated similarly. Simplifying all expressions, we get

$$\Delta F_4^{(1)} = \frac{1}{72}\cdot\frac{TN}{128}\big(8\cos(6\varphi)-35\big), \qquad \Delta F_4^{(2)} = \frac{1}{36}\cdot\frac{TN}{128}\big(8\cos(6\varphi)-35\big),$$
$$\Delta F_4^{(3)} = -\frac{1}{18}\cdot\frac{TN}{128}\big(8\cos(6\varphi)+19\big), \qquad \Delta F_4^{(4)} = -\frac{1}{54}\cdot\frac{TN}{128}\big(8\cos(6\varphi)+19\big).$$

Summing up all angular dependent terms the total effect on degeneracy breaking is expressed as

$$\Delta F_4 = -\frac{7}{3456}TN\cos(6\varphi), \tag{7.10}$$

it represents the correction to the free energy due to the thermal fluctuations. Equation (7.10) manifests the fact that the thermal order by disorder favours six configurations with $\varphi_0 = k\pi/3$ from the submanifold of uniform ground states. In the framework of the Jahn-Teller effect they correspond to positive and negative tetragonal deformations along one of the three crystallographic axes $\mathbf{e}_\alpha$.

7.2.2 Ground state selection by site disorder

Next we tackle the problem of lifting the continuous ground state degeneracy by vacancies. Again, we consider only a submanifold of uniform ground states $\varphi_i = \varphi$ and calculate the energy correction, arising from the reconfiguration of spins, surrounding vacancies.

As in the frustrated triangular and anisotropic pyrochlore models, vacancies are treated in the weak-impurity model

$$\mathbf{S}_i \longrightarrow \mathbf{S}_i(1-\epsilon p_i), \qquad S_i^\alpha S_{i+\mathbf{e}_\alpha}^\alpha \to S_i^\alpha S_{i+\mathbf{e}_\alpha}^\alpha\left[1-\epsilon(p_i+p_{i+\mathbf{e}_\alpha})\right]. \tag{7.11}$$

This model as well as the whole procedure of finding the impurity-induced energy correction was thoroughly described in section 2.2.1, here we apply the procedure for the orbital model. Within this approximation the Hamiltonian can be rewritten as

$$\hat{\mathcal{H}}_0 = \frac{h}{2}\sum_i \xi_i^2\left[1-\epsilon p_i - \frac{J\epsilon}{h}\sum_{\pm\alpha} p_{i+\mathbf{e}_\alpha}\cos^2(\varphi+\gamma_\alpha)\right], \tag{7.12}$$

$$\hat{V}_1 = -\frac{J\epsilon}{2}\sum_i \xi_i \sum_{\pm\alpha} p_{i+\mathbf{e}_\alpha}\sin(2\varphi+2\gamma_\alpha). \tag{7.13}$$

Second sums run over the six neighbours of the site i, so α takes positive and negative values from $\alpha \in \{\pm a, \pm b, \pm c\}$. To find the average gain of energy from the spin tiltings this Hamiltonian is minimised to get

$$\Delta E = -\frac{J\epsilon^2}{24}\sum_i \frac{\left(\sum_{\pm\alpha} p_{i+\mathbf{e}_\alpha}\sin(2\varphi+2\gamma_\alpha)\right)^2}{1-\epsilon p_i - \frac{\epsilon}{3}\sum_{\pm\alpha} p_{i+\mathbf{e}_\alpha}\cos^2(\varphi+\gamma_\alpha)}. \tag{7.14}$$

The series of resulting energy corrections was presented in section 2.2.1. The first one, $\Delta E^{(1)}$ does not lift the continuous degeneracy in the 120° model. The following order $\Delta E^{(2)} = O(n_{\mathrm{imp}}^2)$ due to the absence of triangular plaquettes on the cubic lattices. So the leading energy correction $\Delta E^{(3)}$ (see eq. (2.38)), arises from the decomposition of the denominator in (7.14) and is equal to

$$\Delta E^{(3)} = \frac{J\epsilon^3 n_{\mathrm{imp}} N}{96}\cos(6\varphi). \tag{7.15}$$

Therefore, in 120° model the gain of energy from spin reconfiguration is the largest from six states with $\varphi = \pi/6 + \pi k/3$. Similar to the previous models structural disorder favours opposite spin configurations in comparison to thermal fluctuations. Such an ordered state causes orthorhombic deformation of the orbitally ordered systems.

7.2.3 Order parameters for numerical study

Ordering in the classical 120° model was studied numerically by various groups. In the most recent study Wenzel and Läuchli [110, 111] performed large scale Monte Carlo simulations and determined the ordering temperature with great precision $T_c = 0.6775(1)$. Their estimates for the critical exponents of the model leave a possibility for the transition to the long range order state to belong to a new universality class, distinct from the anticipated 3D-XY class. Unlike previous models in this study, good Monte Carlo studies of the 120° model with vacancies exist. Tanaka and Ishihara [97, 99] studied a problem of T_c reduction with defect concentration. They have found that long range order disappears much faster than in the analogous Heisenberg system, but persists at least up to reasonably high $n_c \simeq 20\%$.

In this work we study exactly the same model with vacancies, but bring up a somewhat more general question of the ground state degeneracy lifting and the establishment of long range order in a system with vacancies. The discrete ground state degeneracy (type-(ii)) is of particular interest, as it was not covered by our analytical research of the previous subsections. The studied impurity concentrations are well below the critical value $n_{\mathrm{imp}} < n_c$ from the work [97]. We also note that with respect to T_c reduction by vacancies, our findings and are consistent with the results of Tanaka and Ishihara.

The serious complication, brought by the 120° model to the numerical simulations is the difficulty of construction of a good order parameter. Any uniform ordered state has nonzero magnetisation

$$m = \sqrt{M_x^2 + M_y^2}; \qquad M_\alpha = \frac{1}{N}\sum_i S^\alpha. \tag{7.16}$$

In the analogy with the sixfold order parameter, used for pyrochlores (5.39) m_6 can be measured to observe the lifting of the continuous symmetry:

$$m_6 = \frac{\mathrm{Re}(M_x + iM_y)^6}{m^5} = m\cos 6\varphi. \tag{7.17}$$

However, functions m and m_6 are valid order parameters only within the subspace of uniform ground states, outside the $\mathbf{Q} = 0$ sector they take arbitrary values. So one should study order parameters, which are insensitive to type - (ii) discrete symmetry operations, but display the lifting of continuous emergent symmetry. Two competing uniform phases with long-range orbital order can be also identified with the help of the following order parameters:

$$M_{\text{ang}} = \frac{1}{N}\left[\sum_i \cos 3\varphi_i\right]^2, \qquad M_6 = \frac{1}{N}\sum_i \cos 6\varphi_i, \tag{7.18}$$

where $\varphi_i = \text{acos}(S_i^z)$. But contrary to (7.17), M_{ang} and M_6 are not affected by the aforementioned spin flips. Indeed, reflections across three α directions are analogous to transformations $\varphi \to -\varphi$, $\varphi \to -\varphi + 4\pi/3$ and $\varphi \to -\varphi - 4\pi/3$. M_{ang} was used in the work of Tanaka and Ishihara [99], it equals to one in the state with $\varphi_i = \pi n/3$ and zero in competing $\varphi_i = \pi(2n+1)/6$ configurations. The second observable M_6, is analogous to the order parameter that was used by Wenzel and Läuchli to study the critical properties of E_g-clock model [110]. Before presenting our results, we would like to emphasise the difference between the m_6 and M_6 parameters. The former is the sixth harmonic of the overall spin direction of the system and has no sense when type-(ii) reflections are present. The latter is the average of $\cos 6\varphi_i$ projection of individual spins.

We proceed in the similar way how we did before while studying triangular and pyrochlore frustrated magnets. In subsection 7.2.4 we present the results of our deterministic search for ground state using the minimisation algorithm. We show that vacancies lift the continuous degeneracy, while keeping untouched the discrete one. And in the next subsection 7.2.5 we consider the competition of thermal order by disorder and energetic selection by vacancies by the means of classical MC simulations.

Both algorithms are fundamentally similar to the corresponding procedures, used for triangular and pyrochlore systems. Technically we had to adapt them to the planar nature of spins. The first major alteration comes from the fact that the local field, calculated in minimisation and overrelaxation procedures now has to be confined to the spin plane. And the second one is a restriction of MC single spin moves to a plane – one single trial angle φ_i was used on every move.

7.2.4 Numerical $T = 0$ ground state minimisation

Figure 7.3 shows the results of our minimisation study for different cluster sizes L and vacancy concentrations n_{imp}. For all runs M_6, averaged over 100 impurity replicas is negative, decreasing at larger clusters. It suggests that structural disorder favours configurations that are normally least supported by thermal fluctuations, namely $\varphi_i = \pi(2n+1)/6$ states within the uniform nonstratified configurations. We note, however, that structure distortions are somewhat stronger than in frustrated systems, studied before: already $n_{\text{imp}} = 5\%$ of vacancies significantly reduces $|M_6|$, from unity.

Another important obtained result is the absence of selection of the wave vector. In Fig. 7.4 (a) we plot a histogram of m at the global minima points for different realisations of impurities for $n_{\text{imp}} = 3\%$ and $L = 14$. We have sampled about $5 \cdot 10^3$ impurity realisations and $4 \cdot 10^3$ random initial conditions for each vacancy replica. One can clearly see seven clusters of minima, which correspond to different branches of degenerate ground states with different numbers of flipped

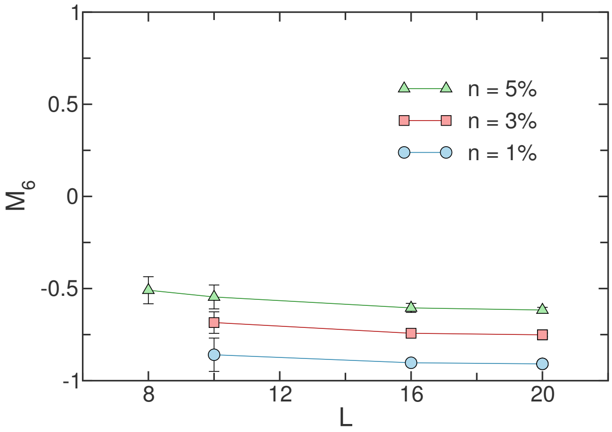

Figure 7.3: Results of the numerical energy minimisation for the 120° model with different concentrations of impurities. Data points and error bars are obtained from the statistical averaging over 100 impurity replicas. Negative values of M_6 evidence for the stabilisation of the states with $\varphi_i = \pi(2n+1)/6$.

spin planes. This histogram does not suggest any type of selection of specific plane-flip patterns, showing a rather smooth distribution of minima over different branches of degenerate ground states. The distribution is qualitatively consistent with the relative volumes that these branches have in the phase space: for a cubic cluster of size L there are $3C_k^L$ ways to flip k spin planes, each configuration has the same value of m. We note that the last branch, which corresponds to uniform spin configuration, is fully or almost absent on this histogram. While this may indicate that a $Q = 0$ structure is disfavoured by impurities, we do not approve this scenario. We believe that this fact is due to a very low statistical weight of uniform ground states, as (i) the same effect is also observed on a clean system, and (ii) one finds global minima with $m \simeq 1$ when some imposed starting uniform spin configuration are added to the random initial configurations.

In this section we have presented the results of our numerical minimisation procedure. It is

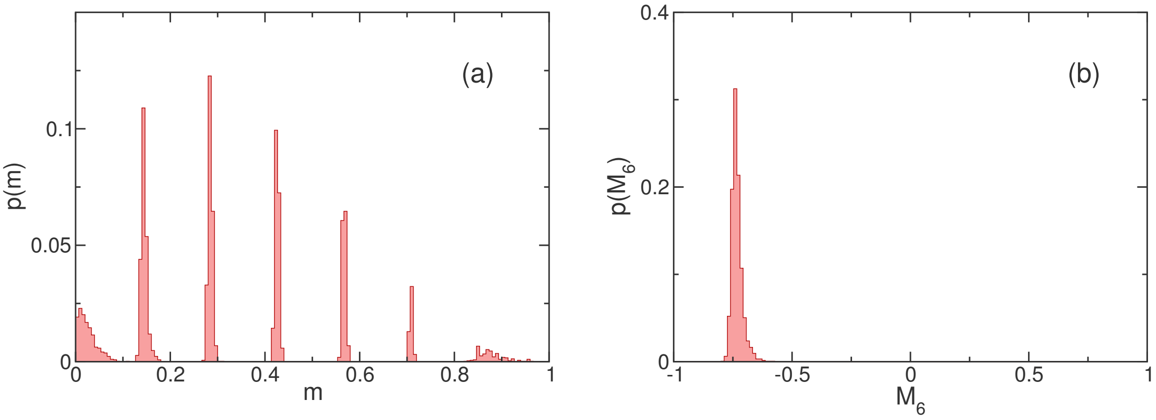

Figure 7.4: Distribution of order parameters in the global minima of the system with $n_{\text{imp}} = 3\%$ of static vacancies randomly set over a cubic lattice with linear size $L = 14$ at $T = 0$. (a) Multi-peak structure of $p(m)$ exhibits the absence of breaking of a discrete symmetry of type (ii), while (b) a narrow distribution of a sixfold order parameter M_6 shows that minima with $\varphi = \pi/6 + \pi k/3$ are robustly selected by vacancies. Histograms are plotted upon $5 \cdot 10^3$ different impurity replicas.

unlikely that in our simulations we have always found a true state with the minimum of energy due to the huge phase space of classically degenerate ground states and the roughness of the energy landscape, generated by impurities. However, based on the presented results: (a) negative M_6, which decreases with growing L and number of sampled initial random conditions and (b) absence of preferred pattern of flipped spin planes, we state that vacancies in the 120° model lift the continuous degeneracy of type-(i) in favour of states with $\varphi_i \in \pi/6 + n\pi/3$, but leave the discrete degeneracy of type-(ii) intact.

7.2.5 Finite temperature classical Monte Carlo simulations

In this section we present the results of our MC simulations. We focus on the low-T region of parameter range and probe dilution rates surely below the critical value $n_{\text{imp}} \leq 10\% < n_c = 17\%$, found by Tanaka and Ishihara [97]. We show that vacancies induce an additional phase transition into the phase with $Q = 0$ and $\varphi_i = \pi/6 + n\pi/3$.

The general scheme of the MC algorithm, used in this study was presented in section 3.1, and exact values of the simulation parameters are listed in table 3.1. Here we note two main features, distinct from the previous simulations: presence of discrete symmetry greatly increases the volume of low-energy phase space that has to be probed. Moreover, different branches of degenerate states with different flipped planes are very weakly interconnected. So we increased a number of independent runs, made for each impurity replica, in order to compensate this phase space enlargement and to better probe the low-energy states of the system. Secondly, for the MC simulations of the compass models we used both periodic (PBC) and screw-periodic boundary conditions (SBC). The latter are known to significantly reduce finite size effects and improve

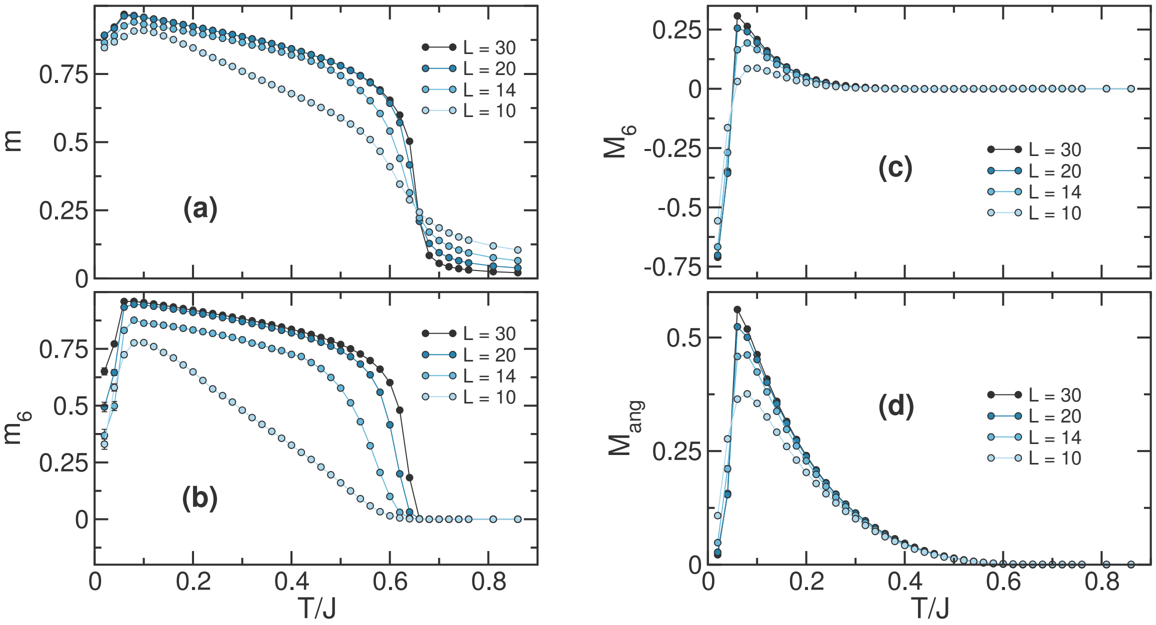

Figure 7.5: Finite-size behaviour of four order parameters (7.16) - (7.18). 120° model with $n_{\text{imp}} = 1\%$ of impurities was studied by the hybrid Monte-Carlo algorithm with periodic boundary conditions. M_{ang} and M_6 show the transition to the low-T ordered phase with $\varphi = \frac{\pi}{6} + \frac{\pi k}{3}$. It is a uniform state with $\mathbf{Q} = 0$, as follows from the finite size analysis of m.

scaling in orbital models [110, 112, 113]. On the other hand, SBC support $Q = 0$ ordering on the boundaries. Therefore, as one of the questions under study was the selection of the ordering vector by impurities, we concentrated on simulations with the usual periodic boundaries.

Figures 7.5 (a) - (d) show various order parameters (7.16) - (7.18) for different cluster sizes $L \leq 30$ in the presence of $n_{\rm imp} = 1\%$ of vacancies. Negative values of the multipole parameter M_6 at $T \to 0$ clearly indicate breaking of the continuous symmetry into a state with $\varphi_i = \pi/6 + n\pi/3$. We also note good agreement between finite-T values of the order parameter and its limiting values in Fig. 7.3. Unfortunately, one cannot rely on M_6 at higher temperatures. An order parameter, constructed as $\sum \cos(k\varphi_i)$ can only be used if at any moment the distribution of angles $p(\varphi)$ is not too wide (modulo spin flips). For example, the Gaussian-like distribution of angles should have $2k\sigma(\varphi) < \pi$. In our model at high T thermal fluctuations are so strong that $M_6 = 0$ far inside the phase with actually broken continuous degeneracy. The same considerations are valid for $M_{\rm ang}$, we suppose that it is the reason why no finite size effects were observed in Ref. [99].

Nevertheless, at lower temperature $M_{\rm ang}$ evidences the presence of both ordered phases at $n_{\rm imp} = 1\%$. The intermediate conventional phase, stabilised by thermal order by disorder at high T is confirmed by $m_6 \to 1$. This order parameter, however, should be used with care, as it assumes a $Q = 0$ structure, otherwise if some spin plane flips are present, m_6 may take arbitrary values.

The main order parameter m converges smoother to unity for larger clusters. A dip in m close to the low-T phase transition was also observed in Ref. [99] and is, indeed, a finite cluster size effect. The fact that it monotonically disappears at high L and is completely absent for the runs

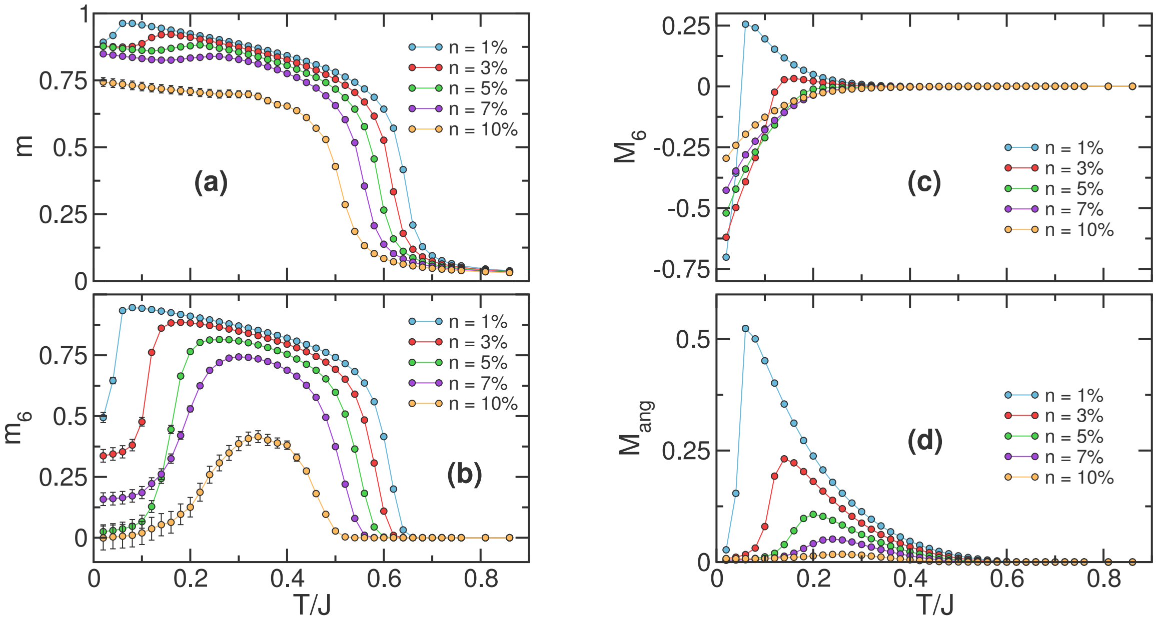

Figure 7.6: Dependence of order parameters (7.16) - (7.18) on impurity concentration at finite temperatures. Monte Carlo simulations were performed on systems with $L = 20$ and periodic boundary conditions. The boundary to the new phase with $\varphi = \frac{\pi}{6} + \frac{\pi k}{3}$ shifts to higher temperatures with the strength of disorder. The first-order phase transition at low T gets significantly smeared by impurities.

with SBC (see below) supports our statement that dilution, while competing with conventional order by disorder in breaking the continuous $U(1)$ symmetry, does not destroy $Q = 0$ long-range order, or induce any other spin pattern.

Similarly to the triangular and pyrochlore antiferromagnets, presented above, the vacancy induced phase transition is a first order phase transition. Like before for small n_{imp} this reconfigurational transition is rather abrupt. Larger concentration of impurities smear out this first order transition very quickly. The results of MC simulations of more disordered systems are shown in figs. 7.6 (a) - (d). Stronger finite size effects are observed in more diluted systems, m and m_6 are mainly affected. On the other hand, panels (c) and (d) show that the sequence of phases should stay the same at least up to $n_{\mathrm{imp}} = 7\%$.

For completeness in figure 7.7 we present the results of the runs with the screw-periodic boundary conditions. They show that suppression of finite size effects results in a more robust $\mathbf{Q} = 0$ structure. As a result even m_6 has negative values and shows an onset of a $\varphi_i = \pi/6 + n\pi/3$ phase (we emphasize the difference between panels (b) of Fig. 7.6 and 7.7). The multipole order parameters M_6 and M_{ang} are only weakly affected by SBC and show the same sequence of phases as before.

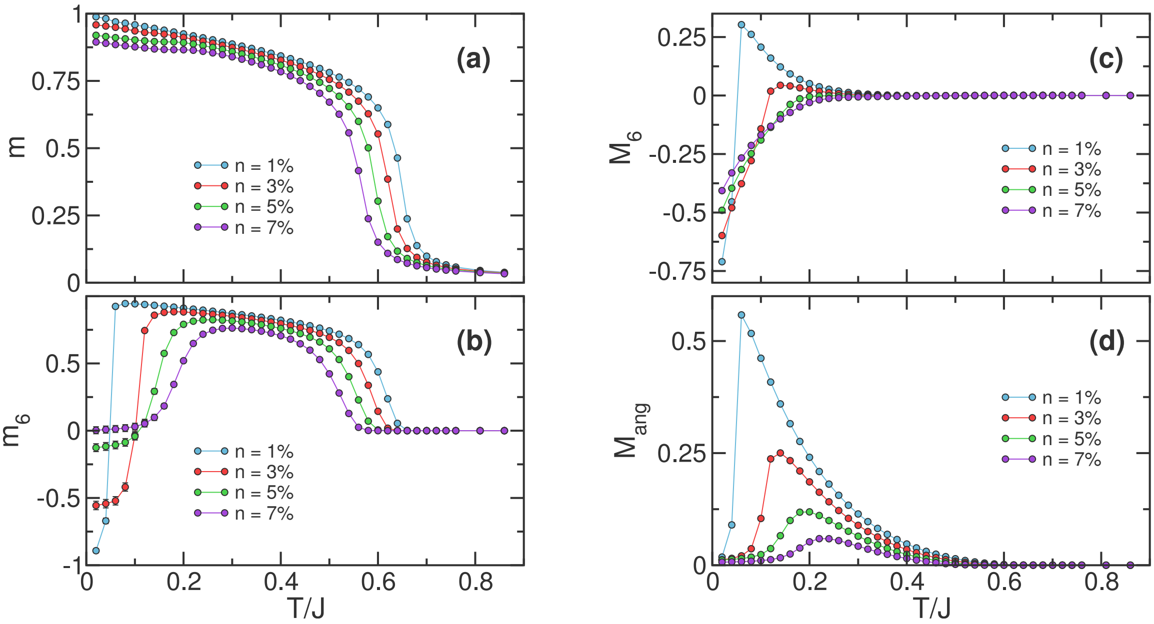

Figure 7.7: Results of Monte Carlo simulations with $L = 20$ and screw-periodic boundary conditions. SBC support the $\mathbf{Q} = 0$ structure and increase the effective lattice size, which results in a better convergence of m and m_6 order parameters.

To sum up we have shown the appearance of a new phase at low temperatures inside the long-range order region of the classical 120° model. The main feature of this phase is that it requires the presence of *both* thermal and structural order by disorder, which is somewhat different from what is observed in the triangular or pyrochlore antiferromagnets. Dilution leaves discrete degeneracy intact, and thermally-induced $Q = 0$ structure is retained. On the other hand impurities compete with thermal order by disorder in breaking the continuous $U(1)$ symmetry. At low T it prevails and stabilises a structure with $\varphi_i = \pi/6 + n\pi/3$.

7.3 Reentrant transition due to impurities in 2D 90° compass model

The behaviour of t_{2g} models is slightly different from the e_g case studied above. First, we analyse a simpler 2D model, which is described by the Hamiltonian

$$\hat{\mathcal{H}} = -J \sum_i S_i^x S_{i+\mathbf{e}_x}^x + S_i^y S_{i+\mathbf{e}_y}^y. \tag{7.19}$$

S - are 2D vectors of unit length with components $S_i^x = \cos\varphi_i$ and $S_i^y = \sin\varphi_i$, sitting on a regular square lattice. The overall sign if the interaction is not important as it can be gauged away by the rotation in the xy plane (see discussion below eq. (7.4)), so for simplicity we choose the ferromagnetic interaction between the spins $J > 0$.

The analysis of ordered phases should start with the discussion of symmetries of the Hamiltonian, which are nontrivial in all compass models. This system remains invariant under the following two transformations: (I) a $\mathbb{Z}_2$ symmetry of reflection across the [110] direction, which results in $(S^x \to S^y, S^y \to S^x)$ transformation. And (II) changing sign of S^y (S^x) component of each spin that belongs to any one column (row) of the lattice. This 1D spin flip transformation is somewhat similar to the discrete type-(ii) symmetry, of the previous section. But we would like to emphasise, though, that in the 90° model it is the true symmetry of the model, while in the 120° model it emerged in the ground state sector only. We illustrate these two symmetries of the model in Fig. 7.8 (a) and (b).

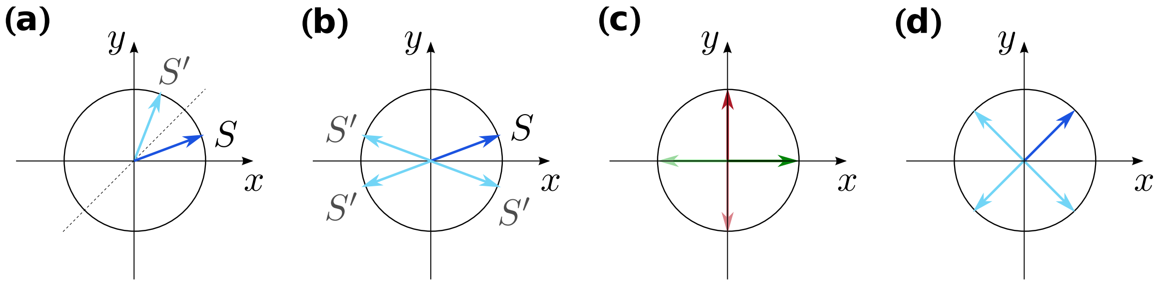

Figure 7.8: True symmetries of the 2D 90° compass model: (a) global $\mathbb{Z}_2$ coordinate permutation and (b) 1D gauge-like independent spin flips of different columns and rows. (c) Nematic states, stabilised by thermal order by disorder, with broken $\mathbb{Z}_2$ symmetry. (d) Spin configuration, favoured by structural disorder.

Symmetry (I) is a discrete global symmetry, so it can be broken at finite temperature in 2D. This will be equivalent to $C_4 \to C_2$ transition in terms of lattice rotations. On the contrary the 1D nature of the gauge-like symmetry (II) prevents it from being broken at any finite temperature, as follows from the Elitzur's theorem [114, 115]. The important consequence of this fact is that conventional magnetic order with the order parameter $\mathbf{M}_Q = \sum \mathbf{S}_i \exp(i\mathbf{Q}\cdot\mathbf{r}_i)$ for any wave vector $\mathbf{Q}$ is prohibited at $T > 0$.

Each spin has only one degree of freedom, and we can rewrite the Hamiltonian in the trigonometric form

$$\hat{\mathcal{H}} = -J \sum_i \cos\varphi_i \cos\varphi_{i+\mathbf{e}_x} + \sin\varphi_i \sin\varphi_{i+\mathbf{e}_y}. \tag{7.20}$$

This function is minimised by any constant spin configuration $\varphi_i = \varphi$. So the ground state sector of the model is invariant under $U(1)$ rotations. This degeneracy, however, is accidental and can be lifted when fluctuations around a ground state or relaxation of the structure due to vacancies is taken into account. In the following two subsections, working in the manifold of uniform configurations and employing the formalism of real space perturbation theory, we derive state selection terms.

7.3.1 Thermal order by disorder

Fluctuations of spins around an arbitrary uniform ground state can be described by a set of small angles $\xi_i = \varphi_i - \varphi$. Substituting them into eq. (7.20) and decomposing trigonometric functions in series of small ξ_i, we get

$$\begin{aligned}
\hat{\mathcal{H}} &= E_{\mathrm{cl}} + \hat{\mathcal{H}}_0 + \hat{V}_1 + \hat{V}_2 + \cdots ; \\
\hat{\mathcal{H}}_0 &= -\frac{h}{2}\sum_i (1-\xi_i^2); \qquad\qquad h = 2J; \\
\hat{V}_1 &= \frac{J}{2}\sum_i (\xi_i + \xi_{i+\mathbf{e}_x} - \xi_i - \xi_{i+\mathbf{e}_y}) \sin 2\varphi; \\
\hat{V}_2 &= -J\sum_i \xi_i \xi_{i+\mathbf{e}_x} \sin^2\varphi + \xi_i \xi_{i+\mathbf{e}_y} \cos^2\varphi.
\end{aligned}$$

One can easily see that the linear term $\hat{V}_1$ vanishes in the pure system, which is consistent with the fact that we make a decomposition around a ground state. However, we include this term as it will give the principal correction in the case of the system with quenched disorder.

Now we can use the thermodynamic perturbation theory to calculate the entropy of ground states. In this system accidental continuous degeneracy is lifted already in the second order, the correction to the free energy is $\Delta F^{(2)} = -\frac{\langle \hat{V}_2^2 \rangle}{2T}$ and results in a degeneracy lifting term

$$\Delta F^{(2)} = -\frac{TN}{32}\cos 4\varphi. \tag{7.21}$$

Thermal fluctuations favour the configurations with $\varphi_0 = \frac{\pi k}{2}$ or spin ordering along the bonds of the square lattice. It is easy to show that in the Ginzburg-Landau expansion this term would correspond to a fourth order invariant $\delta F = -A(T)[m_x^4 + m_y^4]$. The main features of such states is that application of chain flip symmetry of type - (II) splits four possible fluctuation-stabilised uniform configurations in two families of stratified states with no mixing between them. In figure 7.8 (c) we show these classes of configurations with $\varphi = 0, \pi$ and $\varphi = \frac{\pi}{2}, \frac{3\pi}{2}$ by different colours.

Therefore, thermal fluctuations lift the accidental continuous degeneracy of ground states via term $\delta F = -A(T)[m_x^4 + m_y^4]$ and stabilise the nematic state with spontaneously broken Ising symmetry of type-(I).

7.3.2 Order by structural disorder

As we have shown before, introduction of weak random dilution to a model generates a nonzero linear term in the Hamiltonian. We can parameterise the projections of spins on coordinate axes via the phase angles $\gamma^\alpha = \{0, \pi/2\}$, like it was done in eq. (7.5). Then $\hat{V}_1$ takes exactly the same form (7.13), as in the 120° model

$$\hat{V}_1 = \frac{J\epsilon}{2}\sin 2\varphi \sum_i \xi_i \sum_{j=1}^{4} p_j \mathrm{e}^{2i\gamma_{ij}}. \tag{7.22}$$

Like before to obtain the selection from local energy optimisation around impurities, we minimise the Hamiltonian $\hat{\mathcal{H}}_0 + \hat{V}_1$ over the spin deviations ξ_i. A linear in n_{imp} nontrivial energy correction is obtained already at the leading correction of the type (2.35):

$$\Delta E^{(1)} = \frac{JNn_{\text{imp}}\epsilon^2}{8}\left(\cos 4\varphi - 1\right). \tag{7.23}$$

This fourfold anisotropy has an opposite sign to the conventional order by disorder term (7.21) and competes with it in state selection. Accordingly, the corresponding invariant differs by a prefactor $\delta F = B(n_{\text{imp}})[m_x^4 + m_y^4]$.

The striking difference with the entropically selected states is that ordering along the diagonals of the lattice preserves the $\mathbb{Z}_2$ symmetry (I). Figure 7.8 (d) illustrates this fact with a dark arrow, depicting a uniform $\varphi = \pi/4$ state and lighter arrows illustrating the direction of rows or columns in stratified states. Thus a state, favoured by (7.23), has the same symmetry as the paramagnetic state and is smoothly connected to it. This situation is similar to the anticollinear state, stabilised by vacancies in $J_1 - J_2$ model [24].

7.3.3 Numerical results and reentrant phase transition

The classical 2D 90° compass model was extensively studied numerically by Monte Carlo simulations. Mishra and collaborators [95] were the first to observe the low-T phase transition to the nematic state at $T_c/J = 0.147$. They also predicted the 2D Ising universality class of the transition, which was later confirmed by Wenzel and Janke [116] in their thorough numerical study. In addition to this, Tanaka and Ishihara [98] studied decrease of T_C by dilution in the 2D compass model on a square lattice by the means of both classical and quantum Monte Carlo simulations.

Due to the effective one-dimensional nature of the ordered state, orbital compass models exhibit extremely strong finite size effects and nonregular scaling behaviour [112]. That is why periodic boundary conditions are avoided in numerical studies in favour of fluctuating [95] or screw-periodic boundaries [112]. As this model does not allow the breaking of translational symmetry, we are no longer interested in considering all stratified patterns on equal footing. So our MC simulations of 90° model were also made with screw-periodic boundary conditions. They are technically defined by

$$\begin{aligned} (x, y+1) &= \begin{cases} (x, y+1) & \text{if } y < L, \\ ([x+S] \bmod L, 1) & \text{if } y = L; \end{cases} \\ (x+1, y) &= \begin{cases} (x+1, y) & \text{if } x < L, \\ (1, [y+S] \bmod L) & \text{if } x = L; \end{cases} \end{aligned} \tag{7.24}$$

where $(x, y+1)$ denotes the nearest neighbour of site $i = (x, y)$. S - is a screw parameter, which determines the deformation of the torus on the boundaries. We took $S = 1$, which was found to be an efficient choice for the screw parameter [112].

Directional ordering is traced by the order parameter M_2, constructed in analogy with (7.18):

$$\left|M_2\right| = \frac{1}{N}\Big|\sum_i \cos 2\varphi_i\Big| = \frac{1}{N}\Big|\sum_i \left(S_i^{x2} - S_i^{y2}\right)\Big|. \tag{7.25}$$

This observable was also used in the work [95]. The exact transition temperature was determined using its Binder cumulant $U_B(|M_2|)$. Moreover, to illustrate the nature nature of the ordered states we used a fourfold correlation function $M_4 = 1/N \sum \cos 4\varphi_i$. Finally, to be able to compare our results with numerical works by Wenzel *et al* [112, 116], we also measured the nonlocal directional order parameter $D = J/N |\sum (S_i^x S_{i+\mathbf{e}_x}^x - S_i^y S_{i+\mathbf{e}_y}^y)|$, but did not plot it in our figures.

Our results are summarised in figures 7.9 and 7.10. The former shows the finite size analysis for $n_{\text{imp}} = 2\%$ of vacancies, and the latter illustrates suppression of the order with impurity concentration. On both figures the reentrant transition to the paramagnetic phase with the restored symmetry is clearly seen by the decrease of $|M_2|$ order parameter. We note that the low-T feature in the specific heat C (panels (b)) is more pronounced in this model than in other observed systems, where the reconfigurational transition was observed. It is also interesting that M_4 (Fig. 7.9, panel (d)) has a nonzero value above T_c in the paramagnetic region. Therefore, this correlator can not be used as an order parameter, and the low-T phase with negative M_4 has only short range correlations and is not a true phase of the system. Otherwise, the nematic order is, indeed, very quickly suppressed from above in agreement with the work of Tanaka and Ishihara [98].

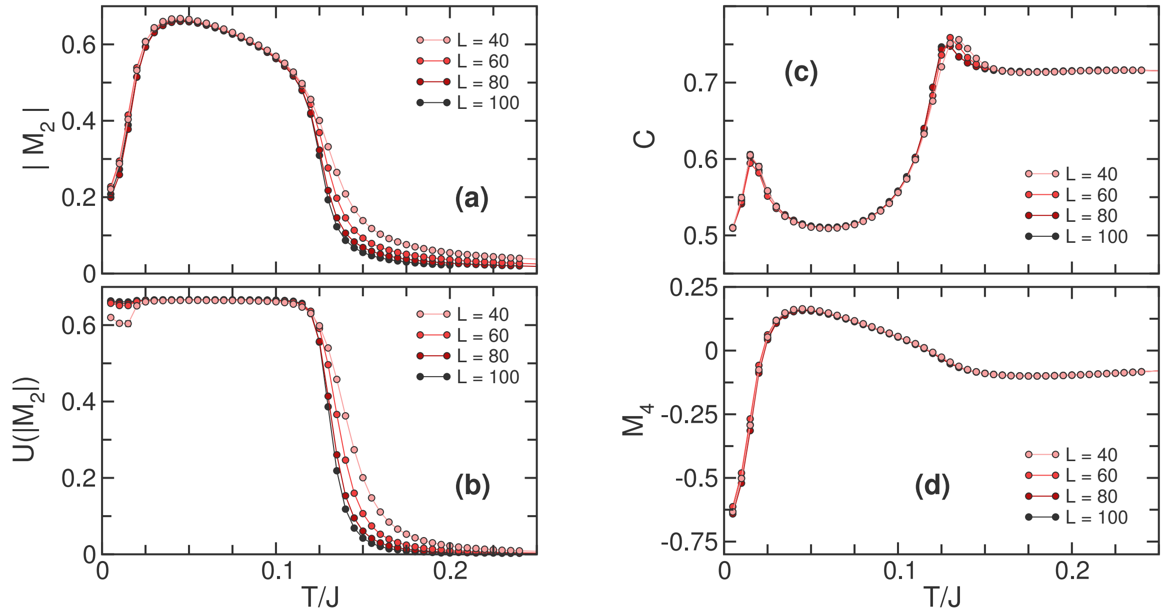

Figure 7.9: Finite size scaling for the classical 2D 90° model with $n_{\text{imp}} = 2\%$ of impurities. Data from Monte Carlo simulations of the square lattice with screw-periodic boundary conditions. Vacancies cause a reentrant phase transition to the paramagnetic phase at $T \simeq 0.02J$ as can be seen from the decrease of $|M_2|$ (panel (a)) and a peak in the specific heat C (panel (c)). Binder cumulant $U(|M_2|)$ is used for the precise determination of the high-T phase transition. Negative values of the correlation function M_4 evidence the positive sign of the disorder-induced energy correction (7.23).

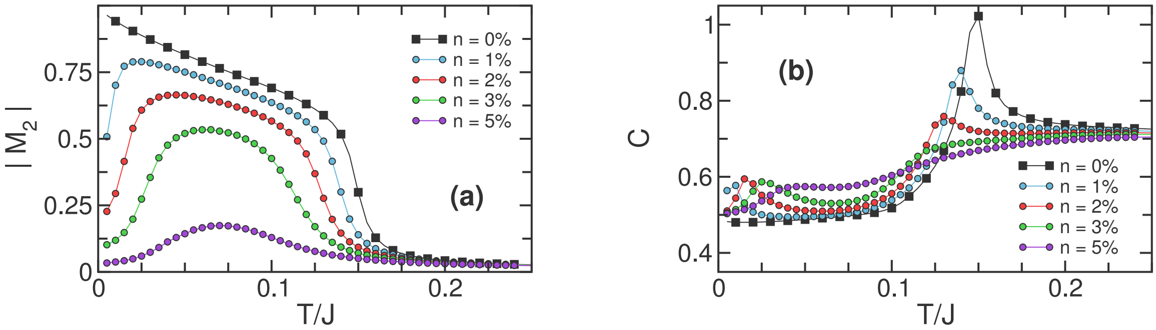

Figure 7.10: Suppression of the nematic phase by vacancies, studied by Monte Carlo with $L = 60$ and SBC. Nematic order is suppressed by already 5% of vacancies. Broad maxima in the order parameter $|M_2|$ and specific heat C are finite size effects.

Finally, in order to illustrate the nature of states in figure 7.11 we present typical MC snapshots of the 10×10 periodic system with and without impurities. The left column corresponds to nematic phase at $T/J = 0.05$, the right column shows the system at $T/J = 0.005$. Two different system behaviours at low T are clearly visible. Different impurity placement - distant and nearby, - on the contrary, has little effect on the system.

We showed that in addition to severe decrease of T_c, the ordered phase is bound from below by the effect of order by structural disorder, realised by the energy correction (7.23) and the model exhibits reentrant behaviour below T_c.

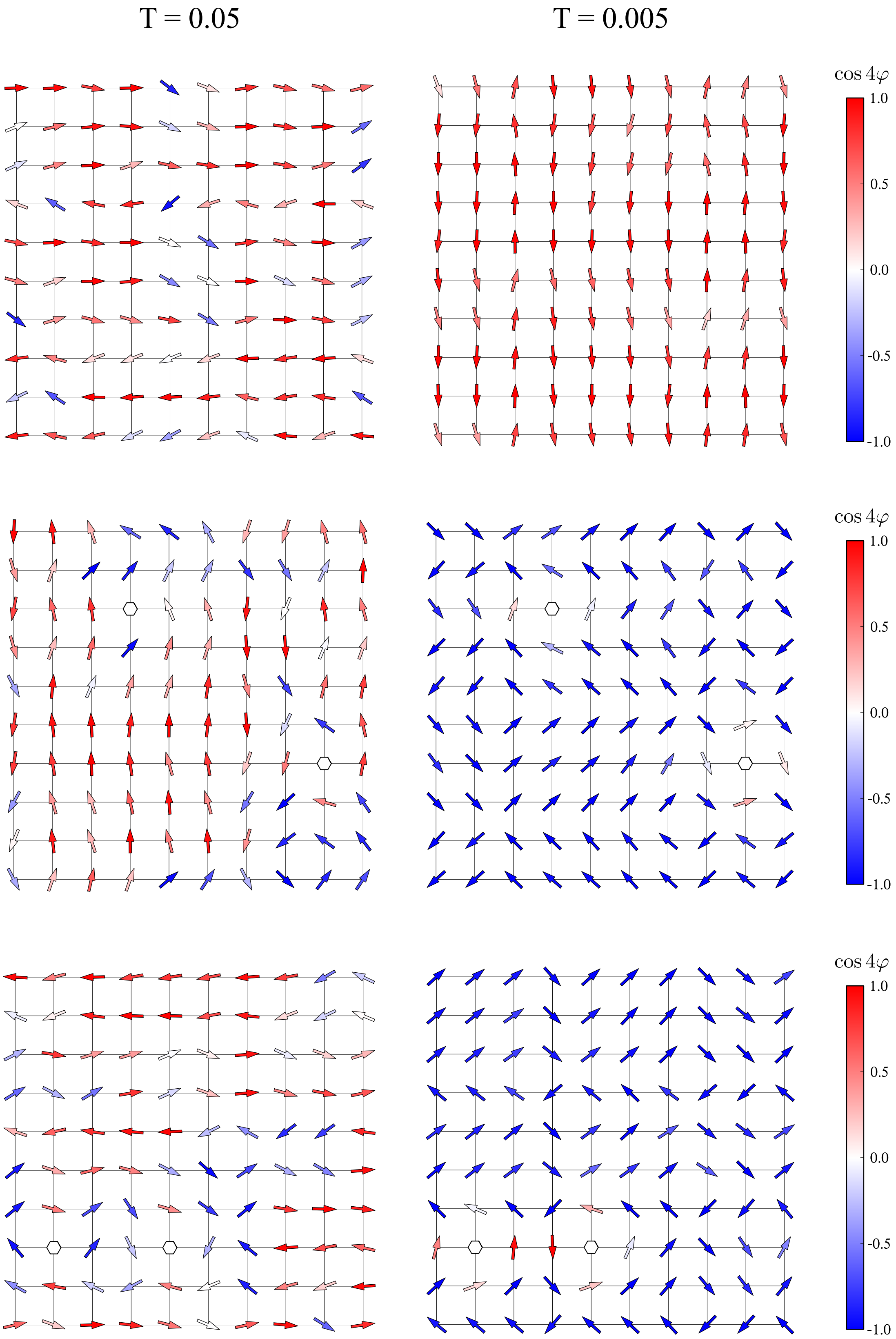

Figure 7.11: Snapshots from MC simulation with $L = 10$ and periodic boundaries taken at $T = 0.05J$ and $T = 0.005J$ ($T_c = 0.147J$ in the clean system). Top row is the simulation of the clean system, middle and bottom rows correspond to $n_{\mathrm{imp}} = 2\%$ with different impurity placement.

7.4 Reentrant behaviour in 3D compass model

Finally, we consider a 3D t_{2g} orbital model of interacting classical spins of unit length on a cubic lattice:

$$\hat{\mathcal{H}} = -J \sum_i S_i^x S_{i+\mathbf{e}_x}^x + S_i^y S_{i+\mathbf{e}_y}^y + S_i^z S_{i+\mathbf{e}_z}^z . \tag{7.26}$$

The symmetries of the 90° compass model highly resemble its 2D analogue and constitutes its extension to higher dimension. (I) First, the system is invariant under all operations of the $\mathbb{S}_3$ coordinate permutation group. The Hamiltonian is preserved if one interchanges any pair coordinates of all spins of the system $S^\alpha \longleftrightarrow S^\beta$, $\alpha, \beta \in \{x, y, z\}$. (II) And second, it is possible to reflect one coordinate $S_i^\alpha \to -S_i^\alpha$, of all spins i that belong to one chain parallel to the same cubic direction $\mathbf{e}_\alpha$. The other two coordinates of these spins are left untouched $S_i^\beta \to S_i^\beta$. Any number of such operations can be performed independently on different rows and columns of the cubic lattice.

The local 1D symmetry of type-(II) cannot be broken at any finite temperature [114]. On the other hand, nothing prevents a global symmetry (I) from being broken. We will see that thermal fluctuations stabilise nematic order along one of the cubic axes thus lowering the symmetry $\mathbb{S}_3 \to \mathbb{S}_2$. Also, to avoid confusion, we note that the quantum 3D 90° compass model is less symmetric than its classical counterpart. It possesses only a $(\mathbb{Z}_2)^{3L}$ subset of planar 2D gauge-like flips from the aforementioned $(\mathbb{Z}_2)^{3L^2}$ symmetry, present for the classical spins [100, 105].

Up to an unimportant constant the Hamiltonian (7.26) can be rewritten as

$$\hat{\mathcal{H}} = -\frac{J}{2} \sum_{i,\alpha} \left(S_i^\alpha - S_{i+\mathbf{e}_\alpha}^\alpha \right)^2 , \tag{7.27}$$

so $\hat{\mathcal{H}}$ is obviously minimised by any uniform spin configuration. This suggests that on top of spin reflections the ground state sector of the model is additionally symmetric under the S^2-sphere rotations. This operation does not correspond to any symmetry of the model, and in the following section we show that such accidental degeneracy is lifted by thermal fluctuations and structural disorder. Moreover, the first mechanism additionally triggers lifting of permutation symmetry (I) and stabilisation of nematic order, while the second does not.

7.4.1 Ground state selection by thermal fluctuations and impurities

We consider a uniform ground state, which can be described by two polar angles (θ, φ) and a local reference frame, related to it. Coordinate transform to the local frame is done with the rotation matrix $R(\theta, \varphi) = R_{\hat{\mathbf{z}}}(\varphi) R_{\hat{\mathbf{y}}}(\theta)$. We explicitly denote the spin coordinates in the new reference frame by S^α, so that $\mathbf{S} = R^T \boldsymbol{\mathsf{S}}$ with

$$R^T = \begin{pmatrix} \cos\varphi \cos\theta & -\sin\varphi & \cos\varphi \sin\theta \\ \sin\varphi \cos\theta & \cos\varphi & \sin\varphi \sin\theta \\ -\sin\theta & 0 & \cos\theta \end{pmatrix} . \tag{7.28}$$

In the new frame deviations of spins from a ground state are described by nonvanishing small S^x and S^y. The Hamiltonian (7.26) can be rewritten as a familiar real space expansion series in spin fluctuations $\hat{\mathcal{H}} = E_{\rm cl} + \hat{\mathcal{H}}_0 + \hat{V}_1 + \hat{V}_2 + \ldots$. The noninteracting fluctuation part has a usual simple form

$$\hat{\mathcal{H}}_0 = \frac{h}{2}\sum_i \Big[\mathsf{S}_i^{x2} + \mathsf{S}_i^{y2}\Big], \qquad h = 2J. \tag{7.29}$$

The interaction terms, on the contrary are more complicated, but they are all expressed via the products of the elements of rotation matrix (7.28).

Like in the two-dimensional 90° compass model, thermal fluctuations lift the continuous ground state degeneracy already at the lowest order of perturbation $\Delta F = \langle \hat{V}_2^2\rangle/2T$ via the simple single-bond graphs. Like always, average of square of spin fluctuations equals to $\langle \mathsf{S}^{\alpha 2}\rangle = T/h$, so the total free energy correction can be written as

$$\Delta F^{(2)} = -\frac{TN}{8}\Big[\cos^4\varphi\cos^4\theta + \sin^4\varphi + \sin^4\varphi\cos^4\theta + \cos^4\varphi + \sin^4\theta + \cos^2\theta\sin^2 2\varphi\Big].$$

This expression can be simplified using the components of the order parameter $\mathbf{m} = (\cos\varphi\sin\theta, \sin\varphi\sin\theta, \cos\theta)$:

$$\Delta F = -\frac{TN}{8}\big[m_x^4 + m_y^4 + m_z^4 + 1\big]. \tag{7.30}$$

From the last expression it is clear that free energy is minimised when the spins are directed along one the cubic axes. In the analogy with the 2D model, considered in the previous subsection, such states form three distinct families of states with the spontaneously broken $\mathbb{S}_3$ symmetry of the type (I). Thermal fluctuations stabilise the nematic ordered state at low temperatures. Such state, predicted by Mishra *et al.* [95] was observed numerically only recently in the Monte Carlo simulations by Gerlach and Janke [113].

We now switch to the breaking of the continuous degeneracy of the mean-field ground states by impurities in the weak-vacancy limit. Due to the local relief of frustration, surrounding spins deviate from the former equilibrium configurations and gain energy. This average energy gain can in principle be different for various degenerate states. We determine it for the whole continuous manifold by minimising the spin Hamiltonian $\hat{\mathcal{H}}_0 + \hat{V}_1$ and calculating the new energy. Already the leading minimisation correction produces an anisotropic energy gain

$$\Delta E^{(1)} = -\frac{1}{2}\,\frac{J^2\epsilon^2 n_{\rm imp}N}{2h}\Big[\cos^4\varphi\sin^2 2\theta + \sin^2 2\varphi\sin^2\theta + \sin^4\varphi\sin^2 2\theta + \sin^2 2\varphi\sin^2\theta + \sin^2 2\theta\Big].$$

Reparameterising this expression in terms of the order parameter, we obtain

$$\Delta E = \frac{J\epsilon^2 n_{\rm imp}N}{2}\big[m_x^4 + m_y^4 + m_z^4 + 1\big]. \tag{7.31}$$

The opposite states are favoured by this term with eight minima along the diagonals of the cube $\mathbf{S}_i = (\pm\sqrt{2}/2, \pm\sqrt{2}/2, \pm\sqrt{2}/2)$. Consideration of all possible stratified states, constructed from uniform configurations restores the discrete $\mathbb{S}_3$ permutation symmetry of the Hamiltonian. So much like in the previous 2D compass model, the configuration, stabilised by vacancies is not a long range order state.

7.4.2 Numerical results and reentrant phase transition

A combination of frustration with dimensional reduction, typical for the orbital models, makes them very difficult to study numerically. It is especially relevant for the 3D models, where the number of sites grows quickly with the characteristic length scale of the lattice $N = L^3$. Only recently the 3D 90° compass model was analysed numerically in an impressive Monte Carlo study by Gerlach and Janke [113]. They report the transition to the ordered phase at $T_c/J = 0.098$. The transition was found to be of the first order; however, due to very strong finite size effects, its discontinuous nature appears only at very large cluster sizes.

Here we investigate the 3D t_{2g} model with vacancies by the Monte Carlo method. Our principal aim is to study the competition of two anisotropies (7.30) and (7.31) at lowest T. Additionally, we describe the decrease of T_c with impurity concentration.

The ordered state of the pure model has all the spins aligned along one of the three cubic axes, parallel or antiparallel. It breaks the $\mathbb{S}_3$ symmetry of the Hamiltonian. Such state can be characterised by an order parameter q_2, constructed from the quadrupole tensors

$$q_2 = \frac{3}{2}\mathrm{tr}\Big[\big(Q^{\alpha\beta}\big)^2\Big]; \qquad Q^{\alpha\beta} = \frac{1}{N}\sum_i \big(S_i^\alpha S_i^\beta - \frac{1}{3}\delta^{\alpha\beta}\big). \tag{7.32}$$

q_2 is normed to unity in the perfect nematic state. In the opposite state, favoured by impurities all the spins are directed along the diagonals of the cube. Furthermore, every spin might take

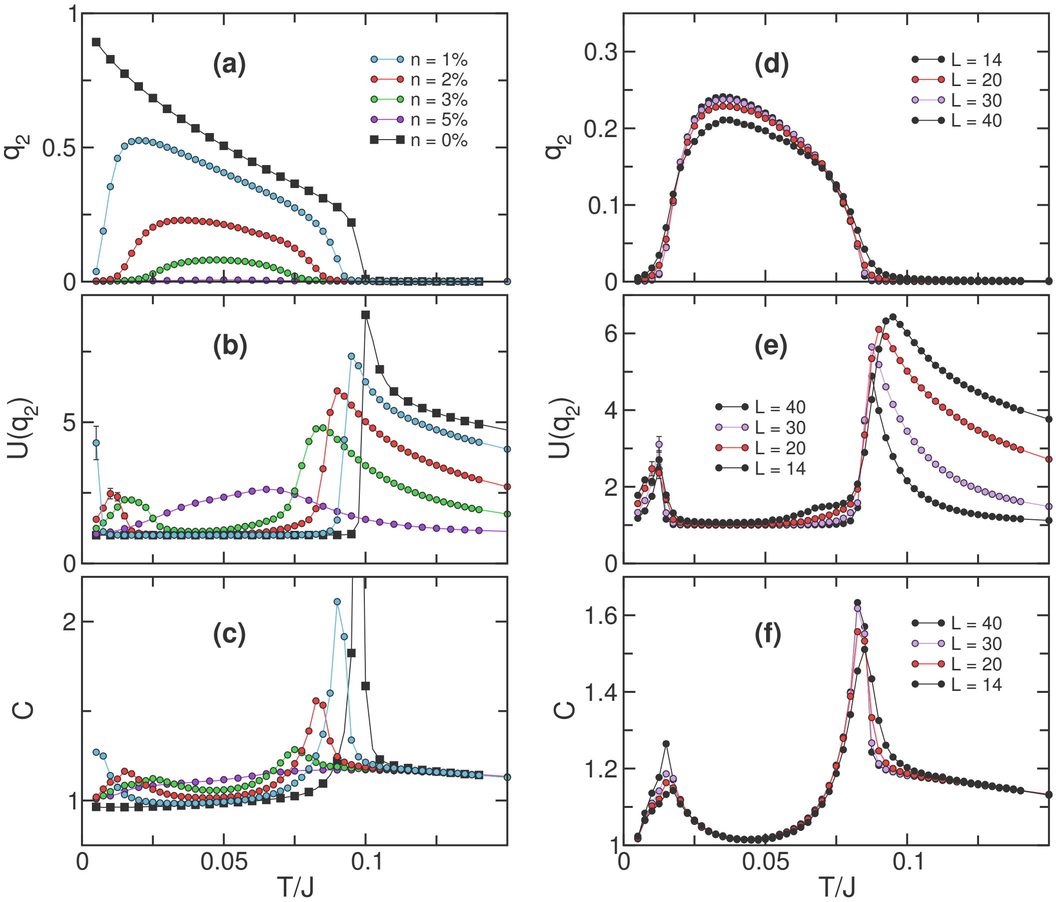

Figure 7.12: Monte Carlo simulations of the 3D 120° model with impurities on a L^3 cubic lattice with SBC. The nematic order parameter, its Binder cumulant and magnetic specific heat are plotted. (a) - (c) Suppression of the nematic phase by vacancies, for $L = 20$ clusters. Long range order disappears around $n_{\mathrm{imp}} = 3\%$, slightly earlier than in the 2D model. (d) - (f) Finite size analysis of the $n_{\mathrm{imp}} = 2\%$ case.

any of the eight orientations. This state has a nonzero octupole moment, but the diagonal of $Q^{\alpha\beta}$, hence q_2 is zero. We emphasise the fact that the octupole state does not constitute a true phase of the system because it does not break the symmetry of the Hamiltonian. So we do not calculate the octupole tensor in our calculations, as it is not an order parameter of the system.

Our numerical results are presented in figure 7.12. The behaviour of the order parameters resembles the one of the 2D model. Nematic order gets suppressed very quickly by impurities, it is already absent at $n_{\text{imp}} = 3\%$. At low T there is a reentrant transition to the paramagnetic phase, caused by vacancies.

Both observed transitions appear like the continuous ones, even though both are expected to be of the first order. However, our cluster sizes are not large enough to unambiguously say that it happens due to the effect of impurities alone.

The results of our numerical simulations confirm the analytic predictions that at low T structural disorder selection (7.31) takes over the thermal fluctuations (7.30). It results in a reentrant phase transition and restricts the nematic ordered phase from below.

7.5 Summary

In this chapter classical frustrated 120° and 90° compass models with emergent continuous ground state degeneracy were studied. In particular, we examined the order by structural disorder effect, which was found to always compete in continuous degeneracy lifting with the ordering by thermal fluctuations, similar to spin models, considered before.

At the same time, completely new effects were observed in orbital models. First, discrete emergent symmetries of the ground state of 120° model were found to be not affected by disorder. Therefore, the low-T phase is stabilised by essentially both fluctuations and defects. The former are necessary to preserve the $\mathbf{Q} = 0$ structure, and the latter select a particular state from a continuous manifold. The situation is different in both 2D and 3D 90° models, in these systems translational symmetry cannot be broken by fluctuation or disorder. Instead, a collinear nematic phase, which is stabilised by fluctuations, breaks the discrete reflection symmetry. But its anticollinear counterpart, selected by vacancies does not. So at low T both models undergo a reentrant transition to a PM state, which bounds the nematic phase from below in addition to a strong decrease of T_C by vacancies.

Our findings have direct relevance for the Mott insulators, which order through the cooperative Jahn-Teller effect. The observed first order transition between the ordered phases in the 120° model is manifested by the tetragonal to orthorhombic transition in these systems. In particular, we predict the appearance of a new orthorhombic phase at low T in diluted $\mathrm{KCu}_{1-x}\mathrm{T}_x\mathrm{F}_3$ when Cu is substituted by Zn [108] or Mg [117].

From the theoretical perspective, consideration of other types of randomness, bond disorder above all, as well as a study of diluted spin-orbital model may reveal further intriguing effects of quenched disorder. Moreover, it is likely to provide additional materials for the experimental observation of order by structural disorder effect. Finally, orbital models give a rare possibility to compare classical and quantum diluted frustrated systems. Study of the order by structural disorder effect by quantum Monte Carlo is an interesting and feasible challenge in these systems as, thanks to ferromagnetic interaction sign, the task is not plagued by the minus sign problem.

Chapter 8

Conclusion

In this work we have examined diverse frustrated systems, which have a continuously degenerate lowest energy state. And we have studied the interplay of various mechanisms of lifting this mean-field degeneracy: entropic ordering from internal thermal or quantum zero-point fluctuations, random modification of the structure by quenched disorder and tunable additional interaction, such as Zeeman interaction with an external magnetic field.

Each of these processes is capable of selecting certain states from the degenerate manifold and thus establishing long range order. Additional interactions break the degeneracy already on the mean-field level. Chapter 6, devoted to frustrated pyrochlore system in the external magnetic field provides an example of such process. The demonstrated phase diagrams for different directions of the magnetic field are of obvious importance as they can be directly applied to the description of $Er_2Ti_2O_7$ in the external field. However, we would like to emphasise another interesting and less apparent aspect of the study. The presented results are illustrations of the interplay between ordering due to fluctuations and energetic selection of states. The observed phase boundaries are completely missing in the mean-field description of the magnetic structure because the $\mathbb{Z}_6$ zero-field anisotropy, which is an essential element of the transitions, is produced by fluctuations. An interesting consequence of such transitions is that if observed, they would allow to directly quantify the strength of fluctuation effect.

Somewhat less obvious is the idea that random structural disorder can also participate in the establishment of long range order. When a small amount of impurities is added to the system, magnetic structure relaxes to a slightly distorted configuration, around one of the pure mean-field ground states. The *order by structural disorder* effect is realised by the fact that only this local distortion, but not an overall spin pattern, depends on the specific impurity replica.

States favoured by different mechanisms need not be the same, so the interplay usually results in a complex phase diagram with several phase transitions. The configurations stabilised via the order by disorder mechanism are usually well characterised and observed in real systems. Other states were reported in this work for the first time, so below we recapitulate some of our main results

In triangular antiferromagnets structural disorder favours the least collinear spin configurations from the continuously degenerate manifold of mean-field ground states. In the isotropic Heisenberg system it corresponds to the conical or umbrella state. When noncoplanar states are prohibited by anisotropy, the anti-Y or a fan configuration is established. In the XY anisotropic pyrochlore, on the contrary, impurities favour the most collinear $m_{x^2-y^2}$ (ψ_3) configuration. For all these models we derived corrections to energy from dilution in the form of effective anisotropies, acting on the degenerate manifold. The corresponding long range ordered phases were then observed in our numerical simulations in the low-T parameter region.

In contrast to the studied antiferromagnets in classical 120° and 90° compass models the states that are selected by impurities do not break any symmetry of the model. Therefore, structural disorder cannot set a long range ordered phase solely by itself. Still, the observed sequence of phase transitions in the 120° model shows both phases: the configuration, stabilised by fluctuations, and its antipode, favoured by defects. The latter, however, is only present at $T > 0$ when the breaking of the translational symmetry is assured by thermal order by disorder. On the other hand, 2D and 3D 90° compass models have only one phase with nematic order. Its low-T anticollinear counterpart is smoothly connected to the paramagnetic phase, and a corresponding transition is a reentrant phase transition.

All these findings of the work make up a rather wide variety of realisations of basically the same phenomenon. Structural defects, and in particular dilution, have an opposite effect on degenerate ground states, compared to thermal and quantum fluctuations. Structural and fluctuational ordering compete in selecting a particular state. And this competition results in appearance of a first order reconfigurational phase transition at low T, where structural disorder eventually overcomes the effect of fluctuations

The results that were presented in this work raise several natural questions. What is the fundamental reason of the similarity between quantum and thermal order by disorder? How universal is the scenario of competition of fluctuations and vacancies and can it be generalised for the other types of disorder? Finally, what is the impurity concentration when the effect breaks down and gives way to the (presumably) glassy phase?

One of the possible ways to tackle these problems is to investigate more complex frustrated systems, like the ones that appeared in orbital models. Another road is the numerical study of the same systems, but with the other types of structural disorder, such as bond disorder, mobile vacancies, etc. We showed that in most of the models real space perturbation theory predicts the same effect from the bond disorder as from dilution. However, numerical verification of this hypothesis was left out of the scope of this work. Description and understanding of the behaviour of the above models with bond disorder remains an interesting and important problem. It is additionally motivated by studies of the neighbouring frustrated systems with bond disorder that predicted the absence of the ordered state in the BCT antiferromagnets [21] or a spin-glass transition in the Heisenberg pyrochlore [118].

More challenging is the highly diluted limit of the considered (and other) frustrated systems. It requires the application of different methods, both analytical and numerical, including those used for studying spin glasses. As the absence of a small disorder parameter makes the perturbation inherently unreliable, while in the numerics large impurity concentration leads to extremely rough energy surface and smeared phase boundaries.

Also, prediction of phase boundaries for real systems is highly complicated by the necessity of calculation of spin-wave corrections around a structure, distorted by impurities. In this work we circumvented it by calculating quantum effects separately on pure system and neglecting all possible interplay of zero point fluctuations with dilution. The lack of a good quantitative description motivates the effort in this direction. A semiclassical method of calculating harmonic spin-wave corrections around classically unstable states was proposed in Ref. [119]. One may try to adapt this scheme to spin configurations, slightly distorted by weak impurities. Another possibility is to use the methods, employed for spin-wave calculations of the frustrated [120] or nonfrustrated [11, 14] antiferromagnets with a single impurity. Alternatively, the order by structural disorder effect can be studied numerically by the means of Quantum Monte Carlo simulations in orbital models, which are not affected by the minus sign problem owing to the ferromagnetic interaction of pseudospins.

Finally, experimental studies of diluted frustrated systems are highly demanded. In this work we have discussed various classes of compounds, where order by structural disorder effect can be observed experimentally. The most straightforward is the insulating pyrochlore $\mathrm{Er_2Ti_2O_7}$, especially considering the fact that studies of the diluted compound $\mathrm{Er}_{2-2x}\mathrm{Y}_{2x}\mathrm{Ti_2O_7}$ have already been reported [90].

The other class of systems, perspective for experimental observation are triangular antiferromagnets. Their main advantage is that a rather large variety of compounds that exhibit fingertips of ordering by fluctuations have been discovered. In spin systems structural disorder has to overcome the effect of quantum fluctuations, which scales as $1/S$. So among all candidates the high-spin magnets are the most perspective ones for detecting vacancy-induced ordered phases. These include a $S = 7/2$ triangular antiferromagnet $\mathrm{GdPd_2Al_3}$ [121] and a number of $S = 5/2$ magnets, such as $\mathrm{RbFe(MoO_4)_2}$ [3, 4], $\mathrm{Ba_3MnSb_2O_9}$ [66] etc.

Lastly, under a different disguise of tetragonal to orthorhombic structural transition the studied order by structural disorder effect may appear in the physics of doped Mott insulators. In $\mathrm{KCuF_3}$ and $\mathrm{LaMnO_3}$ orbital degrees of freedom order via the collective Jahn-Teller effect, and when diluted, we expect these materials to undergo an additional transition to an orthorhombic phase when the temperature is decreased. In comparison with quantum magnets, the orbital order in such systems is not enhanced by quantum zero-point fluctuations. Therefore, a substantially smaller dilution rate should be enough for the observation of the effect.

Bibliography

[1] J. Villain et al., *Order as an effect of disorder*, J. Phys. **41**, 1263–1272 (1980).

[2] E. F. Shender, *Antiferromagnetic garnets with fluctuationally interacting sublattices*, J. Exp. Theor. Phys. **56**, 178 (1982).

[3] T. Inami, Y. Ajiro, and T. Goto, *Magnetization Process of the Triangular Lattice Antiferromagnets* $RbFe(MoO_4)_2$ *and* $CsFe(SO_4)_2$, J. Phys. Soc. Jpn. **65**, 2374–2376 (1996).

[4] A. I. Smirnov et al., *Triangular lattice antiferromagnet* $RbFe(MoO_4)_2$ *in high magnetic fields*, Phys. Rev. B **75**, 134412 (2007).

[5] N. A. Fortune et al., *Cascade of Magnetic-Field-Induced Quantum Phase Transitions in a Spin-1/2 Triangular-Lattice Antiferromagnet*, Phys. Rev. Lett. **102**, 257201 (2009).

[6] M. E. Zhitomirsky et al., *Quantum Order by Disorder and Accidental Soft Mode in* $Er_2Ti_2O_7$, Phys. Rev. Lett. **109**, 077204 (2012).

[7] L. Savary et al., *Order by Quantum Disorder in* $Er_2Ti_2O_7$, Phys. Rev. Lett. **109**, 167201 (2012).

[8] S. Sachdev, C. Buragohain, and M. Vojta, *Quantum Impurity in a Nearly Critical Two-Dimensional Antiferromagnet*, Science **286**, 2479–2482 (1999), pmid: `10617456`.

[9] S. Sachdev and M. Vojta, *Quantum impurity in an antiferromagnet: Nonlinear sigma model theory*, Phys. Rev. B **68**, 064419 (2003).

[10] O. P. Sushkov, *Long-range dynamics related to magnetic impurities in the two-dimensional Heisenberg antiferromagnet*, Phys. Rev. B **68**, 094426 (2003).

[11] A. Lüscher and O. P. Sushkov, *Long-range dynamics of magnetic impurities coupled to a two-dimensional Heisenberg antiferromagnet*, Phys. Rev. B **71**, 064414 (2005).

[12] S. Eggert et al., *Universal Alternating Order around Impurities in Antiferromagnets*, Phys. Rev. Lett. **99**, 097204 (2007).

[13] J. Engel and S. Wessel, *From enhanced to reduced quantum antiferromagnetism by tuning a magnetic impurity*, Phys. Rev. B **80**, 094404 (2009).

[14] S. Shinkevich, O. F. Syljuåsen, and S. Eggert, *Spin-wave calculation of the field-dependent magnetization pattern around an impurity in Heisenberg antiferromagnets*, PHYS. REV. B **83**, 054423 (2011).

[15] C.-C. Chen et al., *Revealing the degree of magnetic frustration by non-magnetic impurities*, NEW J. PHYS. **13**, 043025 (2011).

[16] A. Wollny, L. Fritz, and M. Vojta, *Fractional Impurity Moments in Two-Dimensional Noncollinear Magnets*, PHYS. REV. LETT. **107**, 137204 (2011).

[17] A. Wollny, E. C. Andrade, and M. Vojta, *Singular Field Response and Singular Screening of Vacancies in Antiferromagnets*, PHYS. REV. LETT. **109**, 177203 (2012).

[18] A. Sen, K. Damle, and R. Moessner, *Fractional Spin Textures in the Frustrated Magnet* $SrCr_{9p}Ga_{12-9p}O_{19}$, PHYS. REV. LETT. **106**, 127203 (2011).

[19] C. L. Henley, *Ordering by disorder: Ground-state selection in fcc vector antiferromagnets*, J. APPL. PHYS. **61**, 3962–3964 (1987).

[20] T. M. Giebultowicz, *Monte Carlo simulations of dilute magnetic semiconductors for high concentrations of the magnetic component*, J. MAGN. MAGN. MATER. **54-57**, 1287–1288 (1986).

[21] Y. V. Fyodorov and E. F. Shender, *Random-field effects in antiferromagnets with classically degenerate ground states*, J. PHYS.: CONDENS. MATTER **3**, 9123 (1991).

[22] C. L. Henley, *Ordering due to disorder in a frustrated vector antiferromagnet*, PHYS. REV. LETT. **62**, 2056–2059 (1989).

[23] C. L. Henley and S. Prakash, *Ordering due to disorder in a frustrated* XY *antiferromagnet*, J. PHYS. COLLOQ. **49**, pages C8 (1988).

[24] C. Weber and F. Mila, *Anticollinear magnetic order induced by impurities in the frustrated Heisenberg model of pnictides*, PHYS. REV. B **86**, 184432 (2012).

[25] J. C. Slonczewski, *Fluctuation mechanism for biquadratic exchange coupling in magnetic multilayers*, PHYS. REV. LETT. **67**, 3172–3175 (1991).

[26] B. E. Larson and C. L. Henley, *Effective Hamiltonians for state selection in Heisenberg antiferromagnets* (2008), arXiv: `0811.0955`.

[27] A. V. Chubukov and D. I. Golosov, *Quantum theory of an antiferromagnet on a triangular lattice in a magnetic field*, J. PHYS.: CONDENS. MATTER **3**, 69 (1991).

[28] H. Kawamura and S. Miyashita, *Phase Transition of the Two-Dimensional Heisenberg Antiferromagnet on the Triangular Lattice*, J. PHYS. SOC. JPN. **53**, 4138–4154 (1984).

[29] P.-A. Lindgård, *Theory of Adiabatic Nuclear Magnetic Ordering in Cu*, PHYS. REV. LETT. **61**, 629–632 (1988).

[30] M. T. Heinilä and A. S. Oja, *Selection of the ground state in type-I fcc antiferromagnets in an external magnetic field*, PHYS. REV. B **48**, 7227–7237 (1993).

[31] B. Canals and M. E. Zhitomirsky, *An XY checkerboard antiferromagnet in an external field*, J. PHYS.: CONDENS. MATTER **16**, S759 (2004).

[32] A. Chernyshev and M. Zhitomirsky, *Quantum Selection of Order in an XXZ Antiferromagnet on a Kagome Lattice*, PHYS. REV. LETT. **113**, 237202 (2014).

[33] M. W. Long, *Effects that can stabilise multiple spin-density waves*, J. PHYS.: CONDENS. MATTER **1**, 2857 (1989).

[34] M. E. Zhitomirsky, *Real-space perturbation theory for frustrated magnets: application to magnetization plateaus*, J. PHYS.: CONF. SER. **592**, 012110 (2015).

[35] H. Kawamura and S. Miyashita, *Phase Transition of the Heisenberg Antiferromagnet on the Triangular Lattice in a Magnetic Field*, J. PHYS. SOC. JPN. **54**, 4530–4538 (1985).

[36] K. H. Höglund, A. W. Sandvik, and S. Sachdev, *Impurity Induced Spin Texture in Quantum Critical 2D Antiferromagnets*, PHYS. REV. LETT. **98**, 087203 (2007).

[37] D. P. Landau and K. Binder, *A Guide to Monte Carlo Simulations in Statistical Physics*, Cambridge University Press, (2000).

[38] M. E. J. Newman and G. T. Barkema, *Monte Carlo Methods in Statistical Physics*, Clarendon Press, (1999).

[39] N. Metropolis et al., *Equation of State Calculations by Fast Computing Machines*, J. CHEM. PHYS. **21**, 1087–1092 (1953).

[40] M. Creutz, *Overrelaxation and Monte Carlo simulation*, PHYS. REV. D **36**, 515–519 (1987).

[41] M. E. Fisher, *Theory of critical point singularities*, in: Critical phenomena, Proceedings of the 51st Enrico Fermi School, Academic Press, New York, (1971), 1–99.

[42] K. Binder, *Finite size effects at phase transitions*, in: Computational Methods in Field Theory, Springer Berlin Heidelberg, (1992), 59–125.

[43] K. Binder, *Critical Properties from Monte Carlo Coarse Graining and Renormalization*, PHYS. REV. LETT. **47**, 693–696 (1981).

[44] A. J. Liu and M. E. Fisher, *On the corrections to scaling in three-dimensional Ising models*, J STAT PHYS **58**, 431–442 (1990).

[45] A. M. Ferrenberg, D. P. Landau, and K. Binder, *Statistical and systematic errors in Monte Carlo sampling*, J STAT PHYS **63**, 867–882 (1991).

[46] W. Janke, *First-order phase transitions*, in: Computer Simulations of Surfaces and Interfaces, **114**, Dordrecht: Springer, (2003), 111–135.

[47] K. Binder, *Theory of first-order phase transitions*, REP. PROG. PHYS. **50**, 783 (1987).

[48] K. Binder and D. P. Landau, *Finite-size scaling at first-order phase transitions*, PHYS. REV. B **30**, 1477–1485 (1984).

[49] D. H. Lee et al., *Symmetry analysis and Monte Carlo study of a frustrated antiferromagnetic planar (XY) model in two dimensions*, PHYS. REV. B **33**, 450–475 (1986).

[50] P. Olsson and P. Minnhagen, *On the helicity modulus, the critical temperature and Monte Carlo simulations for the two-dimensional XY-model*, PHYS. SCR. **43**, 203 (1991).

[51] H. Kawamura, *Spin-Wave Analysis of the Antiferromagnetic Plane Rotator Model on the Triangular Lattice–Symmetry Breaking in a Magnetic Field*, J. Phys. Soc. Jpn. **53**, 2452–2455 (1984).

[52] D. H. Lee et al., *Discrete-Symmetry Breaking and Novel Critical Phenomena in an Antiferromagnetic Planar (XY) Model in Two Dimensions*, Phys. Rev. Lett. **52**, 433–436 (1984).

[53] T. Ono et al., *Magnetization plateaux of the* $S = 1/2$ *two-dimensional frustrated antiferromagnet* Cs_2CuBr_4, J. Phys.: Condens. Matter **16**, S773 (2004).

[54] H. D. Zhou et al., *Successive Phase Transitions and Extended Spin-Excitation Continuum in the S=1/2 Triangular-Lattice Antiferromagnet* $Ba_3CoSb_2O_9$, Phys. Rev. Lett. **109**, 267206 (2012).

[55] T. Susuki et al., *Magnetization Process and Collective Excitations in the* $S = 1/2$ *Triangular-Lattice Heisenberg Antiferromagnet* $Ba_3CoSb_2O_9$, Phys. Rev. Lett. **110**, 267201 (2013).

[56] N. D. Mermin and H. Wagner, *Absence of Ferromagnetism or Antiferromagnetism in One- or Two-Dimensional Isotropic Heisenberg Models*, Phys. Rev. Lett. **17**, 1133–1136 (1966).

[57] S. R. Hassan and R. Moessner, *Semiclassical degeneracies and ordering for highly frustrated magnets in a field*, Phys. Rev. B **73**, 094443 (2006).

[58] M. V. Gvozdikova, P.-E. Melchy, and M. E. Zhitomirsky, *Magnetic phase diagrams of classical triangular and kagome antiferromagnets*, J. Phys.: Condens. Matter **23**, 164209 (2011).

[59] L. Seabra et al., *Phase diagram of the classical Heisenberg antiferromagnet on a triangular lattice in an applied magnetic field*, Phys. Rev. B **84**, 214418 (2011).

[60] A. B. Harris, *Effect of random defects on the critical behaviour of Ising models*, J. Phys. C: Solid State Phys. **7**, 1671 (1974).

[61] B. Berche et al., *Influence of quenched dilution on the quasi-long-range ordered phase of the 2d XY model*, Eur. Phys. J. B **36**, 91–98 (2003).

[62] J.-K. Kim, *Weak universality in the two-dimensional randomly disordered three-state Potts ferromagnet*, Phys. Rev. B **53**, 3388–3391 (1996).

[63] M. Picco, *Numerical results for the two-dimensional random-bond three-state Potts model*, Phys. Rev. B **54**, 14930–14933 (1996).

[64] H. J. Lewtas et al., *Magnetic excitations in multiferroic* $LuMnO_3$ *studied by inelastic neutron scattering*, Phys. Rev. B **82**, 184420 (2010).

[65] M. Lee et al., *Magnetic phase diagram and multiferroicity of* $Ba_3MnNb_2O_9$*: A spin-5/2 triangular lattice antiferromagnet with weak easy-axis anisotropy*, Phys. Rev. B **90**, 224402 (2014).

[66] Y. C. Sun et al., *High-field magnetization and ESR in the triangular-lattice antiferromagnets* $Ba_3MnSb_2O_9$ *and* $Ba_3TNb_2O_9$ *(*$T = Ni, Co$*)*, Journal of Magnetism and Magnetic Materials **393**, 273–277 (2015).

[67] J. D. M. Champion et al., $Er_2Ti_2O_7$ *: Evidence of quantum order by disorder in a frustrated antiferromagnet*, Phys. Rev. B **68**, 020401 (2003).

[68] P. Dasgupta, Y. Jana, and D. Ghosh, *Crystal field effect and geometric frustration in* $Er_2Ti_2O_7$ *-an XY antiferromagnetic pyrochlore*, Solid State Communications **139**, 424–429 (2006).

[69] P. Dalmas de Réotier et al., *Magnetic order, magnetic correlations, and spin dynamics in the pyrochlore antiferromagnet* $Er_2Ti_2O_7$, Phys. Rev. B **86**, 104424 (2012).

[70] M. E. Zhitomirsky, P. C. W. Holdsworth, and R. Moessner, *Nature of finite-temperature transition in anisotropic pyrochlore* $Er_2Ti_2O_7$, Phys. Rev. B **89**, 140403 (2014).

[71] J. Oitmaa et al., *Phase transition and thermal order-by-disorder in the pyrochlore antiferromagnet* $Er_2Ti_2O_7$*: A high-temperature series expansion study*, Phys. Rev. B **88**, 220404 (2013).

[72] P. A. McClarty, P. Stasiak, and M. J. P. Gingras, *Order-by-disorder in the XY pyrochlore antiferromagnet*, Phys. Rev. B **89**, 024425 (2014).

[73] K. Ross et al., *Order by Disorder Spin Wave Gap in the XY Pyrochlore Magnet* $Er_2Ti_2O_7$, Phys. Rev. Lett. **112**, 057201 (2014).

[74] P. A. McClarty, S. H. Curnoe, and M. J. P. Gingras, *Energetic selection of ordered states in a model of the* $Er_2Ti_2O_7$ *frustrated pyrochlore XY antiferromagnet*, J. Phys.: Conf. Ser. **145**, 012032 (2009).

[75] S. Petit et al., *Order by disorder or energetic selection of the ground state in the XY pyrochlore antiferromagnet* $Er_2Ti_2O_7$*: An inelastic neutron scattering study*, Phys. Rev. B **90**, 060410 (2014).

[76] S. H. Curnoe, *Structural distortion and the spin liquid state in* $Tb_2Ti_2O_7$, Phys. Rev. B **78**, 094418 (2008).

[77] S. Onoda and Y. Tanaka, *Quantum Melting of Spin Ice: Emergent Cooperative Quadrupole and Chirality*, Phys. Rev. Lett. **105**, 047201 (2010).

[78] K. A. Ross et al., *Quantum Excitations in Quantum Spin Ice*, Phys. Rev. X **1**, 021002 (2011).

[79] J. P. C. Ruff et al., *Spin Waves and Quantum Criticality in the Frustrated XY Pyrochlore Antiferromagnet* $Er_2Ti_2O_7$, Phys. Rev. Lett. **101**, 147205 (2008).

[80] S. E. Palmer and J. T. Chalker, *Order induced by dipolar interactions in a geometrically frustrated antiferromagnet*, Phys. Rev. B **62**, 488–492 (2000).

[81] J. D. M. Champion and P. C. W. Holdsworth, *Soft modes in the easy plane pyrochlore antiferromagnet*, J. Phys.: Condens. Matter **16**, S665 (2004).

[82] A. W. C. Wong, Z. Hao, and M. J. P. Gingras, *Ground state phase diagram of generic XY pyrochlore magnets with quantum fluctuations*, Phys. Rev. B **88**, 144402 (2013).

[83] V. S. Maryasin and M. E. Zhitomirsky, *Order from structural disorder in the XY pyrochlore antiferromagnet $Er_2Ti_2O_7$*, PHYS. REV. B **90**, 094412 (2014).

[84] D. L. Bergman et al., *Effective Hamiltonians for some highly frustrated magnets*, J. PHYS.: CONDENS. MATTER **19**, 145204 (2007).

[85] A. Andreanov and P. A. McClarty, *Order induced by dilution in pyrochlore XY antiferromagnets*, PHYS. REV. B **91**, 064401 (2015).

[86] T. Lin et al., *Nonmonotonic residual entropy in diluted spin ice: A comparison between Monte Carlo simulations of diluted dipolar spin ice models and experimental results*, PHYS. REV. B **90**, 214433 (2014).

[87] X. Ke et al., *Nonmonotonic Zero-Point Entropy in Diluted Spin Ice*, PHYS. REV. LETT. **99**, 137203 (2007).

[88] K. A. Ross et al., *Lightly stuffed pyrochlore structure of single-crystalline $Yb_2Ti_2O_7$ grown by the optical floating zone technique*, PHYS. REV. B **86**, 174424 (2012).

[89] M. Campostrini et al., *Theoretical estimates of the critical exponents of the superfluid transition in ^4He by lattice methods*, PHYS. REV. B **74**, 144506 (2006).

[90] J. F. Niven et al., *Magnetic phase transitions and magnetic entropy in the XY antiferromagnetic pyrochlores $(Er_{1-x}Y_x)_2Ti_2O_7$*, PROC. R. SOC. LOND. MATH. PHYS. ENG. SCI. **470**, 20140387 (2014).

[91] S. S. Sosin et al., *Magnetic excitations in the XY-pyrochlore antiferromagnet $Er_2Ti_2O_7$*, PHYS. REV. B **82**, 094428 (2010).

[92] O. A. Petrenko, M. R. Lees, and G. Balakrishnan, *Low-temperature magnetisation process in the cubic pyrochlore quantum antiferromagnet $Er_2Ti_2O_7$*, EUR. PHYS. J. B **86**, 1–4 (2013).

[93] J. van den Brink et al., *Orbital dynamics in ferromagnetic transition-metal oxides*, PHYS. REV. B **59**, 6795–6805 (1999).

[94] Z. Nussinov et al., *Orbital order in classical models of transition-metal compounds*, EPL **67**, 990 (2004).

[95] A. Mishra et al., *Directional Ordering of Fluctuations in a Two-Dimensional Compass Model*, PHYS. REV. LETT. **93**, 207201 (2004).

[96] K. Kubo, *Quantum Fluctuation Induced Order in an Anisotropic Pseudospin Model*, J. PHYS. SOC. JPN. **71**, 1308–1312 (2002).

[97] T. Tanaka, M. Matsumoto, and S. Ishihara, *Randomly Diluted e_g Orbital-Ordered Systems*, PHYS. REV. LETT. **95**, 267204 (2005).

[98] T. Tanaka and S. Ishihara, *Dilution Effects in Two-Dimensional Quantum Orbital Systems*, PHYS. REV. LETT. **98**, 256402 (2007).

[99] T. Tanaka and S. Ishihara, *Dilution effect in correlated electron systems with orbital degeneracy*, PHYS. REV. B **79**, 035109 (2009).

[100] Z. Nussinov and J. van den Brink, *Compass models: Theory and physical motivations*, Rev. Mod. Phys. **87**, 1–59 (2015).

[101] G. Khaliullin, *Orbital Order and Fluctuations in Mott Insulators*, Prog. Theor. Phys. Supplement **160**, 155–202 (2005).

[102] K. I. Kugel' and D. I. Khomskii, *The Jahn-Teller effect and magnetism: transition metal compounds*, Sov. Phys. Usp. **25**, 231 (1982).

[103] J. v. d. Brink, *Orbital-only models: ordering and excitations*, New J. Phys. **6**, 201 (2004).

[104] L. Paolasini et al., *Coupling between Spin and Orbital Degrees of Freedom in $KCuF_3$*, Phys. Rev. Lett. **88**, 106403 (2002).

[105] Z. Nussinov and E. Fradkin, *Discrete sliding symmetries, dualities, and self-dualities of quantum orbital compass models and $p + ip$ superconducting arrays*, Phys. Rev. B **71**, 195120 (2005).

[106] L.-M. Duan, E. Demler, and M. D. Lukin, *Controlling Spin Exchange Interactions of Ultracold Atoms in Optical Lattices*, Phys. Rev. Lett. **91**, 090402 (2003).

[107] M. Ferrero, F. Becca, and F. Mila, *Freezing and large time scales induced by geometrical frustration*, Phys. Rev. B **68**, 214431 (2003).

[108] N. Tatami et al., *Orbital ordering and the dilute effect in copper fluoride*, Journal of Magnetism and Magnetic Materials, Proceedings of the 17th International Conference on Magnetism, The International Conference on Magnetism **310**, 787–789 (2007).

[109] S. Ohtani et al., *Orbital dilution effect in ferrimagnetic $Fe_{1-x}Mn_xCr_2O_4$: competition between anharmonic lattice potential and spin-orbit coupling*, J. Phys.: Condens. Matter **22**, 176003 (2010).

[110] S. Wenzel and A. M. Läuchli, *Unveiling the Nature of Three-Dimensional Orbital Ordering Transitions: The Case of e_g and t_{2g} Models on the Cubic Lattice*, Phys. Rev. Lett. **106**, 197201 (2011).

[111] S. Wenzel and A. M. Läuchli, *Monte Carlo study of the critical properties of the three-dimensional* 120° *model*, J. Stat. Mech. **2011**, P09010 (2011).

[112] S. Wenzel, W. Janke, and A. M. Läuchli, *Re-examining the directional-ordering transition in the compass model with screw-periodic boundary conditions*, Phys. Rev. E **81**, 066702 (2010).

[113] M. H. Gerlach and W. Janke, *First-order directional ordering transition in the three-dimensional compass model*, Phys. Rev. B **91**, 045119 (2015).

[114] C. D. Batista and Z. Nussinov, *Generalized Elitzur's theorem and dimensional reductions*, Phys. Rev. B **72**, 045137 (2005).

[115] S. Elitzur, *Impossibility of spontaneously breaking local symmetries*, Phys. Rev. D **12**, 3978–3982 (1975).

[116] S. Wenzel and W. Janke, *Monte Carlo simulations of the directional-ordering transition in the two-dimensional classical and quantum compass model*, Phys. Rev. B **78**, 064402 (2008).

[117] P. Ghigna et al., *Experimental disentangling of orbital and lattice energy scales by inducing cooperative Jahn-Teller melting in $KCu_{1-x}Mg_xF_3$ solid solutions*, Phys. Rev. B **81**, 073107 (2010).

[118] A. Andreanov et al., *Spin-glass transition in geometrically frustrated antiferromagnets with weak disorder*, Phys. Rev. B **81**, 014406 (2010).

[119] T. Coletta, M. E. Zhitomirsky, and F. Mila, *Quantum stabilization of classically unstable plateau structures*, Phys. Rev. B **87**, 060407 (2013).

[120] B. Xu et al., *Collinear to Anti-collinear Quantum Phase Transition by Vacancies* (2011), arXiv: `1104.1848`.

[121] H. Kitazawa et al., *High-field magnetization of triangular lattice antiferromagnet: $GdPd_2Al_3$*, Physica B: Condensed Matter **259–261**, 890–891 (1999).

List of publications

- V. S. Maryasin and M. E. Zhitomirsky, *Triangular Antiferromagnet with Nonmagnetic Impurities*, Phys. Rev. Lett. **111**, 247201 (2013).
- V. S. Maryasin and M. E. Zhitomirsky, *Order from structural disorder in the XY pyrochlore antiferromagnet* $Er_2Ti_2O_7$*.*, Phys. Rev. B **90**, 094412 (2014).
- V. S. Maryasin and M. E. Zhitomirsky, *Collective impurity effects in the Heisenberg triangular antiferromagnet*, J. Phys.: Conf. Ser. **592**, 012112 (2015).
- V. S. Maryasin, M. E. Zhitomirsky, and R. Moessner, *Low-field behavior of an XY pyrochlore antiferromagnet: emergent clock anisotropies.* In preparation.